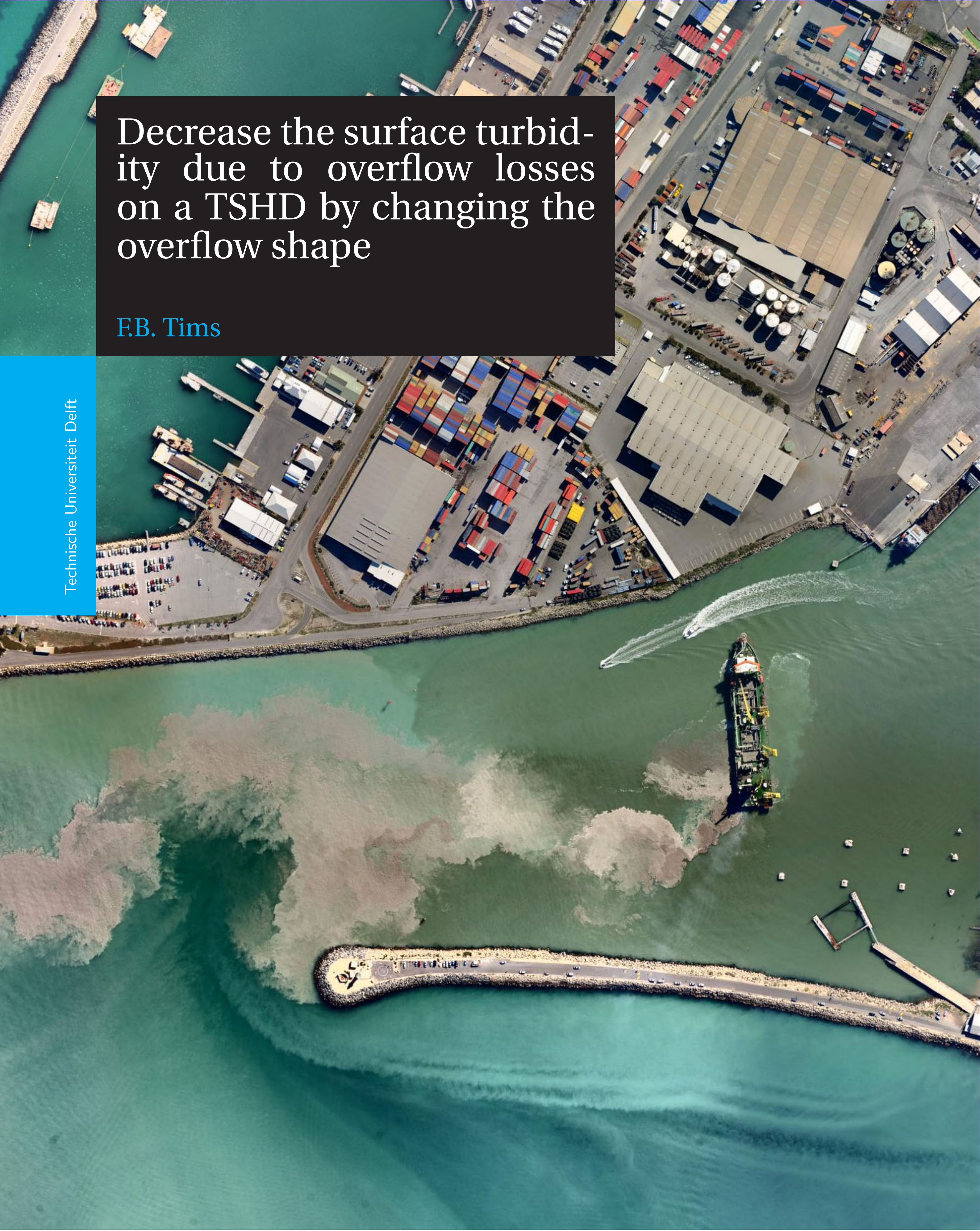

# Decrease the surface turbidity due to overflow losses on a TSHD by changing the overflow shape

F.B. Tims

Technische Universiteit Delft

TU Delft Delft University of Technology

Challenge the future

# Decrease the surface turbidity due to overflow losses on a TSHD by changing the overflow shape

by

**F.B. Tims**

in partial fulfillment of the requirements for the degree of

**Master of Science**
in Offshore & Dredging Engineering

at the Delft University of Technology,
to be defended publicly on Tuesday May 28, 2019 at 10:00 AM.

| | | |
|---|---|---|
| Student number: | 4418808 | |
| Project duration: | February 19, 2018 – May 22, 2019 | |
| Chairman: | Dr. Ir. G.H. Keetels | TU Delft |
| Thesis committee: | Ir. G. Teheux | APT Offshore BV |
| | Dr. Ir. R.L.J. Helmons | TU Delft |
| | Dr. F. Schulte | TU Delft |

*This thesis is confidential and cannot be made public until May 28, 2020*

# Preface

My final step finishing the master Offshore & Dredging Engineering at the Technical University of Delft, this master thesis. Thanks to APT Offshore which gave me the opportunity to investigate deeply into turbidity problems regarding Trailing Hopper Suction Dredgers and finding an improvement to reduce this problem. During this year, I have worked closely together with a great number of people which helped and supported me throughout this period.

First of all I want to thank my daily supervisors Dr. Ir. G.H. Keetels and Ir. G. Teheux which both showed great interest and helped me with the problems I faced. They provided me with lots of information and new insights and offered me great feedback during the research. During the experiments I had a great time with my fellow student W. Pont where we both helped each other out with small practical things. Next to that, all experiments could not be done without the help of Ir. F. van Grunsven and the lab supervisors F. Brakel and E. Stok.

Finally, I want to thank my family for all support they gave me during this thesis, but also all years before that. I really feel the love they give me and want to thank them deeply from my heart, a place where since a few months my girlfriend is added who pushed in in the right direction in the last few months of this thesis. The writing of this thesis also marks the end of my academic career and I look forward to the next chapter in my life. I wish the reader much enjoyment reading this paper.

*F.B. Tims*
*Delft, May 22, 2019*

# Summary


Already since the start of civilisation dredging is carried out to create and maintain waterways and ports or to create new land. In recent times the scale of dredging and awareness of potential environmental impact of dredging have increased drastically. An often used dredging vessel is the trailing suction hopper dredger (TSHD). A TSHD pumps up a water-sediment mixture from the bed into a hopper. In this hopper the sediment is given time to settle and the process water is spilled overboard, often through a vertical shaft called the overflow. The spilled process water will contain some suspended sediment which has not deposited yet and this forms a turbid plume. Increased turbidity and deposition at the bed of the suspended sediment from the overflow dredging plume can have negative environmental impact. Identify the factors which create the surface plume and testing a solution to improve this is done in this thesis.

Initial mixing of the overflow dredging plume under/near the TSHD is not well understood. Although the plume starts under the keel of a TSHD, it has initial downward velocity and it is denser than the ambient water, sometimes a part of the plume flows upward and reaches the free surface right behind the TSHD. This so called surface plume can stay suspended for long periods and is therefore important for the potential environmental impact. This thesis reports on laboratory experiments in still ambient water and numerical modelling with a crossflow.

Firstly, all influence factors which create a surface plume are investigated to see which factors have the highest influence. Based on the wish of a passive solution and the ability to do laboratory experiments, specific attention is given to the change of overflow shape, from round to rectangular. The analytical background of plume dispersion with different shapes is investigated to find the differences between them.

The laboratory experiments where conducted at the dredging lab at the Technical University of Delft. In this lab, a $25m^3$ tank filled with water where at the top a frame is positioned which holds the overflow pipe. By adding two type of nozzles (different rectangular aspect ratio) onto the pipe, the outflow shape is changed to see if a rectangular outflow shape improves the plume path in still ambient water. This is done by measuring the concentrations at the bottom and measuring the angle of the plume. Results of the experiments show less entrainment by finding smaller plume angles and higher concentrations in the middle of the plume when having a rectangular outflow shape.

To say something about the improvement of the plume path in real live, the plume is modelled by adding a crossflow. The information from the experiments is used to create a plume trajectory of the round outflow shape and rectangular outflow shape which are then compared with each other. Practical values are then scaled and used in the model. Results of the model show similarity from the experiments, with a deeper plume trajectory when having a rectangular outflow shape.

# Samenvatting

Vanaf het begin van de beschaving wordt er gebaggerd voor aanleg of onderhoud van waterwegen en havens of om nieuw land te creëren. Recentelijk is de schaal van baggeren en het besef van potentiële milieu effecten enorm toegenomen. Een vaak gebruikt baggerwerktuig is de trailing suction hopper dredger (TSHD). Een TSHD zuigt een water-sediment mengsel vanaf de bodem in een beun. Hier krijgt het sediment de tijd om te bezinken en het proceswater wordt overboord gemorst, vaak via een verticale buis die een overvloei genoemd wordt. Dit proceswater bevat vaak gesuspendeerd sediment wat nog niet bezonken is in het beun en dit vormt een troebele pluim. Toename in troebelheid en bezinking van gesuspendeerd sediment op de bodem kan een negatieve milieu impact hebben. Daarom is het modelleren van deze invloeden van baggeren vaak een essentieel onderdeel van een milieu-effect-rapportage van baggerwerken. Het identificeren van the factoren die deze suspensie veroorzaken en het testen van een oplossing om dit te verbeteren wordt behandeld in dit rapport.

Er is nog veel onduidelijk over de initiële menging van een overvloei baggerpluim onder/nabij het baggerschip. Hoewel de pluim onder de kiel van het baggerschip begint, de initiële snelheid neerwaarts gericht is en de pluim zwaarder is dan de omgeving, komt toch soms een deel van de pluim direct achter het baggerschip omhoog naar het wateroppervlak. Deze oppervlaktepluim kan zeer lang in suspensie blijven en is daarom belangrijk voor de potentiële milieu impact. Dit verslag rapporteerd lab experimenten in stabiel stilstaand water en nummerieke modellering met een achtergrondstroming.

Als eerst worden alle factoren die de suspensie van sediment veroorzaken onderzocht. Gebasseerd op de wens van een passieve oplossing en de mogelijkheid om experimenten uit te voeren in een testopstelling, is specifieke aandacht gegeven aan de verandering van uitstroomvorm, wat is veranderd van rond naar rechthoekig. De analytische achtergrond van pluim verspreiding met verschillende uitstroomvormen is onderzocht om een verschil te vinden tussen deze.

De lab experimenten zijn gedaan in het baggerlab van de Technische Universiteit Delft. In dit lab is gebruik gemaakt van een $25m^3$ reservoir die gevuld is met water. Aan de bovenkant van het reservoir is een frame gepositioneerd die die overvloei buis vasthoudt. Door aan de overvloei buis twee type mondstukken (die een verschillende aspect ratio hebben) te bevestigen wordt de uitstroomvorm veranderd van rond naar rechthoekig om te zien of een rechthoekige uitstroomvorm positief effect heeft op het traject van de pluim in stilstaand water. Dit is gedaan door de concentratie op de bodem van het reservoir te meten en door de hoeken te meten van de pluim. De resultaten van de experimenten laten minder loslating zien tussen de pluim en het stilstaande water, en dus een smallere pluim hoek, en hogere concentratie in het midden van de pluim wanneer de rechthoekige uitstroomvorm gebruikt wordt.

Om iets te kunnen zeggen over de verbeteringen ten opzichte van het traject van de pluim in de praktijk is de pluim gemodelleerd met daarbij een toevoeging van achtergrond stroming. De informatie van de experimenten is gebruikt om zowel het traject van de pluim te modelleren voor een ronde uitstroomvorm en een reckhoekige uitstroomvorm waarbij deze daarnaast vergeleken zijn met elkaar. Praktische waardes zijn geschaald en gebruikt in het model. Resultaten van het model laten overeenkomsten zien met resulaten van de experimenten met een dieper traject van de pluim wanneer er gebruikt wordt gemaakt van een rechhoekige uitstroomvorm.

# Contents

# List of Figures

# List of Tables

# Nomenclature

**Roman Symbols**

| | | |
|---|---|---|
| $A_0$ | Initial overflow area | $[m^2]$ |
| $A_c$ | Plume element area due to plume curvature | $[m^2]$ |
| $A_p$ | Projected area plume element | $[m^2]$ |
| $A_w$ | Plume element area due to plume growth | $[m^2]$ |
| $B_0$ | Initial overflow buoyancy flux | $[m^4/s^3]$ |
| $b_k$ | Plume element radius | $[m]$ |
| $B_o$ | Lateral distance from overflow to ships centerline | $[m]$ |
| $D$ | Plume source pipe diameter (Overflow outflow diameter) | $[m]$ |
| $d_0$ | Plane/slot width | $[m]$ |
| $E_p$ | Entrainment correction term due to the plume curvature | $[-]$ |
| $E_p$ | Entrainment due to the projected plume area normal to the crossflow | $[-]$ |
| $E_w$ | Entrainment correction term due to the increase in plume width | $[-]$ |
| $f$ | Oscillating frequency | $[1/s]$ |
| $F_\Delta$ | Densimetric Froude number | [-] |
| $g$ | Gravity acceleration | $[m/s^2]$ |
| $H_k$ | Depth below the keel | [-] |
| $h_k$ | Plume element thickness | $[m]$ |
| $l_m$ | Jet-to-plume length scale | $[m]$ |
| $L_o$ | Distance from overflow to stern | $[m]$ |
| $M_0$ | Initial overflow momentum flux | $[m^4/s^2]$ |
| $Q_0$ | Initial outflow volume | $[m^3/s]$ |
| $S$ | Centerline dilution ratio | [-] |
| $U_{cf}$ | Ambient crossflow velocity | $[m/s]$ |
| $v_e$ | Entrainment velocity | $[m/s]$ |
| $V_k$ | Jet velocity | $[m/s]$ |
| $W_0$ | Overflow exit velocity | $[m/s]$ |
| $z_b$ | Buoyancy length scale | $[m]$ |
| $z_c$ | Deep water momentum length scale | $[m]$ |
| $z_m$ | Momentum length scale | $[m]$ |

**Greek Symbols**

| | | |
|---|---|---|
| $\alpha_G$ | Entrainment coefficient based on Gaussian velocity profile | [-] |
| $\alpha_y$ | Yaw angle | [°] |
| $\beta_G$ | Spreading rate based on Gaussian profile | [-] |
| $\Delta\rho$ | Excess mass density of sediment in ambient fluid | $[kg/m^3]$ |
| $\Delta M$ | Total increase of mass at each time-step | $[kg]$ |
| $\Delta M_f$ | Increase of mass at each time-step due to vortex entrainment | $[kg]$ |
| $\Delta M_s$ | Increase of mass at each time-step due to shear entrainment | $[kg]$ |
| $\Delta U$ | Relative jet velocity in direction of jet axis per time step | $[m/s]$ |
| $\lambda$ | Jet-to-crossflow velocity ratio | [-] |
| $\lambda_r$ | Ratio of concentration-to-velocity width | [-] |
| $\phi_a$ | Volume fraction of air | [-] |
| $\phi_k$ | Angle of jet axis with horizontal plane | [°] |
| $\phi_s$ | Volume fraction of sediment | [-] |
| $\psi$ | Angle between the ship centerline and its speed through water | [°] |
| $\rho_a$ | Mass density of ambient fluid | $[kg/m^3]$ |
| $\rho_m$ | Mass density of mixture | $[kg/m^3]$ |
| $\rho_s$ | Mass density of solids | $[kg/m^3]$ |
| $\rho_w$ | Mass density of water | $[kg/m^3]$ |
| $\rho_{air}$ | Mass density of air | $[kg/m^3]$ |
| $\theta_k$ | Angle between the x-axis and the projection of the jet axis on the horizontal plane | [°] |

**Abbreviations**

| | |
|---|---|
| 1D | One Dimensional |
| 2D | Two Dimensional |
| 3D | Three dimensional |
| CFD | Computational Fluid Dynamics |
| JETLAG | Lagrangian jet |
| JICF | Jet In Cross Flow |
| LES | Large Eddy Simulation |
| NTU | Nephelometric Turbidity Unit |
| PAE | Projected Area Entrainment |
| TSHD | Trailing Suction Hopper Dredger |
| ZEF | Zone Established Flow |
| ZFE | Zone of Flow Establishment |

# 1

# Introduction

*The introduction gives information about the topic of this master thesis. Furthermore the research aim, research methodology and the outline of this master thesis is presented.*

## 1.1. OVERVIEW TSHD

The Trailing suction hopper dredger (TSHD) is a ship that is equipped with one or two suction pipes, which are lowered to the seabed during dredging operations. A water-sediment mixture is sucked up to the ship which will be discharged in the cargo hold, also called the hopper of the ship. The hopper is filled, where the sand particles settle and excess water flows overboard. The loading process of a TSHD is shown in figure 1.1[van Rhee, 2017].

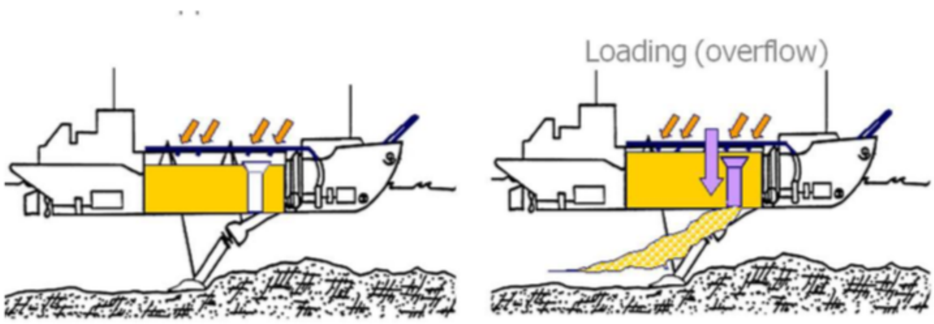


Figure 1.1: Loading process of a TSHD

After the loading process, the TSHD sails to the designated location where the hopper is discharged by opening the doors in the bottom of the ship, pumping the sediment ashore or by rain bowing, which is shown in figure 1.2 [Institute, 2018]

Figure 1.2: Discharge of TSHD by rainbowing

The hopper inlet system varies between ships, but the general aim is to divide the water-sediment mixture over the width of the hopper. During the loading process, the hopper is filled with water to obtain a water level inside the hopper equal to outside. The inlet loading pipes discharge the sucked up water-sediment mixture inside the hopper. The sand particles settle and will form a bed, which grows during the loading process.

## 1.2. DESCRIPTION OF OVERFLOW

The excess water flows overboard through the overflow. The commonly used overflows these days are adjustable in the vertical to regulate the overflow in the hopper. An overview of an overflow is shown in figure 1.3.

The overflow will transport the excess water underneath the hull into the surrounding water. However, not every sand particle will settle inside the hopper due to the current from the inlets to the overflow inside the hopper. With the dividing of the water-sediment mixture over the hopper dimension the process is more or less controlled to load as fast as possible, and so, to lose as less sand particles through the overflow. Despite this, the control of the process is very hard and so sediment particles are lost through the overflow.

Figure 1.3: Overview of hopper with overflow [IHC, 2018]

## 1.3. ECOLOGICAL EFFECTS OF SEDIMENT TURBIDITY

Overflow losses on a TSHD may lead to increased turbidity, higher suspended concentrations in the upper water column and enhanced sediment deposition. This mainly affects performance of visual predators and growth and survival of bottom vegetation as is shown in figure 1.4. However it is not understood yet, how large this impact is and whether it results in real problems. The circumstances in the sea and the bed may change, but it is not clear if and how it will affect the flora and fauna in this region. The tolerance levels of different species of plant and animals differ from each other. Therefore some species may profit from increased sedimentation or suspended matter concentrations, whilst others do not survive a slight change in living environment. An important aspect is the kind of material that is released into the water. Clay particles together with organic material can form large coagulates that absorb a lot of light, while the organic material is also a source of food. In contrast a same weight of sand particles absorbs almost no light. [Dankers, 2002]

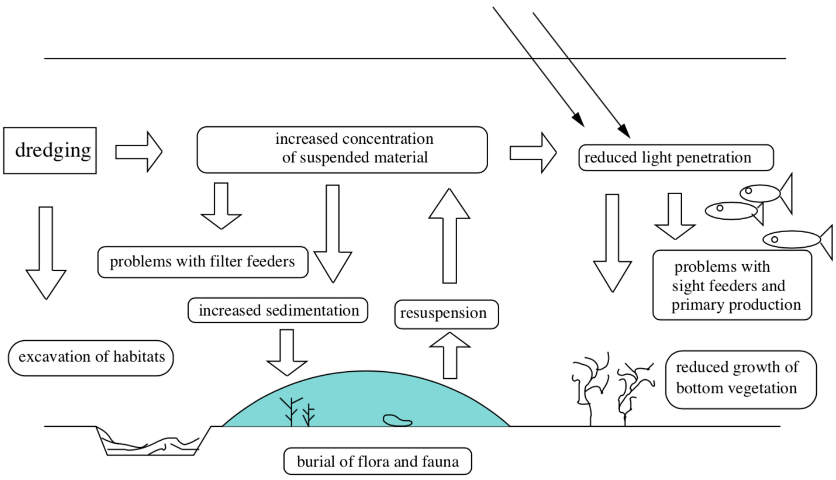


Figure 1.4: Ecological effect dredging

## 1.4. RESEARCH AIM

The aim of this master thesis is to provide insight in which factors influence the amount of surface turbidity and investigate a solution to decrease the surface turbidity. The turbidity has ecological and visual impact and should be decreased in ecological point of view. Based on the research and the preference of a passive solution, the change in overflow shape is chosen to investigate further, by doing experimental tests in stable water and give an indication of the plume trajectory in combination with a crossflow with the Lagrangian jet (JETLAG) model.

## 1.5. RESEARCH METHODOLOGY

The research methodology is characterized by the following steps:

- Description dredging processes in the near field
- Find out which factors influence the creation of a surface plume
- Further investigation of overflow shapes
- Practical experiments in stable ambient water
- Using the JETLAG model to give an indication of the plume trajectory with crossflow

## 1.6. OUTLINE

In Chapter 2, the different processes which occur during dredging on a TSHD are explained. The processes contain the sedimentation in the hopper which will induce overflow losses at a certain moment. A turbulent buoyant jet exits the overflow in ambient water, which can feel an ambient crossflow. The mixing of the dredging plume and the crossflow causes near field dredging processes which are elaborated further. The influence factors that create turbidity or a surface plume are deeper investigated. By the use of literature and models, each influence factor is investigated to see the effect of each influence factor independently to the creation of a surface plume.
Chapter 3 describes the analytical literature regarding plane- and round outflow shapes. Also the difference between a jet and plume is explained, with the regrading equations to see that the momentum and mass equations are conserved, with the turbulent diffusion accounted for. Chapter 4 describes the experimental setup and parameters used for the experimental tests.
Chapter 5 describes the results of the experimental tests, divided into two parts: concentration measurements and angle measurements. The angle measurements are used to derive an entrainment coefficient, which is related to the spreading rate of the plume. Based on the derived entrainment coefficient, the JETLAG model from Lee & Chu [2003] is used to give an indication of the plume path when it has an interaction with a crossflow. This information is found in Chapter 6. In addition, Chapter 7 sums up this thesis with conclusions and recommendations.

# 2

# Description Dredging Processes

*To give a first inside about overflow losses, the dredging process of a TSHD is presented in this chapter. This process consists of the sedimentation in the hopper and with that the loss of sediment into the overflow (section 2.1). Several models of Camp, Miedema & Vlasblom and van Rhee come back in this section. Furthermore, the plumes that come out of the overflow are described (section 2.2). Here we can find different descriptions like, a dynamic plume of a passive plume and the meaning of them. Next to that, the interaction with ambient cross-flow is investigated and the near field processes of a dredging plume are described (section 2.3). Mixing with ambient water is strong dependent on two numbers and with empirical length scales something can be said about the mixing length.*
*The nearfield processes of the dredging plume are described in section 2.4. The factors which influence the amount of surface plume or overall turbidity in the water column are further described in section 2.5. In total, twelve influence factors are elaborated where one is chosen to investigate further. A research question is formulated at the end of this section.*

## 2.1. SEDIMENTATION IN HOPPER & OVERFLOW LOSSES

Research on the sedimentation process is carried out by multiple professors like [Miedema & Vlasblom, 1996], [Ooijens, 1999] and [van Rhee, 2002]. All their models are based on the [Camp, 1946] model, a settling basin theory model which was developed for waste water treatment. The Camp model is a strongly simplified flow field where no vertical flow and constant flow depth are assumed. Miedema & Vlasblom [1996] used the Camp model as the basis for their model, but added sorting, erosion, the hindered settling effect and the influence of a rising sand bed. In addition, Ooijens [1999] added dynamics for example the time effect, which was added by regarding the hopper as an ideal mixing tank. Miedema & Vlasblom [1996] assumed an equal inflow concentration and concentration in the hopper and a instantaneous reaction of the outflow concentration on the determined settling efficiency. Ooijens [1999] used the calculated concentration in the hopper for the settling efficiency. In general, the overflow losses increase exponentially at the later stage of filling the hopper. This theory is however outdated by the research of van Rhee [2002] where several experiments are carried out in a rectangular laboratory flume with a glass side wall, where flow patterns could be monitored. van Rhee [2002] concluded that the hopper area can be divided into five different sections (figure 2.1), where A is the inflow and B is the density current.

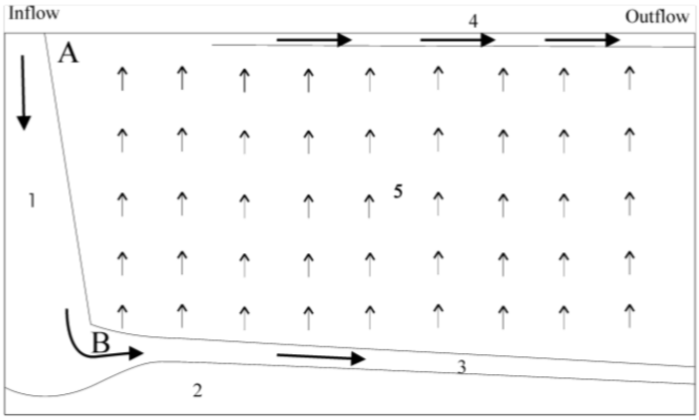


Figure 2.1: Schematic overview of flow field in hopper.

The five different sections are divided in:

1. Inflow section
2. Settled sand / stationary bed
3. Density flow over settled bed
4. Horizontal flow at the surface towards overflow
5. Suspension in remaining area

The incoming mixture (A) flows towards the bottom and forms an erosion crater and density current (B). From this current, sedimentation will take place where coarser particles will settle first which results in a rising bed level. A part of the incoming sediment which does not settle (fine particles) will go up in suspension. When the overflow level is reached, the surface water creates a horizontal current to the overflow. This process is continued until the hopper is completely filled with sediment.

van Rhee [2002] measured the the particle size distribution at the inflow and outflow where the overflow samples showed a large variation of particle size distribution, becoming coarser in time. The increasing grain diameter in the overflow is related to the increasing concentration in the overflow. Due to hindered settling, the settling velocity decreases with concentration and therefore larger particles remain in suspension and are removed with the overflow. Also, erosion of the bed at the surface when the hopper is almost totally filled, adds coarser materials to the overflow.

van Rhee [2002] used the observed flow field and grain size distributions to develop a numerical 1DV model to determine the overflow losses. Instead of the Camp model, which uses a horizontal one-dimensional approach with a horizontal supply on one side and overflow on the other. The 1DV model of van Rhee [2002] is

a vertical model, where sediment is supplied from the bottom and the overflow is located at the top. In addition, the influence of the hopper load parameter and the mutual interaction of the different grain sizes of the particle size distribution is implemented. The numerical 1DV model was compared with hopper sedimentation tests where a good correlation was shown between the model and the experiments. However, horizontal transport and erosion are not accounted for in the 1DV model and probably scale effects are present. Therefore the model can not be guaranteed to be in agreement with reality.
In order to include horizontal transport, van Rhee [2002] extended the 1DV model to a 2DV model. A boundary condition at the interface between the settled sediment and the mixture above had to be formulated for the numerical model. In order to do this, sedimentation tests where done in the laboratory and an empirical relation between the bed shear stress and the reduction of the sedimentation flux was found. This empirical relation was built in the 2DV model, after which the model was validated and found to agree well with laboratory- and prototype measurements.

## 2.2. DESCRIPTION OF OVERFLOW PLUMES

The water-sediment mixture that leaves the overflow may have large ecological impact. This depends on, among other things, how the sediment is distributed when leaving the overflow. Upon release from the bottom of the ship, the water-sediment mixture forms a negative-buoyant plume, which is either mixed directly with the ambient water or behaves as a density current [Winterwerp, 2002]. Plumes that are mixed directly are called passive plumes and plumes that behave as a density current are called dynamic plumes.

**Dynamic Plumes**

Dynamic plumes, shown in figure 2.2 [Dankers, 2002], descend rapidly as a current to the seabed and spread radially across the seabed as a dense plume, slowing down in time and distance as the kinetic energy is lost due to friction. The bulk behaviour of the water-sediment mixture rather than the individual settling velocity is important [Winterwerp, 2002]. Because of the rather high (bulk) settling velocity of a dynamic plume, the zone of impact is small.

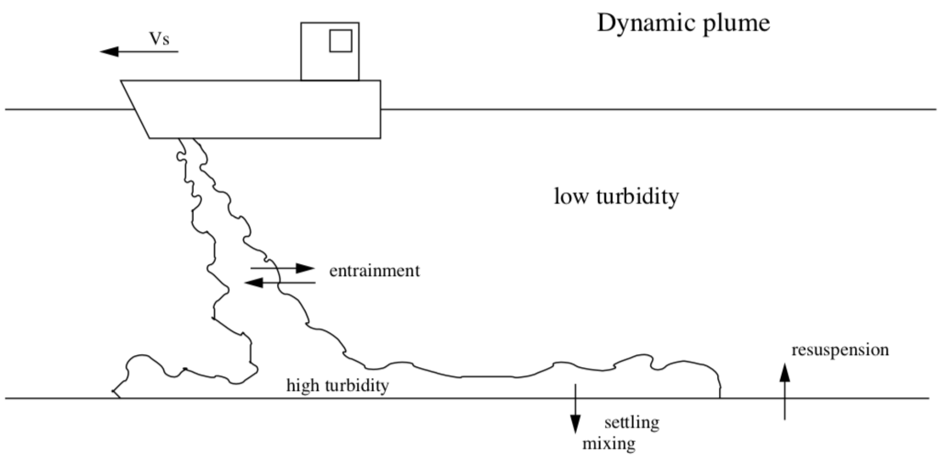


Figure 2.2: Dynamic plume phase

**Cloud formation**

A particular case of a dynamic plume develops when the outflow of the overflow is discontinuous. Clouds of sediment, water and air bubbles that entered the overflow due to the discontinuous outflow of the overflow are formed which do not behave as a dynamic plume shown in figure 2.2. This phenomena is called cluster settling, convective settling or cloud formation. Clouds can also form from density currents by stretching and eventually 'breaking' in different parts. The cloud formation is presented in figure 2.3 [Dankers, 2002].

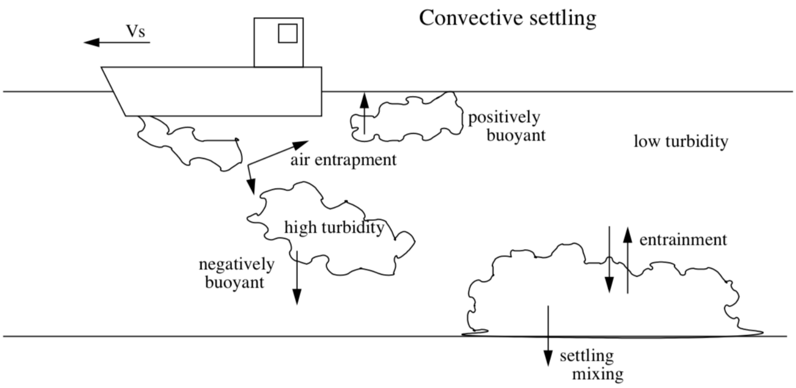


Figure 2.3: Plume cloud

**Passive plume**

Passive plumes are created due to stripping of dynamic plumes by entrainment caused by turbulence. For example, when the ambient current is strong enough, the plume will be mixed fully with the ambient water. Sediment concentrations are relatively low in a passive plume, therefore fine particles settle extremely slow due to the small settling velocity and the higher depth to the seabed compared to the dynamic plume. The zone of impact of the passive plume is very large and is dependent on the magnitude and direction of the ambient currents. An overview is displayed in figure 2.4 [Dankers, 2002].

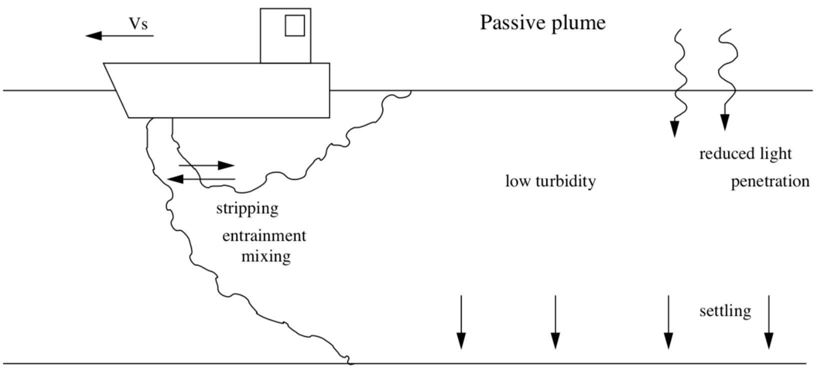


Figure 2.4: Passive plume phase

## 2.3. TURBULENT BUOYANT JET IN AMBIENT CROSSFLOW

As mentioned in section 2.2, the outgoing flow of the overflow forms a negative buoyant jet. The ambient current has effect on the buoyant jet, which will be elaborated in this section. In further notice, a dredging plume is noted as an overflow dredging buoyant jet, because it starts with initial buoyancy and momentum where a plume only starts with buoyancy. However, dredging plume fits better in dredging nomenclature.

When releasing a momentum- and buoyancy source from a round pipe in ambient fluid with uniform flow velocity and mass density, the round negative buoyant jet in crossflow (JICF) is obtained. As long as the jet starts fully turbulent, mixing of a buoyant JICF is not strongly dependent on the jet Reynolds numbers (Re), but primarily governed by the densimetric Froude number ($F_\Delta$) and the jet-to-crossflow velocity ratio ($\lambda$) [Jirka, 2004].

$$F_\Delta = \frac{W_0}{\sqrt{Dg\frac{\Delta\rho}{\rho_w}}} \tag{2.1}$$

$$\lambda = \frac{W_0}{U_{cf}} \tag{2.2}$$

Where $W_0$ is the overflow exit velocity, $U_{cf}$ is the crossflow velocity (vector sum of dredging speed and ambient current), D the plume source pipe diameter (overflow exit diameter in this case) and $\rho_w$ the mass density of the ambient water. $\Delta\rho$ is the excess mass density of solids in ambient fluid which also can be described as $\rho_s$ - $\rho_w$. A schematic overview of mixing of a negative buoyant JICF is shown in figure 2.5 [de Wit, 2015].

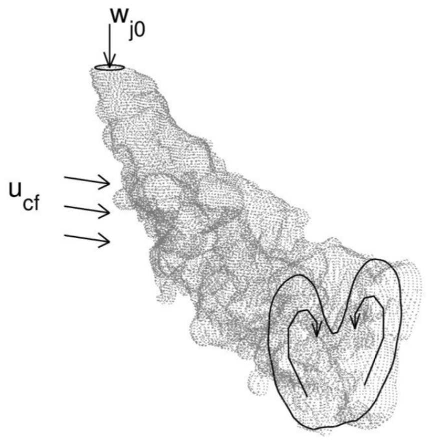


Figure 2.5: Schematic mixing of a negative buoyant JICF

The way the plume spreads out is determined by several possible flow regimes [Wright, 1984], [Fischer *et al.* , 1979]. Jet regime, plume regime and the bent regime are generally found. A perpendicular injected buoyant JICF to the ambient flow starts with no horizontal velocity. Moving further downstream, the ambient current will take the buoyant plume further in the horizontal. The vertical momentum is important at the exit of the overflow, but eventually buoyancy will take over. Fischer *et al.* [1979] derived length scales to distinguish the different flow regimes of a buoyant JICF. The length scales are given by:

$$l_m = \frac{M_0^{3/4}}{B_0^{1/2}} \tag{2.3}$$

$$z_m = \frac{M_0^{1/2}}{U_{cf}} \tag{2.4}$$

$$z_b = \frac{B_0}{U_{cf}^3} \tag{2.5}$$

$$z_c = z_m \left(\frac{z_m}{z_b}\right)^{1/3} \tag{2.6}$$

$M_0$ is the overflow momentum flux ($Q_0 W_0$ where $Q_0 = A_0 W_0$) and $B_0$ is the overflow buoyancy flux ($Q_0 g'$ where $g'$ is the specific gravity ($\frac{\rho_m - \rho_w}{\rho_w} g$)). As said, the length scales determine the flow regime. If z < $l_m$ from the source, a buoyant jet acts as a jet and when z > $l_m$ the buoyant jet acts as a plume. The length scales $z_m$ & $z_b$ are defined for the influence of momentum and buoyancy compared to the ambient current. As long as z < $z_m$, initial momentum is dominant over to the ambient current and so the buoyant jet acts like a jet. If z < $z_b$, initial buoyancy is dominant over the ambient current and so acts as plume.
Independent of momentum- or buoyant dominance, a buoyant JICF always ends as a bent over plume due to the horizontal ambient current (figure 2.5). As long as $z_b > z_m$, the transition to the bent over plume happens after z > $z_b$. In reverse, if $z_m > z_b$, the transition happens after $z_c$. Figure 2.6 [de Wit, 2015] summaries the length scales and the connected flow regimes of a buoyant JICF, as derived by Fischer *et al.* [1979].

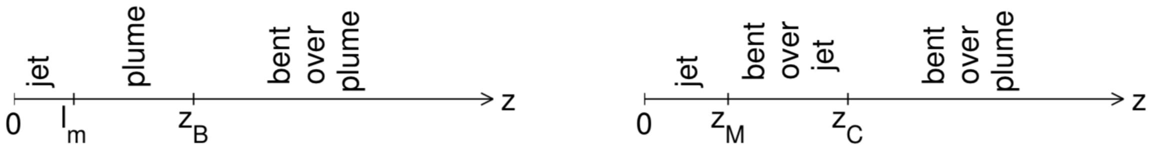


Figure 2.6: Length scales and flow regimes of a buoyant JICF in case $z_b > z_m$ (left) and in case $z_m > z_b$ (right)

Even though the initial relative density difference is usually in the order of 1 to 10%, the buoyancy is relatively weak compared to the crossflow found during dredging operations, with the jet-to-crossflow velocity ratio usually in the range $0.25 < \lambda < 3$ [Decrop, 2016]. Therefore, the momentum length scale $z_m$ is larger than the buoyancy length scale $z_b$ in most cases, leading to a plume regime sequence as shown in figure 2.6 on the right. However, in strong crossflow cases both $z_m$/D and $z_b$/D are around or less than unity, due to which the plume transforms very rapidly to the bent over plume regime.

## 2.4. NEAR FIELD PROCESSES DREDGING PLUME

Near field is defined as the zone where plume mixing is dominated by density differences and interaction with the dredging vessel. Typically, the near field zone ends some hundred meters behind the TSHD. In the far field, plume mixing is mainly governed by sediment settling and ambient (tidal) currents [de Wit, 2015]. The focus of this study is plume mixing in the near field, because near field mixing determines the amount and distribution of suspended sediment available in the far field.

The dredge plume normally contains a non-uniform sediment grain size distribution. The sediment particle diameter ($D_p$) can range from sand ($D_p > 63\ \mu m$) to mud ($D_p < 63\ \mu m$). However, due to the slower settling of finer sediment in the hopper with respect to coarser sediment, the overflow and therefore the exiting plume generally contains more mud and finer particles than the dredged material [van Rhee, 2002].
Under influence of turbulence and differences in settling velocity, mud particles can cluster together to form flocs with typical sizes of 0.01-1mm. The density of mud flocs is less than the density of individual mud particles, however the settling velocity is larger. Flocculation is especially important when the mud concentration is large and therefore strong flocculation has been found for mud fractions inside an overflow plume with floc diameters of 40 - 800$\mu m$ and floc settling velocities of 0.1 - 6mm/s [Smith & Friedrichs, 2011]. Even after flocculation, the mud settling velocity is very small leading to large deposition periods, especially for the mud in the surface plume which can take hours to days before it has deposited at the seabed. Although the overflow plume leaves the vessel at the keel several meters below the water surface, the initial velocity is downward and it is denser than the ambient water (it is negatively buoyant). Already close behind the dredger, a part of the overflow plume can end up fully mixed near the water surface as a surface plume where a surface plume can remain visible for considerable distances from a dredger [Newell *et al.* , 1999].

Generally, buoyant JICF mixing is not responsible for the generation of a surface plume, as it will bring the plume further down - not up. Therefore, other processes are responsible for the generation of a surface plume.

## 2.5. INFLUENCE FACTORS TURBIDITY CREATION

During this research, a total of twelve influence factors are distinguished which are further elaborated in this section. Most litarature is from [de Wit, 2015] and [Decrop, 2016] which both created a 3D computational fluid dynamics (CFD) and 3D large eddy simulation (LES) model to investigate overflow plumes. Designs that decrease turbidity and that are currently available are shown in Appendix A.

**Overflow inlet process**

As noted in chapter 2.1, The filling of the hopper basin has certain phases. When the water level in the overflow is at his maximum, a horizontal flow at the surface flows towards the overflow. During this phase, the overflow losses grow exponentially due to erosion of the sediment bed and increased velocity at the surface. Therefore it is interesting to see if this filling process into the overflow can be changed. Nowadays, an overflow is placed inside the TSHD barge where the water-sediment mixture flows into the overflow and leaves at the bottom of the TSHD. With this setup, a horizontal velocity at the surface is created when the water level reaches the height of the overflow. Looking at the filling process of a TSHD and stripping away the overflow, all sediment particles will settle until the whole barge is filled and the water level reaches his maximum. Without an overflow, the filling process takes far more time which will increase the financial costs dramatically. Looking into this problem, no sufficient literature is found that looks at the filling process of the overflow. Therefore, further investigation has to be done in order to come with sufficient data and comparisons. However, it is noted that in order to decrease the exponential grow of overflow loss, a way should be found to decrease or eliminate the created horizontal velocity induced by the filling process of a TSHD.

**Dredging speed**

Both [Decrop, 2016] and [de Wit, 2015] used their models to see if dredging speed has an influence on the plume trajectory. The dredging speed is related to the jet-to-crossflow velocity ratio ($\lambda$) which connects the overflow exit velocity to the ambient current velocity. In the models, a low $\lambda$ is used to create a high ambient current which represents a high trailing velocity of the TSHD. In both models, a high dredging speed shows a higher amount of sediment mixed towards the surface. Furthermore, a lower dredging speed shows that the bulk of the released sediment moves more rapidly to the seabed, forming a density current and more dilute surface plume. Increasing the dredging speed will lift the plume up towards the surface which can lead to interaction with the propeller and increases the horizontal spreading of the plume.

**Water depth**

In figure 2.7, vertical profiles of $C/C_0$ are given at y = 0 and x/D = 100 (a) and horizontal profiles are shown in the surface plume at y = 0 and at 0.5m below the surface (b). It can be observed that the case with keel clearance ($H_k$) of 5m differs substantially from the other cases. The sediment concentration in the surface plume is about 4 times higher at x/D = 100. In the horizontal profile (figure 2.7b), the concentrations are similar for the cases with $H_k \geq$ 9m, but for $H_k$ = 5m the surface concentration increases significantly at about x/D = 60. Part of this is due to the increase in streamwise velocity with decreasing depth. This location is at 30-40m behind the propellers [Decrop, 2016]. Concluding figure 2.7, water depth does influence the sediment concentration in suspension for $H_k \geq$ 9m, but does not influence the sediment concentration at the water surface.

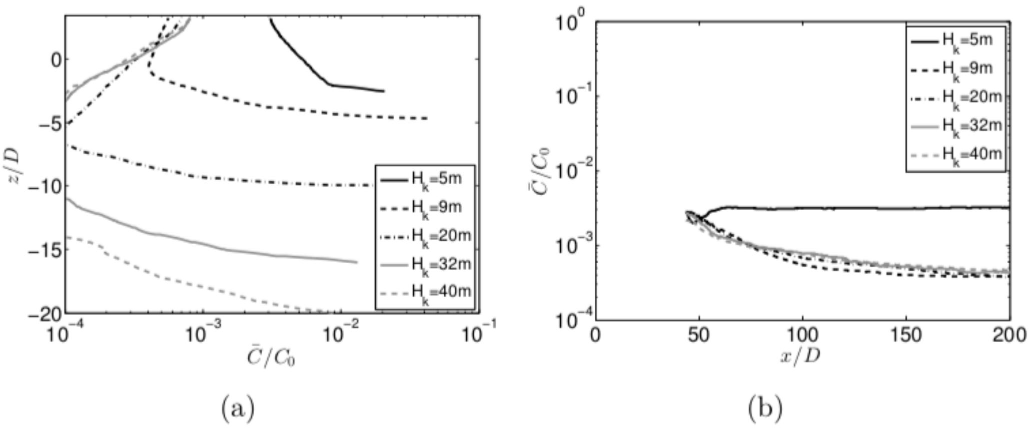


Figure 2.7: Time-averaged sediment concentration $C/C_0$, for identical cases except for the different keel clearance $H_k$. In figure (a), vertical profiles are given at y = 0 and x/D = 100. In figure (b), horizontal profiles are given at y = 0 and at 0.5m below the surface.

de Wit [2015] calculated the vertical distribution of flux of fines in suspension to illustrate the effects of near field conditions like dredging speed, water depth, pulsing and air entrainment. All vertical distributions for situations with low $U_{cf}$ and large depth are strongly concave with the majority of the flux near the bed. For runs with large $U_{cf}$ or smaller depth the curves are less concave. Increasing water depth shows a way better vertical distribution, with more particles found in the lower water column.

**Angle between TSHD and ambient current**

A high crossflow velocity leads to a larger plume flux still in suspension after a certain settling time, more sediment in higher parts of the water column and thus a large surface plume. A high crossflow velocity increases the interaction between the plume and the TSHD hull and the plume and the TSHD propellers. When

a TSHD is sailing under an angle with the ambient current, the overflow plume is pushed towards the side of the TSHD hull where it can be taken along by the expanding flow towards the free surface. The more the ambient current comes from the side, the more surface plume can be expected[de Wit, 2015].
Decrop [2016] investigated the difference between the plume trajectory of the surface plume and the density current of that plume while encountering a crossflow. Results show that the surface plume follows another path and angle comparing to the density current while both clearly feel the crossflow current. The descending density current feels a secondary current induced by the angle between ship and flow. Therefore the density current is diverted towards a higher angle than the crossflow. The angle of the crossflow does show a diverted path of the plume, however, Decrop [2016] showed that the concentration levels of a diverted plume, or a plume with a head on current is not that different. Therefore the angle of the current does not influence the amount of concentration found in the surface plume.

**Pulsing**
A pulsing, discontinuous flow in the overflow has been measured on a field trip [de Wit, 2015]. The pulsing frequency is dependent on the ambient wave period and the dynamic motions of the TSHD. Pulsing has two effects on the dredging plume: it enhances vertical spreading of the plume and it gives a deeper plume path. The deeper plume path is caused by the extra initial inflow momentum compared to a continuous non-pulsed case with similar volume flux. Pulsing can either enhance the formation of a surface plume by the increased vertical spreading or reduce the formation of a surface plume by the deeper plume path which reduces the influence of the TSHD hull and propellers. For a high crossflow velocity it is found that pulsing results in a smaller surface plume and for a low crossflow velocity pulsing results in a larger surface plume [de Wit, 2015].
de Wit [2015] defined a pulsing period ($T_p$) based on a frequency in the range of the Strouhal number ($fD/W_0$) to determine the fluctuation inflow of the overflow. A higher value of the Strouhal number describes a smaller pulsing period and the other way around, a lower value of the Strouhal number describes a larger pulsing period. The pulsing period does not have effect while dredging at high dredging speed. However, at normal dredging speed the increase of pulsing period, so lower Strouhal number, creates separate puffs including gaps. This leads to a general finding where a larger pulsing period increases the surface plume.

**Air**
When the water level inside the vertical overflow shaft is much lower than the water level inside the hopper, the overflowing water forms a plunging jet in the shaft and significant amounts of air can be entrained into the overflow plume. So, the air entrainment and pulsing of the overflow are closely related. There is experimental evidence that a main plume and the air content of this plume will separate into two separate plumes at a certain distance from the source. To visualize the trajectories of the liquid-phase in bubbly jets, dye was injected into the water pipeline upstream of the water pump. [Zhang & Zhu, 2013].
In this study, a total of 12 experimental scenarios were investigated. Based on the amount of air flow rate ($Q_a$) and water flow rate ($Q_w$) it can be seen that when the amount of air injected is increased, the separation height is increased. This means that with the increase of air injected, the plume reaches higher in the water column and shows more vertical spreading over the whole water column. Connecting this to dredging on a TSHD with overflow losses, the influence of air creates a uprising buoyant flow to the water surface which can pick up fine particles and so create a surface plume. Under the influence of gravity, air bubbles are rising, which can be seen as a negative (upward) settling velocity.
The influence of entrained air is conditional, largest influence is found with a low crossflow velocity combined with a large depth. With high crossflow velocity and/or small depth a big surface plume with high turbidity at the free surface can be found, independent of the amount of entrained air [de Wit, 2015].

Decrop [2016] tested the effect of the air bubble reduction, by comparing the simulation with- and without air reduction for two cases: a deep water case and a case with plume sediment mixed throughout the water column based on information form Saremi & Jensen [2014b]. In the case with deep water, the effect of decreasing the air entrainment with 90% shows a drastically decrease of surface concentration of around a factor 20. This can be explained by the absence of the vertical momentum source in the water-sediment mixtures due to the wakes of the rising air bubbles (eq. 2.7). It is noticed that the bulk of the plume is situated deeper with a reduced air concentration. This effect is simply explained by the increased bulk density of the plume when the air volume fraction is lower. The bulk mass density of the water-sediment-air mixture is defined by:

$$\rho_m = (1 - \phi_s - \phi_a)\rho_w + \phi_s\rho_s + \phi_a\rho_{air} \tag{2.7}$$

where $\phi_s$ and $\phi_a$ are the volume fractions of sediment and air and $\rho_m$, $\rho_s$, $\rho_w$ and $\rho_{air}$ are the mass densities of respectively the mixture, the sediment, sea water and air. It can be shown that for an air fraction of 7%, mixtures with $C_0$ up to 13 g/l have a positive buoyancy, which means they are lighter than the surrounding sea water and will flow up to the water surface. For $\phi_a$ = 14% this is even the case up to $C_0$ = 26 g/l [Decrop, 2016].

In the case with more shallow water and a near-bed density current combined with a surface plume, a different result is found. The bulk plume volume cannot descend deeper in the case with air reduction, since it is almost fully mixed throughout the water column. The surface concentrations, however, are also positively affected by the air reduction. However, the effect of air entrainment reduction is still four times better in deep water compared to shallow water.

**Interaction with propeller**

de Wit [2015] used his model to look at the influence of a propeller at both normal- and high dredging speed. It is found that a propeller has almost no influence when dredging at high speeds. At normal speeds, the propeller brings the plume up in the vertical. A propeller lifts the dredging plume up by entrainment into the propeller jet an this entrainment partly blocks the counter rotating vortex pair of the dredging plume. However, there is no indication that significant amounts of the dredging plume are sucked in directly into the propeller [de Wit, 2015].

**Position of overflow**

de Wit [2015] looked at the position of the overflow being in the front of the TSHD or at the back. It is shown that, without propeller the plume concentrations do not differ much with the overflow at the front or at the back. With a propeller the plume has moved upward a little. This effect of the propeller is caused by entrainment into the propeller jet: the dredging plume is sucked upward by this entrainment and fine particles could follow this, depending on particle size diameter, but this is more complex due to hindered settling. When the overflow is at the back, the influence of the propeller is larger, because of the reduced distance between outflow of the dredging plume and the propeller.
Decrop [2016] used his model for the same investigation, however took the position of the overflow relative to the stern with the longitudinal distance between the overflow and stern ($L_o$) and lateral distance ($B_o$) to the ships centerline, which is shown in figure 2.8. Both the influence of $L_o$ and $B_o$ are investigated. In addition, a case with two overflows (one in the front and one in the back) is examined.

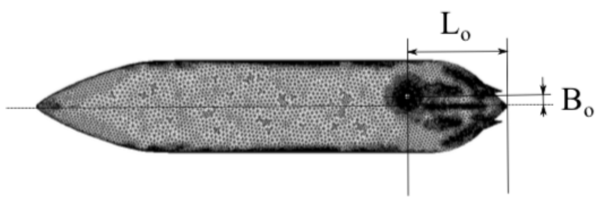


Figure 2.8: Definition of longitudinal- and lateral overflow position $L_o$ and $B_o$

Firstly, the influence of $L_o$ is investigated. It can be assumed that a longer distance $L_o$ is beneficial for the surface plume. When looking at the simulation results of Decrop [2016] for a relatively horizontal plume the longer distance $L_o = 80m$ seems to give the plume more time to detach from the keel and escape the propeller mixing. In this case, a clearly downward density current is visible, with less concentration at the surface. A smaller $L_o = 20m$ ensures the plume to be caught in the uplifting flow of the propeller and mixes the plume. The result is a much more uniform sediment distribution and a higher concentration in the surface plume.
When a more dense plume is released (90 g/l instead of 20 g/l), the impact of the overflow location becomes less important. Due to the more dense plume and so higher concentration, the plume detaches quicker from the hull. Due to this, the mixing of the propeller jet can just be avoided and the surface plume concentration is therefore only slightly higher when having an overflow at the back [Decrop, 2016].

*Shift in lateral distance*
In some vessels, the overflow is not located on the centerline of the vessel. The effect of $B_o$ >0 depends on the geometry of the stern section and of $L_o$. In this case, the strongly curved hull sections near the stern and away from the ship's centerline cause an uplifting flow, taking the plume upwards and causing an increased surface plume concentration. When the overflow is positioned at the centerline, these sloping parts are not encountered by the plume. At least in the geometry with which this model has been set up [Decrop, 2016].

*Two overflows*
In the investigation of Decrop [2016] the difference in amount of overflows is also checked. In this case, the TSHD has overflows at $L_o = 30m$ and $L_o = 80m$ and an equal distributed overflow discharge, by halving the outflow velocity, while maintaining the same diameter D and concentration $C_0$. The result shows a less entrainment of the plumes despite the lower exit velocity $W_0$. The plume with multiple overflows shows a deeper average position and the overall concentrations are also lower. However, it can be assumed that due to the lower concentrations in the two overflows, more particles will be in suspension and the plume is more diluted, which will increase the plume width [Decrop, 2016]. In addition, it could be assumed with a more diluted plume, effects of air bubble rising or interaction with the propeller could increase the the amount of surface plume.

**Overflow sediment load**
The basic dimensionless numbers governing the behaviour of a buoyant jet were identified in section 2.2 as the densimetric Froude number $F_\Delta$ and the velocity ratio $\lambda$. The sediment load in the overflow mixture ($C_0$) has direct influence on $F_\Delta$ and it is therefore expected that $C_0$ has an influence on the trajectory of near-field dredging plumes.
It could be assumed that releasing a higher concentrated mixture leads to less entrainment due to a quicker descent into the ambient water. Evidently, in the field the absolute value of the sediment concentration is of importance. Yet, the question could be raised whether the total amount of sediment brought in suspension during a project could be reduced by releasing a more concentrated mixture. How this could be achieved in practise, is another question.
Decrop [2016] Analyzed the absolute time-averaged concentration C in the surface plume as a function of the released concentration $C_0$. An consistent increase in $C_0$ shows a consistent decrease of sediment concentration in the surface plume (z = 0.5m). Between the stern at x/D = 40 and x/D = 120, the surface plume with $C_0$ = 10 g/l has sediment concentrations about twice as high as the plume with $C_0$ = 150 g/l. Further downstream, the difference becomes smaller, to about a factor 1.5.
This observation leads to the conclusion that releasing a more concentrated water-sediment mixture could reduce the surface plume significantly, however, the total suspended sediment also increases.

**Overflow outflow velocity**
A larger initial overflow velocity brings the overflow plume quicker to the bed, this increases the deposition in the near field and reduces the interaction between the plume and the TSHD hull and the plume and the TSHD propellers. However, an increased overflow velocity also means a larger overflow sediment source flux is brought into suspension [de Wit, 2015]. Based on investigation by de Wit [2015] an increase of overflow exit velocity does not show a large decrease of sediment flux in suspension at the end of the nearfield (X = 350m).

**Overflow shape**
Different studies have shown that non-circular shapes of exit holes of buoyant jets in crossflows have an impact on the jet trajectory. Salewski *et al.* [2008] found that an elliptical jet exit with aspect ratio of 1.69 had a 10% better penetration in the crossflow compared to a circular hole with the same surface area (at x/D = 10). Haven & Kurosaka [1997] also showed that high-aspect ratio openings enhance the crossflow penetration.
These findings lead to the question whether an overflow opening with higher aspect ratio could improve the plume outflow from the TSHD keel wall. Decrop [2016] simulated two test cases with a rectangular overflow cross section. The surface area of the rectangular cases was identical to the reference cases with D = 2m shafts. The rectangular shafts were 3m in length (along ship axis) and $\pi/3$m in width. The aspect ratio of the rectangular overflow shaft is therefore equal to $\pi$. All other conditions were kept constant.

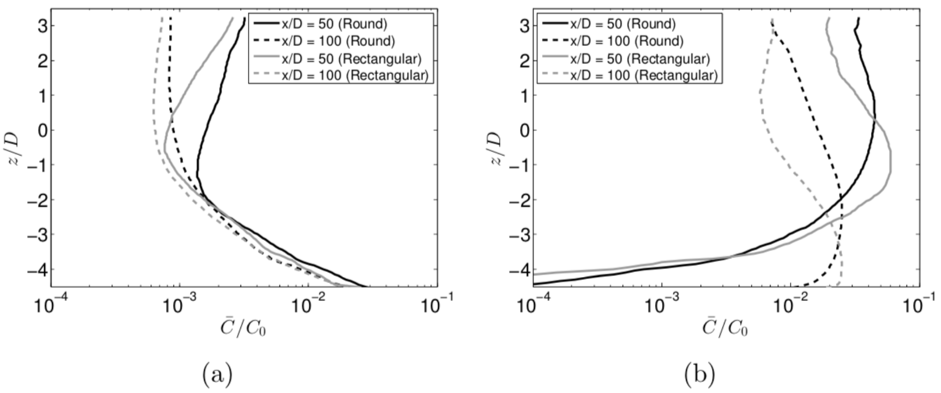


Figure 2.9: Time-averaged sediment concentration $C/C_0$, for 2 cases in which a round overflow shaft was compared with a rectangular shape. For both shapes the cross-sectional area of the overflow shaft was equal to $\pi$. In (a), $U_0$ = 1 m/s, $C_0$ = 55 g/l and $W_0$ = 1.9 m/s. In (b) $U_0$ was increased to 3 m/s

Decrop [2016] simulated the first case (figure 2.9a) which was clearly a type of density current ($U_0$ = 1 m/s, $C_0$ = 55 g/l and $W_0$ = 1.9 m/s) with a distinct surface plume. With a round overflow shaft, the sediment concentrations in the upper half of the water column are about 25% to 50% higher compared to the case with rectangular overflow. It seems that the shape of the overflow shaft does have an influence in the lower half of the water column. Either the higher aspect ratio in the rectangular case leads to a better escape from the keel, or the more narrow shape of the plume after exit might reduce the number of air bubbles that escape per unit of time, leading to less surface plume generation in the first few meters after the exit.
In the second case (figure 2.9b), the crossflow velocity was increased to $U_0$ = 3 m/s. It is determined in this test case whether a high-aspect ratio overflow shaft would lead to a reduction of the surface plume concentration. At x/D = 50, it can clearly be observed that the bulk of the plume is situated lower for the rectangular case compared to the round shaft. The surface concentration is 40% lower in the rectangular case. After x/D = 100, the difference in concentration near the surface has reduced, but it is clear that less sediments are present in the water column in the near-field overflow plume.
The influence of the shape of the overflow shaft needs more investigation to draw definite conclusions, but it seems that variations in the aspect ratio of the shaft cross section have the potential to reduce the sediments in suspension in the overflow plume.

**Extension of overflow**
As shown earlier, the water depth and propeller have influence on the plume dispersion while dredging. Both de Wit [2015] and Decrop [2016] investigated therefore an extension of the overflow to bring the outflow of the overflow deeper, so bring the sediment closer to the bed, and reduce impact of the propeller. de Wit [2015] investigated three overflow extensions for dredging in a depth of 25m:

- Short extension of 3m long
- Medium long extension of 8m long
- Long extension of 16m long (1m above seabed)

de Wit [2015] tested two overflow locations: 100m- and 40m in front of the TSHD aft. In the base case, without an overflow extension, the plume spreads over the complete zone below the keel and suspended sediment clouds of SSC > 100 mg/l touch the keel. A 3m extended overflow has limited influence on the instantaneous SSC distribution, but a 8m extension results in a zone free of suspended sediment below the keel of the TSHD. The 16m overflow extension brings the sediment right at the bed without mixing, but then the sediment is re-suspended up in the water column by the air fraction from the overflow mixture and the turbulent interaction between the vertical overflow extension and the crossflow. This re-suspension is so strong that some puffs of suspended sediment reach the keel of the TSHD before the sloping aft of the TSHD. The re-suspension caused by air of the 16m overflow extension is larger than the re-suspension by air of the 3m and 8m extensions. These two extensions have downward momentum leading to more separation of the air from the sediment-water mixture than with the 16m extension which has horizontal outflow.

Decrop [2016] made a case with his model to verify the findings of de Wit [2015]. In addition, the overflow was positioned near the stern of the ship, with a lateral shift of $B_o$ = 4m. It was shown that a lateral shift, and an overflow in the back, were both unfavourable for the creation of surface plumes. Decrop [2016] compared two overflow extensions (3m, 5m) with a base case without extension.
Based on the results of Decrop [2016], it can clearly observed that in the case with no extension, the overflow plume moves completely to the surface. With an extension length of 3m, the main plume is allowed to escape the uplifting effect of the curved stern sections, but a relatively high sediment concentration remains present in a surface plume. This can be explained by the fact that the plume was not deep enough to escape the propeller jet. For an extension length of 5m, the plume escapes both the uplifting of the stern and the propeller jet mixing. The main plume descends steadily towards the sea bed. Air bubbles still have an influence, which cannot be avoided unless an over overflow extension is combined, for example, with an environmental valve. However, it is noted that an environmental valve is inefficient with an lateral shift of the overflow [Decrop, 2016].
Additionally, Decrop [2016] made an overview of the vertical $C/C_0$ profiles for the different extension lengths. It can be observed that the maximum concentration in the plumes remains similar, but that the plume center is deeper for longer extension lengths. The difference between the depth of the concentration for extension lengths 3m and 5m is larger then the difference in extension length (2m). More important is the fact that the surface concentration decreases a factor 2.5 with a 3m extension and a factor 5 with a 5m extension. When looking further downstream, the same pattern is found, where plumes with increasing extension are deeper and have a lower surface concentration.

### 2.5.1. CONCLUSION

In the past paragraph, twelve factors are investigated and shortly described which decrease the surface turbidity of overflow losses on a TSHD. Based on the research, it is concluded that certain influence factors can decrease the surface plume significantly. In this master thesis, the focus of APT Offshore was to look at a passive system that can be implemented at current TSHD's. In combination with the testing possibilities at TU Delft, it is chosen to investigate the **overflow shape** further to see if the change in overflow shape does decrease the surface plume which was estimated by [Decrop, 2016].

This leads to the following research question:

***Can a change in overflow shape cause a decrease of the surface plume***

This question is answered by doing experimental tests in stable water with concentration- and angle measurements in order to find the shear entrainment coefficient. In addition, this entrainment coefficient is used to give an indication of the plume trajectory with the JETLAG model from [Lee & Chu, 2003].

# 3

# Plume dispersion with circular and plane outflow shape

*Now that the change of overflow shape is chosen to investigate further, an analytical description and in depth study is done regarding the literature of outflow shapes. All of this chapter is found in* Lee & Chu [2003] *where a difference is made between four options: round jet, round plume, plane jet and plane plume. The difference between jets and plumes is that a jet is a continuous source of momentum, whereas a plume is a continuous source of buoyancy. The case of a plane jet is more extensive featured, where the other are shorter elaborated, because the method complies in the other cases, with a few differences and all literature is found in* Lee & Chu [2003] *as said before.*

*For all four cases, the entrainment coefficient* ($\alpha_G$) *and velocity- to concentration width ratio* ($\lambda_r$) *are described and determined. The entrainment coefficient relates to the spreading rate* ($\beta_G$) *which is determined by experiments. Section 3.1 displays the analytical background of a jet, where section 3.2 displays the analytical background of plumes. Section 3.3 gives a summary of all relations needed for the experiments.*

## 3.1. JETS

This section displays the analytical background of jets with a plane- and round outflow shape.

### 3.1.1. PLANE JET

Looking at the inflow of a continuous source of momentum two different zones are noted: Zone of Flow Establishment (ZFE) and Zone Established Flow (ZEF) which can be seen in figure 3.1 in case of a plane outflow shape.

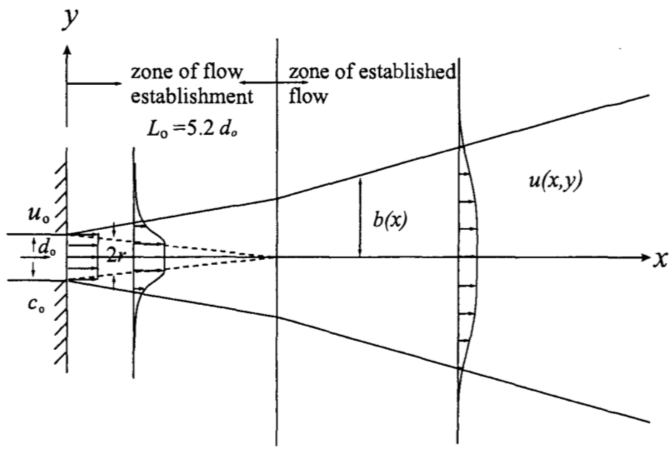


Figure 3.1: Zone of Flow Establishment (ZFE) and Zone Established Flow (ZEF) in case of a plane jet

The velocity and concentration in the potential core of the ZFE are constant. Surrounding the potential core is the mixing layer. The exchange of momentum between the core and the surrounding fluid across the mixing layer leads to the profiles in the mixing layer as follows:

$$
\begin{aligned}
u(x,y) &= u_0 * exp[\frac{-(y-r)^2}{b^2}]; y > r \\
c(x,y) &= c_0 * exp[\frac{-(y-r)^2}{(\lambda_r b)^2}]; y > r
\end{aligned}
\tag{3.1}
$$

$$
\begin{aligned}
u(x,y) &= u_0; y < r \\
c(x,y) &= c_0; y < r
\end{aligned}
\tag{3.2}
$$

where r(x) = half-width of the potential core, b(x) = half-width of the mixing layer, u(x,y) = velocity, c(x,y) = concentration, and y = lateral distance from the center line. The parameter $\lambda_r$ is introduced to account for the difference between the diffusion of mass and diffusion of momentum. The width of the concentration profile $\lambda_r$b(x) is generally wider than the width of the velocity profiles b(x) at the end of the potential core (r → 0).

In the Zone of Established Flow (ZEF),when the turbulence has penetrated to the centerline, the velocity and concentration distributions are self-similar and can be well approximated by Gaussian distributions:

$$
\begin{aligned}
u(x,y) &= u_m * exp[\frac{-y^2}{b^2}]; x > 5.2d_0 \\
c(x,y) &= c_m * exp[\frac{-y^2}{(\lambda_r b)^2}]; x > 5.2d_0
\end{aligned}
\tag{3.3}
$$

where $u_m$(x) and $c_m$(x) are the velocity and concentration maxima along the centerline. The width of the jet, b(x), is defined at a lateral location where the x-component of the velocity is equal to 1/e of the centerline value. Experimental measurements of plane jet by Albertson *et al.* [1950], Miller & Comings [1957] and Bradbury [1957] found the jet spreads linearly with a growth rate $\frac{db}{dx} \simeq 0.1$.

### Governing Equations

The governing equations for the steady incompressible turbulent mean flow of the jet are the continuity equation (3.4), the momentum equations (3.5) and the mass conservation equation (3.6). The reference frame is the same as figure 3.1.

$$\frac{\partial u}{\partial x} + \frac{\partial v}{\partial y} = 0 \tag{3.4}$$

$$\begin{aligned} \rho u \frac{\partial u}{\partial x} + \rho v \frac{\partial u}{\partial y} &= -\frac{\partial p}{\partial x} - \frac{\partial \rho \overline{u'^2}}{\partial x} - \frac{\partial \rho \overline{u'v'}}{\partial y} \\ \rho u \frac{\partial v}{\partial x} + \rho v \frac{\partial v}{\partial y} &= -\frac{\partial p}{\partial y} - \frac{\partial \rho \overline{u'v'}}{\partial x} - \frac{\partial \rho \overline{v'^2}}{\partial y} \end{aligned} \tag{3.5}$$

$$u \frac{\partial c}{\partial x} + v \frac{\partial c}{\partial y} = -\frac{\partial \overline{u'c'}}{\partial x} - \frac{\partial \overline{v'c'}}{\partial y} \tag{3.6}$$

where (u, v) = mean velocity, c = mean concentration (mass per unit volume), p = pressure, and $\rho$ = fluid density; the prime denote the turbulent fluctuations and overbar the time average of the fluctuations. The boundary conditions for a free jet are shown in equation 3.7 for $y \to \pm\infty$. With these boundary conditions the jet is assumed to be free from solid boundary and ambient current effects.

$$\begin{aligned} &u \to 0 \\ &\overline{u'v'} \to 0 \\ &\overline{u'c'} \to 0 \end{aligned} \tag{3.7}$$

Furthermore, since b ≪ x, by continuity v ≪ u and $\frac{\partial}{\partial x} \ll \frac{\partial}{\partial y}$ , the pressure $p$ is approximately constant and $\frac{\partial p}{\partial x} \approx \frac{\partial p}{\partial y} \approx 0$. Hence,

$$p + \rho \overline{v'^2} \simeq p_\infty \tag{3.8}$$

from the boundary-layer approximation of the y-momentum equation (3.5). Which leaves three equations which are subjected to the same boundary conditions as specified before. Thus there are three variables of the mean flow (u,v,c) and three governing equations (3.4, 3.5 in x direction and 3.6). But the turbulent covariances ($\overline{u'v'}, \overline{v'c'}$) are the additional unknowns due to the separation of the flow into mean and fluctuation parts. Therefore a turbulence model must be introduced to relate these covariances with the mean flow.

### Integral equations

A one-dimensional procedure to achieve the turbulent closure of the problem is to integrate across the turbulent jet. First, the x-momentum equation is re-written to a conservative form. Since,

$$\rho u \frac{\partial u}{\partial x} + \rho v \frac{\partial u}{\partial y} = \frac{\partial \rho u^2}{\partial x} + \frac{\partial \rho u v}{\partial y} - \rho u \left(\frac{\partial u}{\partial x} + \frac{\partial v}{\partial y}\right) \tag{3.9}$$

The x-momentum equation (3.5) becomes: (when using equation 3.8)

$$\frac{\partial \rho u^2}{\partial x} + \frac{\partial \rho u v}{\partial y} + \frac{\partial \rho \overline{u^2}}{\partial x} - \frac{\partial \rho \overline{v^2}}{\partial x} = -\frac{\partial \rho \overline{u'v'}}{\partial y} \tag{3.10}$$

Using the boundary condition and integrating across the jet, from y = - ∞ to y = + ∞, equation 3.10 becomes:

$$\begin{aligned}
&\int_{-\infty}^{\infty}(\frac{\partial\rho u^2}{\partial x}+\frac{\partial\rho uv}{\partial y}+\frac{\partial\rho\overline{u^2}}{\partial x}-\frac{\partial\rho\overline{v^2}}{\partial x})dy=\int_{-\infty}^{\infty}(-\frac{\partial\rho\overline{u'v'}}{\partial y})dy\\
&\frac{\delta}{\delta x}\int_{-\infty}^{\infty}\rho u^2+\rho(\overline{u'^2}-\overline{v'^2})dy+[\rho uv]_{-\infty}^{\infty}=[-\rho\overline{u'v'}]_{-\infty}^{\infty}\\
&\frac{\delta}{\delta x}\int_{-\infty}^{\infty}[\rho u^2+\rho(\overline{u'^2}-\overline{v'^2})]dy=0
\end{aligned} \tag{3.11}$$

Equation 3.11 shows that the momentum flux is preserved and the plane jet is a line source of momentum flux. If $M$ is the momentum flux per unit length, equation 3.11 becomes:

$$M=\int_{-\infty}^{\infty}[\rho u^2+\rho(\overline{u'^2}-\overline{v'^2})dy] \tag{3.12}$$

Similarly for the mass conservation, using previous steps shown for the momentum equation, finally we get:

$$\frac{\delta}{\delta x}\int_{-\infty}^{\infty}[uc+\overline{u'c'}]dy=[-\overline{v'c'}]_{-\infty}^{\infty} \tag{3.13}$$

The right hand side would be zero if the concentration (c) is the concentration excess above its value in the ambient and hence that the excess mass flux is constant. If $\Gamma$ is this excess mass flux per unit length of the plane jet, equation 3.13 becomes:

$$\Gamma=\int_{-\infty}^{\infty}[uc+\overline{u'c'}]dy \tag{3.14}$$

Measurements show that the two turbulence quantities in equation 3.11 are of the same order [Miller & Comings, 1957]. If the longitudinal fluxes due to turbulent advection are ignored we get:

$$M\approx\int_{-\infty}^{\infty}[\rho u^2]dy \tag{3.15}$$

$$\Gamma\approx\int_{-\infty}^{\infty}[uc]dy \tag{3.16}$$

These approximated form of equations, since the parts of fluxes due to turbulent advection are ignored, are used in the next sections.

**Eulerian integral model**

The turbulence model of the turbulent jet is based on the assumption of the Gaussian profiles, shown in equations 3.2 & 3.3. In this subsection, the calculations for the ZEF are considered. Based on the velocity- and concentration profiles in equation 3.3, the specific or kinematic momentum flux ($M/\rho$) and the mass flux are functions of the width of the jet ($b$), the maximum velocity ($u_m$) and the maximum concentration ($c_m$) as follows:

$$\frac{M}{\rho}=\int_{-\infty}^{\infty}[u^2]dy=\sqrt{\frac{\pi}{2}}u_m^2 b \tag{3.17}$$

$$\Gamma=\int_{-\infty}^{\infty}[uc]dy=\sqrt{\frac{\pi\lambda_r^2}{1+\lambda_r^2}}u_m c_m b \tag{3.18}$$

Equating the expressions in the above equations to the flux at the source, $M=u_0^2 d_0$ and $\Gamma=u_0c_0d_0$ and assuming $b=\beta_G x$, a relation between the centerline velocity ($\frac{u_m}{u_o}$) and centerline concentration ($\frac{c_m}{c_0}$) can be distinguished.

$$\frac{u_m}{u_o}=\sqrt{\frac{2d_0}{\pi\beta_G x}} \tag{3.19}$$

$$\frac{c_m}{c_o} = \sqrt{\frac{1+\lambda_r^2 d_o}{\lambda_r^2 \beta_G \sqrt{2\pi} x}} \tag{3.20}$$

where $\lambda_r$ is the ratio of concentration-to-velocity width, $b$ is the half-width of jet/plume, $\beta_G$ the spreading rate based on the Gaussian velocity profile and $d_0$ the plane width. The subscripts ($_{m}$,$_{0}$) denote the centerline maximum and source. The volume flux (per unit length of the plane exit) $Q$ at a distance $x$ from the source is greater than the volume flux $Q_0$, which is the jet dilution in order to fulfill the momentum conservation.

$$Q = \int_{-\infty}^{\infty} [u] dy = \sqrt{\pi} u_m b = [\sqrt{2\pi}\beta_G]^{\frac{1}{2}} [\frac{x}{d_0}]^{\frac{1}{2}} u_0 d_0 \tag{3.21}$$

With the centerline dilution ratio:

$$S = \frac{Q}{Q_0} = [\sqrt{2\pi}\beta_G]^{\frac{1}{2}} [\frac{x}{d_0}]^{\frac{1}{2}} \tag{3.22}$$

The jet spread rate $\beta_G$ has to be determined experimentally. The ratio between velocity and concentration width $\lambda_r$ is determined in experiments by Kotsovinos & List [1977] which give a value of $\lambda_r = 1.35$.

**Entrainment Hypothesis**

The closure problem can also be looked at a different way. Integrating the continuity equation across the jet:

$$\frac{\delta Q}{\delta x} = \frac{\delta}{\delta x}\int_{-\infty}^{\infty} [u] dy = [-v]_{-\infty}^{\infty} = 2v_e \tag{3.23}$$

Where $v_e (= |v|_{y=\pm\infty})$ is the entrainment velocity. In this case, the closure problem says something about the entrainment velocity and its relationship to the local jet characteristics. By integrating equation 3.21 and using the solution for $Q(x)$:

$$\begin{aligned} \frac{\delta Q}{\delta x} &= \frac{(\sqrt{2\pi}\beta_G)^{\frac{1}{2}}}{2} u_0 (\frac{d_0}{x}) \\ &= 2(\frac{\sqrt{\pi}\beta_G}{4}) u_m \end{aligned} \tag{3.24}$$

Comparing equation 3.23 & 3.24 it shows that the entrainment velocity is proportional to the local jet centerline velocity. This means that the closure problem could be solved by beginning the assumption that $v_e = \alpha_G u_m$, where $\alpha$ is the entrainment coefficient, and solve the continuity, momentum ans mass conservation equations. In many buoyant jet problems, turbulent closure can be solved by this entrainment hypothesis proposed by Morton & Turner [1956]. The entrainment factor can be obtained by experiments and depends on the spreading rate $\beta_G$ in the case of 2D plane jet.

$$\alpha_G = \frac{\sqrt{\pi}}{4}\beta_G \tag{3.25}$$

### 3.1.2. ROUND JET

In case of a round shape and a continuous source of momentum, the ZFE and ZEF are slightly different, which can be seen in figure 3.2.

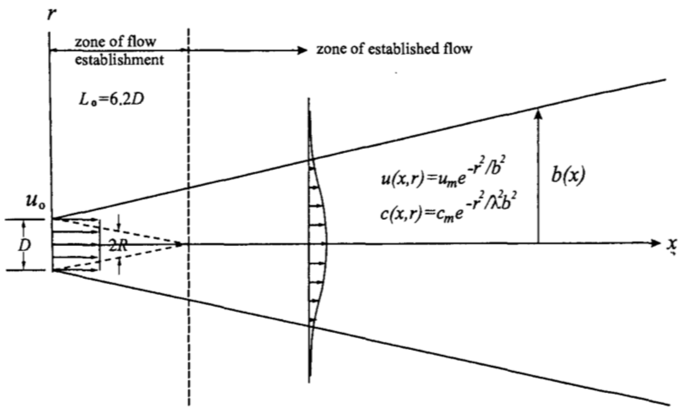


Figure 3.2: Zone of Flow Establishment (ZFE) and Zone Established Flow (ZEF) in case of a round jet

The general experimental features described in section 3.1 also apply for the case of a round jet. The diffusion thickness spreads linearly, static pressure is approximated constant and so the same boundary layer approximations can me made. Again the velocity and concentration profiles can be described according to figure 3.2.

In the ZFE, $x \leq 6.2D$:

$$\begin{aligned} u &= u_0; r \leq R \\ c &= c_0; r \leq R \end{aligned} \tag{3.26}$$

$$\begin{aligned} u &= u_0 * exp[-\frac{(r-R)^2}{b^2}]; r \geq R \\ c &= c_0 * exp[-\frac{(r-R)^2}{\lambda_r^2 b^2}]; r \geq R \end{aligned} \tag{3.27}$$

For $x \geq 6.2D$ also known as the ZEF:

$$\begin{aligned} u &= u_m * exp[-(\frac{r}{b})^2] \\ c &= c_m * exp[-(\frac{r}{\lambda_r b})^2] \end{aligned} \tag{3.28}$$

Where (x,r) are the streamwise and radial coordinates and $u_m(x)$ and $c_m(x)$ are the centerline maximum velocity and concentration. Also the assumption holds that the turbulent round jet spreads linearly with $b = \beta_G x$. Because the round jet is a 3D case, the momentum-, continuity- and mass conservation equations are changed to a (x,r) coordinate system. Showing below are the continuity equation (3.29), momentum equation in x-direction (3.30) and the mass conservation equation (3.31).

$$\rho\frac{\delta u}{\delta x} + \rho\frac{1}{r}\frac{\delta}{\delta r}(rv) = 0 \tag{3.29}$$

$$\rho u\frac{\delta u}{\delta x} + \rho v\frac{\delta u}{\delta r} = -\frac{1}{r}\frac{\delta}{\delta r}(r\rho\overline{u'v'}) \tag{3.30}$$

$$u\frac{\delta c}{\delta x} + v\frac{\delta d}{\delta r} = -\frac{1}{r}\frac{\delta}{\delta r}(r\overline{v'c'}) \tag{3.31}$$

Lee & Chu [2003] evaluated the derivation the same way as with a plane jet, by solving the momentum flux the same way showed in section 3.1 and so find the centerline velocity ($\frac{u_m}{u_0}$), centerline concentration ($\frac{c_m}{c_0}$) and dilution ($S$). $\lambda_r$ is determined in experiments by Papanicolaou & List [1988] and showed a value of $\lambda_r = 1.2$ in case of a round jet.

**Entrainment Hypothesis**
Same as the plane jet, the entrainment hypothesis is applicable for a round jet. By using the same method described for the plane jet, and so integrate the continuity equation across the jet, it can be shown that:

$$\frac{\delta Q}{\delta x} = \frac{\delta}{\delta x}(\pi u_m b^2) = 2\pi(r v) = Q_e \tag{3.32}$$

Where the right hand side represents the local entrainment flux into the jet. By defining the inflowing entrainment velocity at r = b as the entrainment velocity ($v_e$) and use the entrainment hypothesis as shown in section 3.1, the entrainment velocity is assumed to be proportional to the centerline velocity by the entrainment coefficient $\alpha$. Similar to the 2D plane case, it can be shown that the entrainment coefficient depends on the spreading rate, in the case of a 3D round jet.

$$\alpha_G = \frac{\beta_G}{2} \tag{3.33}$$

## 3.2. PLUMES
This section displays the analytical background of plumes with a plane- and round outflow shape.

### 3.2.1. PLANE PLUME
The flow generated by a line source of buoyancy is called a plane plume. The flow in this plume is governed by the buoyancy flux per unit length of the source. Consider the flow generated by a line source of buoyancy at z=0, in stagnant ambient fluid of constant density $\rho_a$. The motion is sustained by a steady constant buoyancy flux $F_0 = \int_{\infty}^{\infty} \frac{\Delta\rho}{\rho} g w dy$ at z=0. Here the continuity-, momentum- and mass conservation equations for the plume are described in the y-z plane, where z is upward positive from the source.

$$\frac{\delta w}{\delta z} + \frac{\delta v}{\delta y} = 0 \tag{3.34}$$

$$w\frac{\delta w}{\delta z} + v\frac{\delta w}{\delta y} = -\frac{\delta \overline{w'v'}}{\delta y} - \frac{\rho - \rho_a}{\rho_a} g \tag{3.35}$$

$$w\frac{\delta c}{\delta z} + v\frac{\delta c}{\delta y} = -\frac{\delta \overline{v'c'}}{\delta y} \tag{3.36}$$

By again assuming a linear spreading rate with $\beta = \frac{dB}{dz}$, experiments from Kotsovinos & List [1977] showed a relation between the entrainment coefficient and the spreading rate as follows, based on the Gaussian velocity profile for a plane plume. Next to that, a value of $\lambda_r = 1.35$ in case of a plane plume.

$$\alpha_G = \frac{\sqrt{\pi}}{2}\beta_G \tag{3.37}$$

### 3.2.2. ROUND PLUME
The round plume is produced by a steady and continuous source of buoyancy. In the case of the jet, the velocity $w(z, r)$ and concentration $c(z, r)$ field of the plume are calculated as function of upward direction $z$ and radial direction $r$. The round plume is good distributed by a Gaussian velocity profile, which simplifies the problem to the prediction of the maximum velocity ($w_m$) the width ($b$) and the maximum concentration ($c_m$) as a function of the upward distance z from the source.

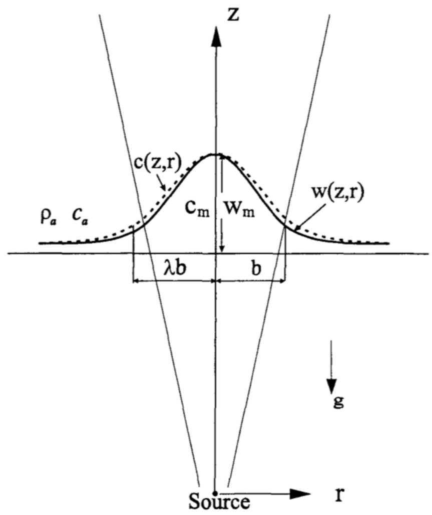


Figure 3.3: Mean velocity- and concentration profiles in case of round plume. The width of the concentration profile is noted by $\lambda b$ where $b$ is the width of the velocity profile

Neglecting effects of initial momentum flux and the size of the source, the width of the plume ($b$) depends on its buoyancy flux at the source $B_0$, the ambient fluid density $\rho_a$ and the distance from the source $z$. Same as seen before, the relation holds that the plume spreads linearly with $b = \beta_G z$. The profile shown in figure 3.3 relates to the following velocity- and concentration profiles (eq 3.38) in the established flow, where the velocity the width of the plume ($b$) is defined by location with velocity $e^{-1} * w_m$.

$$\begin{aligned} w(z,r) &= w_m(z)e^{-(\frac{r}{b})^2} \\ c(z,r) &= c_m(z)e^{-(\frac{r}{\lambda b})^2} \end{aligned} \tag{3.38}$$

The governing continuity- (3.39), momentum-(3.40) and mass conservation (3.41) turbulent incompressible equations in coordinate system (z,r) are defined as follow:

$$\frac{\delta w}{\delta z} + \frac{1}{r}\frac{\delta}{\delta r}(rv) = 0 \tag{3.39}$$

$$\rho(w\frac{\delta w}{\delta z} + v\frac{\delta w}{\delta r}) = -\rho g - \frac{\delta p}{\delta z} - \rho\frac{1}{r}\frac{\delta}{\delta r}(r\overline{w'v'}) \tag{3.40}$$

$$w\frac{\delta c}{\delta z} + v\frac{\delta c}{\delta r} == -\frac{1}{r}\frac{\delta}{\delta r}(r\overline{v'c'}) \tag{3.41}$$

Where $w, v$ are the turbulent mean velocities in vertical and radial direction (z,r) and $w', v', c'$ are the velocity and concentration fluctuations. Assuming a hydrostatic pressure distribution ($\frac{\delta p}{\delta z} = -\rho_a * g$) and adding the Boussinesq approximation, which says that for small densities differences ($\frac{\Delta\rho}{\rho} \ll 1$) density differences can be neglected and so $\rho \approx \rho_a$, except in terms where the the pressure is multiplied with the gravity acceleration $g$. Using this approximation, the momentum equation (3.40) becomes:

$$w\frac{\delta w}{\delta z} + v\frac{\delta w}{\delta r} = -\frac{(\rho - \rho_a)}{\rho_a}g - \frac{1}{r}\frac{\delta}{\delta r}(r\overline{w'v'}) \tag{3.42}$$

Same as found in section 3.1, using integral model equations and the entrainment hypothesis, by solving the volume-, buoyancy- and momentum flux, a relation between the width and entrainment coefficient ($\alpha_G$) is found. Experiments by Papanicolaou & List [1988] showed a concentration-to-velocity ratio for a round plume of $\lambda_r = 1.06$, however, a value of $\lambda_r = 1.19$ is suggested for the entire jet and plume range.

$$b = \frac{6\alpha_G}{5} z \tag{3.43}$$

By combining equation 3.43 and the fact that the plume spreads linearly with $b = \beta_G z$, an expression for the entrainment coefficient is found in case for a round plume.

$$\alpha_G = \frac{5\beta_G}{6} \tag{3.44}$$

## 3.3. SUMMARY

Most importantly, from literature and studying Lee & Chu [2003], the entrainment coefficient ($\alpha_G$) and the concentration- to velocity width ratio ($\lambda_r$) are described and determined in this chapter. An overview for all cases are shown in table 3.1.

| | **Round Jet** | **Round Plume** | **Plane Jet** | **Plane Plume** |
|---|---|---|---|---|
| **Entrainment coefficient** ($\alpha_G$) | $\frac{\beta_G}{2}$ | $\frac{5}{6}\beta_G$ | $\frac{\sqrt{\pi}}{4}\beta_G$ | $\frac{\sqrt{\pi}}{2}\beta_G$ |
| **Velocity- to concentration width ratio** ($\lambda_r$) | 1.19 | | 1.35 | |
| **Velocity width** ($b$) | $\beta_G z$ | | | |

Table 3.1: Overview of all entrainment coefficients and concentration- to velocity width ratios in case of round jet, round plume, plane jet and plane plume

These values say something about the plume exiting from a round shape of a plane shape. In the experiments, these two shapes are tested to measure the differences and also the aspect ratio is investigated in case of a plane shape to see if a higher aspect ratio has a positive or negative influence on the plume. This can be measured in both directions of the nozzle shape (by turning the nozzle 90 degrees). In the experiments, the concentration width is calculated by using the measured angles. With the concentration width, the velocity width and so $\beta_G$ can be calculated following table 3.1. When $\beta_G$ is known, the entrainment coefficient can be calculated. This entrainment coefficient says something about the amount of entrainment between the plume and the ambient water. A higher value denotes more entrainment and so a wider / less concentrated plume, which is easier transported due to a current or air bubbles that will rise the plume. This entrainment coefficient is therefore used in the JETLAG model, that gives in indication of the the plume that is tested in the experiments when it interacts with a crossflow. This model is further elaborated in chapter 6.

# 4

# Experimental Setup

*As there is no experimental data of different overflow shapes, the main priority is to test various overflow shapes. Thanks to previous research done at the Technological University of Delft, a 25$m^3$ rectangular reservoir was available to do experimental tests. A physical description of the test setup is given in section 4.1. Next to that, several parameters are explained, which determine the way of testing, in section 4.2 and the way of data obtainment is shown in section 4.3. All experimental scenario's are shown in section 4.4 which give the values of parameters used. To do the experiments efficient and in a controllable way, a chronological work plan is made which can be found in Appendix B. The main focus of the experiments are:*

- *Try three different overflow shapes (round & two different rectangular aspect ratios) and see by concentration measurements if the concentration distribution is different.*
- *By video imaging, the angle of the plume is obtained which can be translated to an entrainment factor which explains the amount of entrainment between the plume and surrounding water. This entrainment coefficient is important because is it used in the JETLAG model which gives an indication of the plume with a certain amount of crossflow. This model is further elaborated in chapter 8.*

## 4.1. PHYSICAL DESCRIPTION EXPERIMENTAL SETUP

In this section, all parts that make the experimental setup are described. A schematic overview of the used test setup is shown in Appendix C.

**Reservoir**

A $25m^3$ rectangular reservoir is used to perform several experimental tests which is shown in figure 4.1. During the tests, the reservoir is filled with tap water. At the top, a frame is positioned to slide the overflow in the right place. The tests can be visually assessed by the glass windows on the reservoir.

Figure 4.1: $25m^3$ rectangular reservoir at TU Delft

**Mixing tank**

The mixing tank (1.5m x 0.78m x 1m) is a perspex tank which is divided in two equal sections which both have a volume of approximately 500L. In one section, water and sediment are mixed to reach a certain mixture density which is done by hand in combination with a submersible pump. This mixture is pumped from the mixing tank with a small stainless steel flexible impeller pump, with a maximum flow of 20L/min, to the reservoir through a 10mm (inside)diameter pipe. During an experimental test, the other section of the mixing tank can be prepared for the next run and so create another mixture, this to decrease preparation time during testing. An overview is shown in figure 4.2.

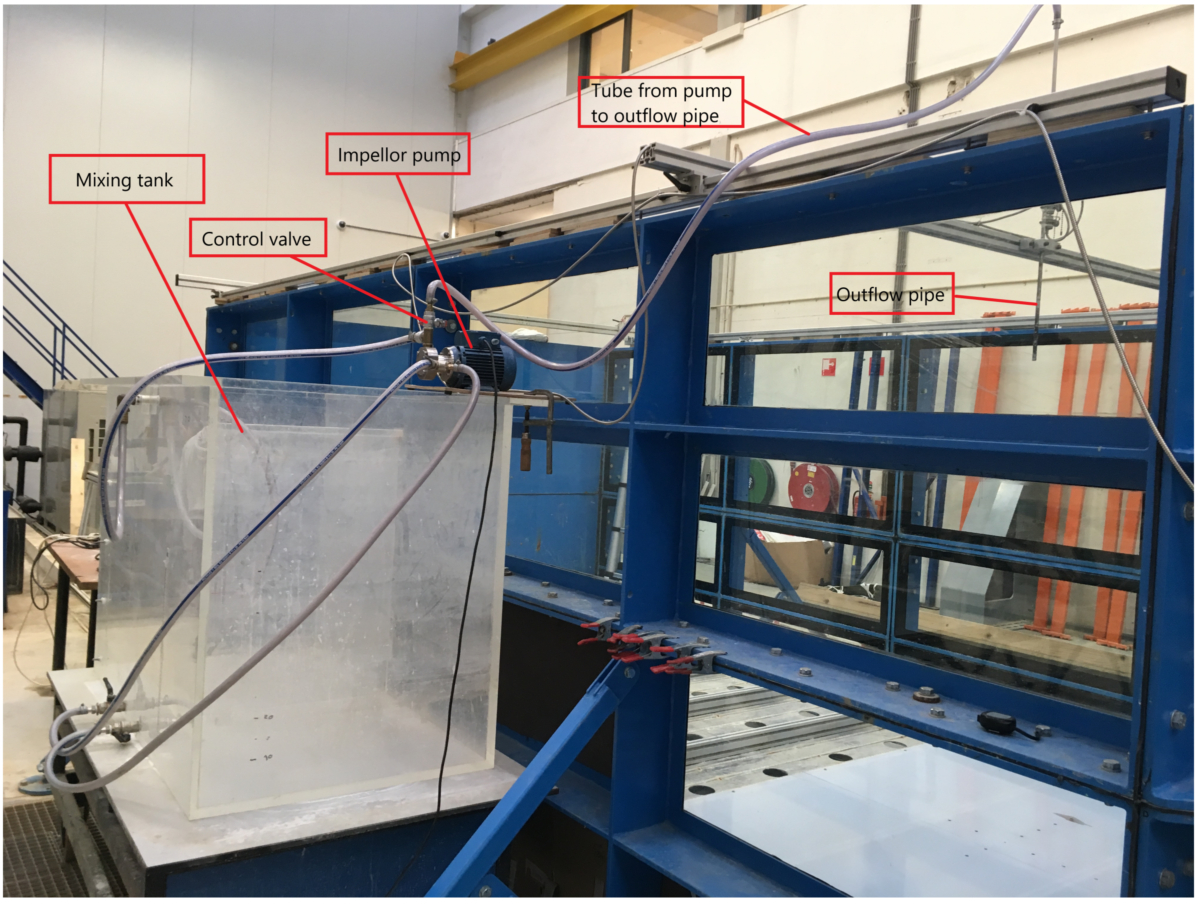


Figure 4.2: Mixing tank with impellor pump and valve to control velocity

**Nozzle shapes**

When the right mixture density is pumped to the reservoir, it goes through the 10mm diameter pipe (outside diameter 12mm). The aim of this experiment is to look at different overflow shapes and therefore three different shapes are tested, which are shown in figure 4.3. At the top of the pipe, a valve can regulate the flow to keep it constant. The round pipe is based as reference, because this is the common outflow shape of a overflow. Based on the sizing of the round pipe, two rectangular nozzle aspect ratios are chosen. Because the sizing of the round pipe is very small, the inner sizing is chosen, that the longer side is a multiple of the round pipe sizing (times 2 & times 3) with corresponding shorter size that keeps the area the same as is the case with the round pipe. It is interesting to see if the aspect ratio does influence the plume trajectory in the two directions of the nozzle (long- and short side).

| Shape | Inner sizing (mm) |
|---|---|
| ○ | 10 |
| ▭ | 20 x 3,9 |
| ▭ | 30 x 2,6 |

Figure 4.3: Inner sizing of different shapes needed to maintain same area

In order to test different shapes, the inner area is kept the same for all shapes to maintain the same velocity in all cases. From here, the best possible shape can be selected which can be translated to a diffusor. Because the valve is connected to the 12mm round pipe, the chosen option to change the outflow shapes is to slide a different attachment, which contains a part that slides over and a part that changes from a round shape to a rectangular shape, over the round pipe until a certain point. These attachments are 3D printed in-house of APT Offshore and are shown in figure 4.4b. The top parts are the different outflow shapes where the bottom parts are the slip-on parts which slide over the round pipe.

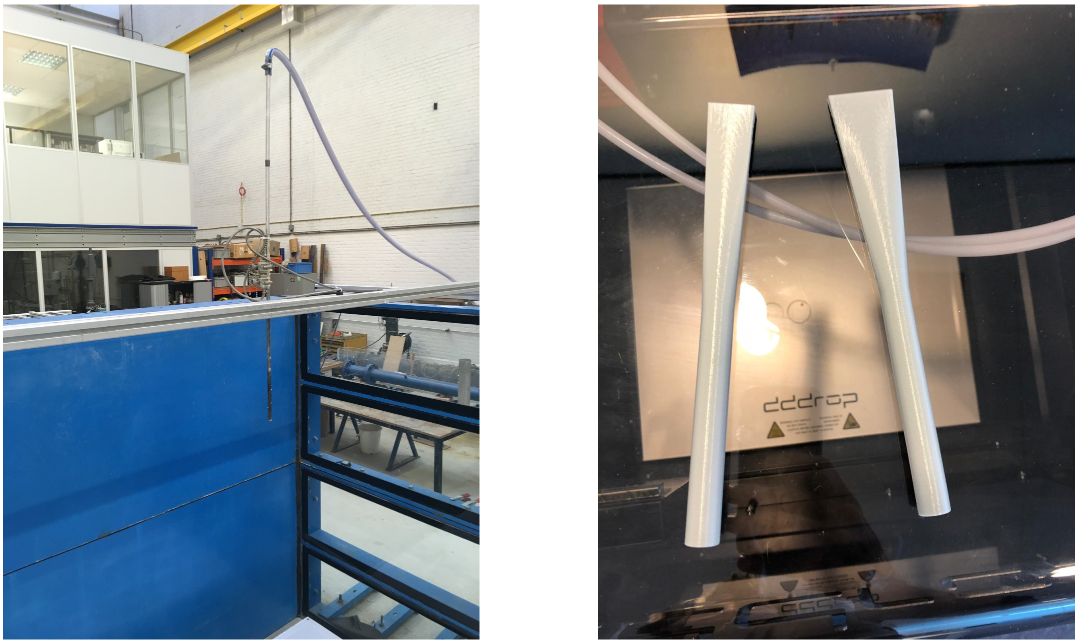


(a) Discharge pipe velocity sensor

(b) 3D printed nozzles

Figure 4.4: Pictures of discharge pipe and nozzles for different outflow shape

**Bottom frame**

When the water-sediment mixture flows into the reservoir trough the round pipe with different shape attachments, it flows into still water where it can spread and fall down on the plate on top of the bottom frame. In this plate, twelve holes are placed in a grid where tubes are connected to twelve valves which all can be opened apart from each other. With these valves, the water sediment mixture from a position in the grid can be sucked up to the drain point where the concentration can be measured. Between the plate and bottom frame are led strips placed for extra light during the tests. An overview of the bottom frame and plate can be seen in figure 4.5.

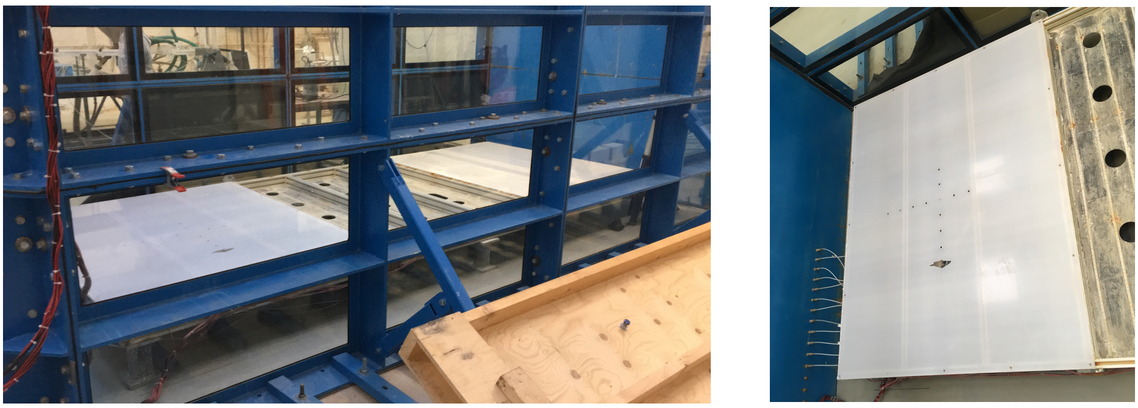

Figure 4.5: Frame with reservoir and plate with drain points

## 4.2. EXPERIMENTAL PARAMETERS

### 4.2.1. MATERIAL

As mentioned in chapter 2, due to the slower settling of finer sediment in the hopper with respect to coarser sediment, the overflow and therefore the exiting plume generally contains more mud and finer particles than the dredged material. Therefore a material is chosen which has a particle size distribution comparable to mud, which is quartz powder (figure 4.6). Quartz powder ($20 < d < 90$ micron) eases the production of homogeneous mixtures and does not cluster together to form flocs due to its neutral electrical charge. Before use, the quartz powder is sifted to ensure a size of $20 < d < 90$ micron. This is done to ensure no blockages of bigger particles inside the discharge pipe.

Figure 4.6: Quartz powder which is used during the experiments as material

### 4.2.2. DISCHARGE

In order to create a turbulent plume, a Reynolds value of > 2000 should be considered. Combining this with a discharge diameter of 10mm, the flow velocity of the mixture should be > 0.2m/s. In order to have some tolerance, it is chosen to have a outflow velocity of 0.35 m/s. It should be noted that the quartz powder particles will increase turbulence with the same Reynolds number comparing with normal tap water. Also the height in the tank is limited and therefore a lower outflow velocity means less interaction with the bottom plate. Interaction with the bottom plate will cause radial dispersion of the material which will influence the concentration measurements. This effect is not desirable in the experiment and so the height is maximized (1.585m) and outflow velocity is minimum to maintain a turbulent plume (0.35 m/s).

To achieve a stable outflow velocity, the discharge flowrate is regulated by the jet valve with the help of a flow meter (Katronic KATflow 200). KATflow (figure 4.7) is a portable instrument with two transducers fixed on the pipe wall. The key working principle of the instrument is that sound waves traveling with the flow will move faster than those traveling against it. Hence, the difference in the transit time of these signals is proportional to the flow velocity of the liquid and consequently the flow rate. Before the use, the instrument needs to be set and adjusted to the pipe and flow characteristics. For the instrument calibration, a known volume of the mixture is pumped over a fixed time and compared with the instrument output registered flow volume.

In case of changes in the flow rate, it is possible to quickly stabilize the flow to the required discharge velocity by turning the ball valve between the pump and the jet pipe.

Figure 4.7: Katronic KATflow 200 instrument used to set right flow discharge

### 4.2.3. MIXTURE DENSITY

In the mixing tank, tap water is mixed with quartz powder to create a certain mixture density. First of all the visibility is important for the video imaging. Previous tests done in the reservoir by Warringa [2017] and Byishimo [2018] used the same experimental setup. Both users compared three different mixtures (5,10,20 gram quartz powder / liter water) in their experiments. Visibility in all cases was not a problem. It should be noted that both experiments looked at impact on the seabed during deep mining operations. Because interaction with the bed leads to re-suspension of the material which is not desired in this experiment, the mixture density is chosen by looking at the re-suspension in the experiments of Warringa [2017]. Warringa [2017] compared three heights (0.25, 0.5, 1m). Because the height in this experiment is maximized (1.585m) an overview is shown in figure 4.8 containing all different mixture densities at height 1m, which was the maximum height in these both studies.

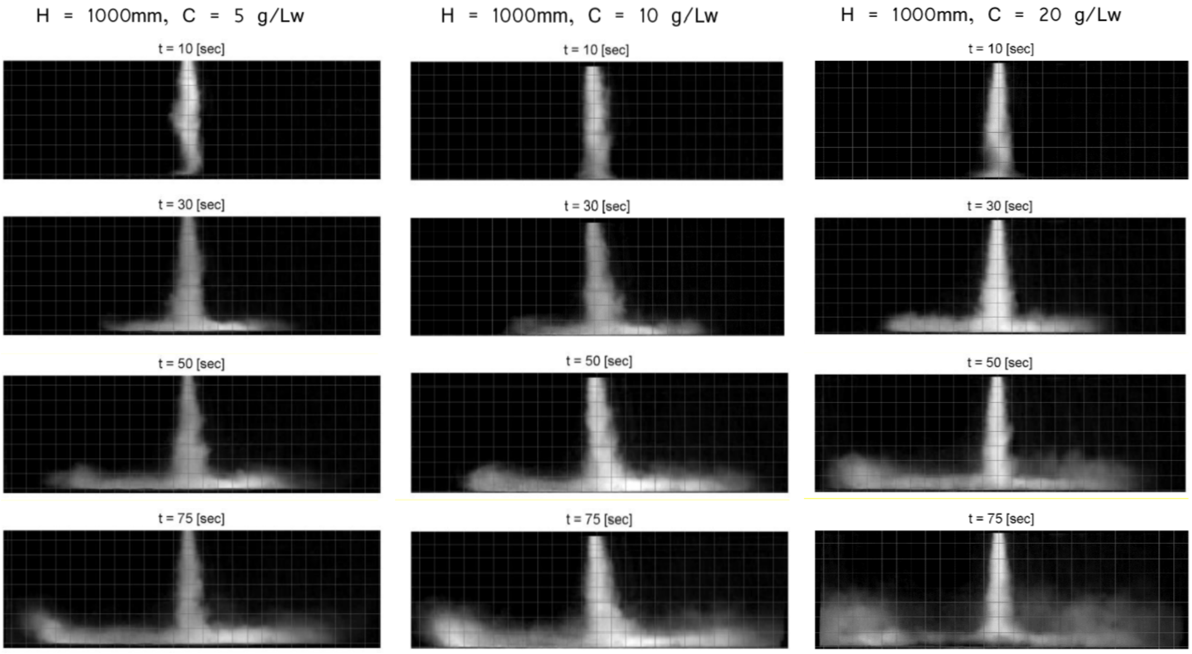


Figure 4.8: Comparison of re-suspension due to the bottom plate between three densities in experiment of Warringa [2017]

Looking at figure 4.8, it can be seen that the mixture with a suspended sediment concentration of 20 g/l has the most re-suspension due to interaction with the bottom plate. Between a SSC of 5 g/l and 10 g/l is not much of a difference in re-suspension height but does in re-suspension density. It should be noted that quartz powder has a polishing effect on the impellor pump which will damage it over time. Due to this, adding more quartz powder will assure more damage to the impellor pump. Due to this, a SSC of 5 g/l is chosen to use during the experiments. Also it should be noted that mixture density has influence on the plume angle and so the entrainment factor.

**Water Temperature**

To ensure no extra density differences due to difference in temperature between the water in the reservoir and in the mixing tank, the temperature of the reservoir is measured before each test. This temperature is set to be maintained inside the mixing tank within a range of 0.3 degrees below or above, because during experiment, the water in the mixing tank warms up with roughly an amount of 0.3 degrees. Adding warm water or use the submersible pump will increase the water temperature, cooling is done by adding cool tap water.

# 4.3. OBTAINMENT DATA

## 4.3.1. SUSPENDED CONCENTRATION

To measure the concentration of suspended particles in the plume, local SSC samples are taken by tubes installed in the table, which connects to drain points on the outside of the reservoir. The samples are measured with a high accuracy laboratory Turbidity meter AL450T-IR by which turbidity values were obtained as NTU value (Nephelometric Turbidity Unit). A picture of it is shown in figure 4.9.


Figure 4.9: Aqualytic Turbidity meter AL450TR-IR

The turbidity meter AL450T-IR is an optical portable turbidity meter designed with the requirements of ISO 7027, for the determination of turbidity for water quality with a measurement auto ranging over the range of 0.01 to 1100 NTU. The operating principles are based on positioning a transparent vial filled with the sample inside the instrument sample chamber. When the measuring button is pressed, an infrared LED (light emitting diode) with a wavelength of 860nm is emitted immediately. The emitted light is reflected by turbidity in the sample. The scattered light will be detected at an angle of 90° by a photo diode.
As an output, the sensor will show the NTU value on screen. In order to minimize errors, the vials and caps are cleaned inside and outside thoroughly after each test to avoid interference's. The outside of the vial must be clean, dry and wiped with a smooth cloth to remove fingerprints, dust or water drops. Details of the working principle of Turbidimeter AL450T-IR can be found on the manufacturer website. [Aqualytic, 2018]
After an experiment is started and a steady state is reached; one by one, the tube end valves are flushed for 30 seconds in order to clean them. Previous experiments of Byishimo [2018] showed that steady state differs for each measuring point, in other words, the distance of the measuring point with respect to the impingement point. Steady state increases with distance so the outer measurement points will occur a later steady state. In order to minimize wall effects and so resuspension of the plume, the outer measurement points are tapped first after they reach a steady state. It is fair to say that the time it takes of the plume to reach a measuring point and multiple that by two, a steady state is reached [Byishimo, 2018]. This time was measured by eye and was approximately 85 seconds. A time of 180 seconds is so fair to begin tapping the outer measurement points. When the tube is cleaned, samples are taken for each point on the measurement map shown in figure 4.10. The process of taking a a good sample are shown in an overview in figure 4.11.

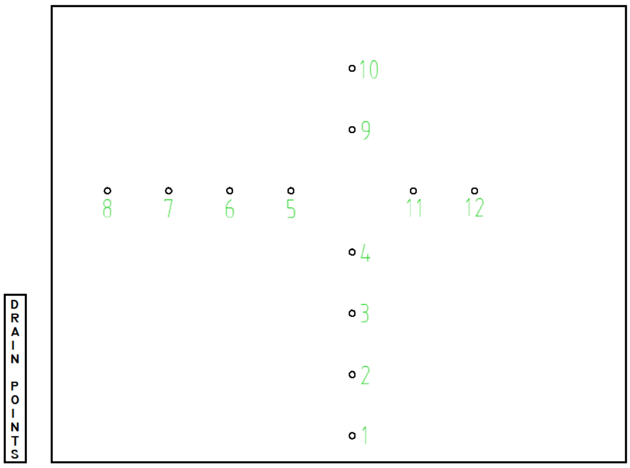


Figure 4.10: Measurement map plate (top view) with placing drain points. Also see figure 4.5

(a) drain sample (b) mix (c) pour in vial (d) vial mixing (e) NTU measuring

Figure 4.11: Steps for sample Turbidimeter (Pictures: Ivo Par)

Turbidity measurements are called local and near-bed SSC measurements because in the experiments of Byishimo [2018] it was noticed that not only the water at the table surface was drained by the tubes. Rather, when a valve was opened, turbid water from a column of about 20 mm above the plate was sucked into the tubes. For this reason, measurements taken by AL450T-R sensor only give the indications of a local averaged concentration rather than the near-bed SSC.

Before using the Turbidimeter AL450T-IR, the device is calibrated by testing eleven samples with intentional SSC in mg/l. The full overview can be found in Appendix D. An overview of the calibration with inserted trendline is visible in figure 4.12.

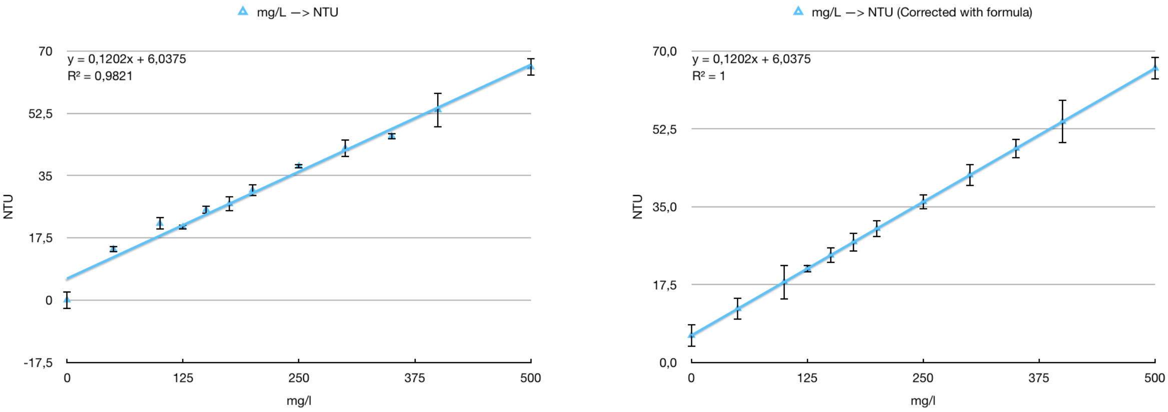


Figure 4.12: Calibration of Turbidimeter AL450T-IR with measured values, trendline and standard deviation (left) and corrected values by inserting formula with standard deviation (right)

The distances of the measurement points are determined by modelling the case with the round nozzle shape, as this is predicted in 3D from Lee & Chu [2003]. In figure 4.13 a case of the radial dispersion is shown with an outflow velocity ($u_0$) of 0.35 m/s, a height of 1.585m and a concentration of 5 g/l, like the case with the reservoir.

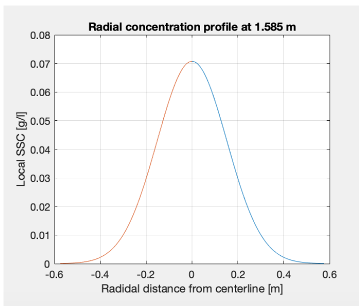


Figure 4.13: Radial dispersion in case of round shape with outflow velocity ($u_0 = 0.35 m/s$), height (1.585m)

Based on this model, the measurement points are decided to be in a radius from the outflow point straight down to the plate, of 100mm, 200mm, 300mm and 400mm. In table 4.1 it is shown which measurement point is on which radius. (See also figure 4.10)

| Radius | Measurement points |
|---|---|
| 100 mm | 4 5 9 11 |
| 200 mm | 3 9 10 12 |
| 300 mm | 2 7 |
| 400 mm | 1 8 |

Table 4.1: Overview of which measurement points lay on which radius from the middle point

### 4.3.2. VIDEO IMAGING

In order to get a good look whats happening during the experiments, next to the concentration measurements, two camera's are used. One camera is placed outside the tank and one GoPro camera is used inside the tank. The outside placed camera looks at the plume horizontally where the GoPro camera is placed near the outflow pipe and looks downward to visualize a top view of the plume. An overview of the placement of the camera's is shown in figure 4.14.

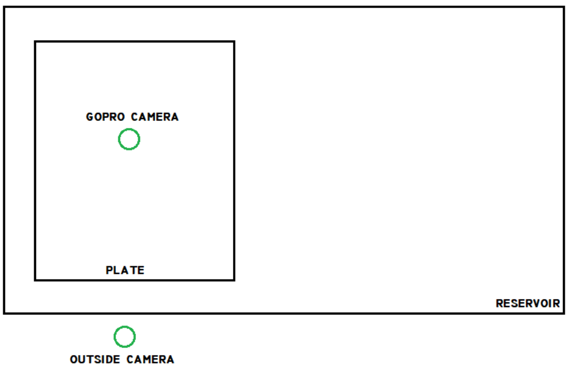


Figure 4.14: Top view of placement of camera's used during experiments

As shown above, a top view and horizontal view are made by the camera's to get a good overview of the plume. The top view is used to determine the radial dispersion of the plume and the camera outside shows a horizontal front view of the plume. Both camera's can say something about the differences between overflow shapes, but in other perspectives. Therefore both camera's are used to analyze the plume and to show differences between the plumes, regarding different overflow shapes. Both camera's are filming in full HD (1920x1080 pixels) and with the same framerate (25 fps).

The outside camera is used to determine the angle of the plume, in 2d perspective. This is done by analyzing the movie in matlab, where the movie is edited and analyzed. The matlab script creates multiple snapshots in time with a high contrast value so that the plume is highly visible and the edges of the plume can be distinguished from the ambient water. Based on the snapshots, like figure 4.15, an overview can be made of the plume in steady state and based on this snapshot a angle is measured.

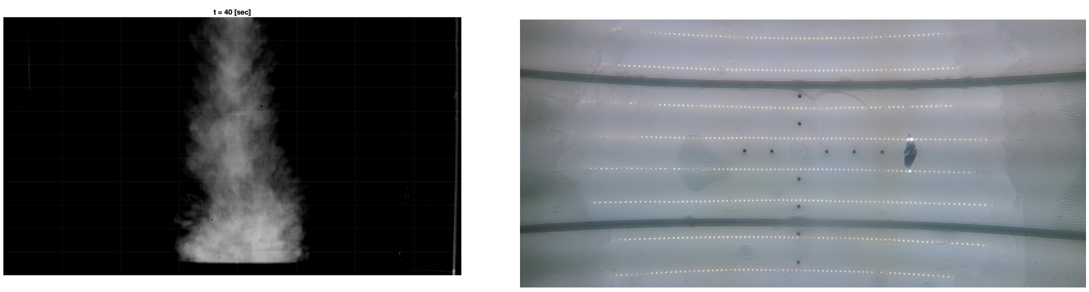


Figure 4.15: High contrast snapshot and image from topview

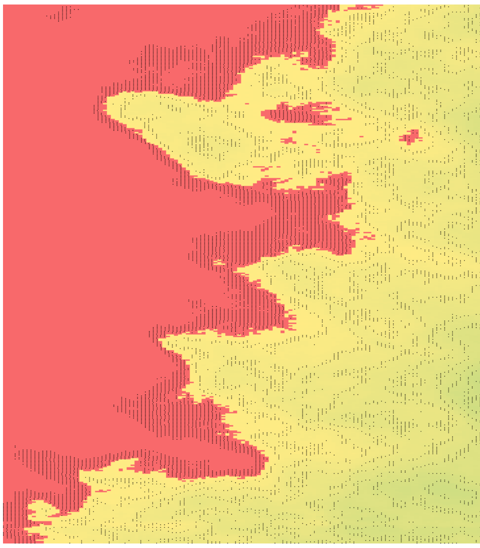

Figure 4.16: Colour scheme of plume, edited in Microsoft Excel

The matlab script shows a matrix of 1920x1080, which are the camera pixels, with different values in them where a value of 0 is black (as shown on the snapshot) and a value of >0 is a certain white value. With this matrix, the edges of the plume are shown in numbers based on the pixels of the camera. This matrix is imported to Microsoft Excel where a colour scheme (figure 4.16) is added to visualize the plume by colours. Based on this colour scheme, the edges of the plume are confirmed and a trendline is made of the left edge and the right edge of the plume. Based on looking at several test runs, a value of 14 in chosen as edge of the plume. It showed that values > 14 increased significantly and so it was determined as contour of the plume. With these trendlines, the mean angle is calculated of the plume.

## 4.4. EXPERIMENTAL PLAN

A total of 45 experiments are done during this thesis. Test numbers 1 to 5, are concentration and angle measurements both done in one experiment. Test number 6-20 are angle measurements only for the purpose of getting a reliable angle and so entrainment coefficient. In the case of the rectangular nozzle shapes test numbers 11-20, the nozzle was turned 90 degrees to see if the angle was different. The tests where done in a multiple of 5, until a error margin of the angle was reached of $\leq 1°$. In table 4.2 are all parameters shown during each experiment. The temperature, discharge of the pump and outflow velocity are filled in after each test.

| Test # | Overflow nozzle | Inner size | SSC | $\rho_0$ | Discharge pump | Outflow velocity | Discharge height | Temperature water |
|---|---|---|---|---|---|---|---|---|
| | $[round/rectangular]$ | $[mm]$ | $[g/L]$ | $[kg/m^3]$ | $[l/min]$ | $[m/s]$ | $[m]$ | [°] |
| Round_1 | Round | 10 | 5 | 998 | 1.641 | 0.348 | 1.585 | 15.3 |
| Round_2 | Round | 10 | 5 | 998 | 1.746 | 0.371 | 1.585 | 15.1 |
| Round_3 | Round | 10 | 5 | 998 | 1.621 | 0.344 | 1.585 | 15.8 |
| Round_4 | Round | 10 | 5 | 998 | 1.699 | 0.361 | 1.585 | 16.3 |
| Round_5 | Round | 10 | 5 | 998 | 1.644 | 0.349 | 1.585 | 16.5 |
| Rectangular_20x3.9_1 | Rectangular | 20x3.9 | 5 | 998 | 1.720 | 0.365 | 1.585 | 17.0 |
| Rectangular_20x3.9_2 | Rectangular | 20x3.9 | 5 | 998 | 1.661 | 0.352 | 1.585 | 17.2 |
| Rectangular_20x3.9_3 | Rectangular | 20x3.9 | 5 | 998 | 1.684 | 0.357 | 1.585 | 17.1 |
| Rectangular_20x3.9_4 | Rectangular | 20x3.9 | 5 | 998 | 1.583 | 0.336 | 1.585 | 17.2 |
| Rectangular_20x3.9_5 | Rectangular | 20x3.9 | 5 | 998 | 1.617 | 0.343 | 1.585 | 17.2 |
| Rectangular_20x3.9_6 | Rectangular | 20x3.9 | 5 | 998 | 1.593 | 0.338 | 1.585 | 17.0 |
| Rectangular_20x3.9_7 | Rectangular | 20x3.9 | 5 | 998 | 1.735 | 0.368 | 1.585 | 17.0 |
| Rectangular_20x3.9_8 | Rectangular | 20x3.9 | 5 | 998 | 1.601 | 0.340 | 1.585 | 17.1 |
| Rectangular_20x3.9_9 | Rectangular | 20x3.9 | 5 | 998 | 1.671 | 0.355 | 1.585 | 17.2 |
| Rectangular_20x3.9_10 | Rectangular | 20x3.9 | 5 | 998 | 1.678 | 0.356 | 1.585 | 17.2 |
| Rectangular_20x3.9_11 | Rectangular | 20x3.9 | 5 | 998 | 1.692 | 0.359 | 1.585 | 17.2 |
| Rectangular_20x3.9_12 | Rectangular | 20x3.9 | 5 | 998 | 1.662 | 0.353 | 1.585 | 17.2 |
| Rectangular_20x3.9_13 | Rectangular | 20x3.9 | 5 | 998 | 1.664 | 0.353 | 1.585 | 17.2 |
| Rectangular_20x3.9_14 | Rectangular | 20x3.9 | 5 | 998 | 1.623 | 0.344 | 1.585 | 17.2 |
| Rectangular_20x3.9_15 | Rectangular | 20x3.9 | 5 | 998 | 1.704 | 0.362 | 1.585 | 17.2 |
| Rectangular_20x3.9_16 | Rectangular | 20x3.9 | 5 | 998 | 1.575 | 0.334 | 1.585 | 17.2 |
| Rectangular_20x3.9_17 | Rectangular | 20x3.9 | 5 | 998 | 1.753 | 0.372 | 1.585 | 17.2 |
| Rectangular_20x3.9_18 | Rectangular | 20x3.9 | 5 | 998 | 1.596 | 0.339 | 1.585 | 17.2 |
| Rectangular_20x3.9_19 | Rectangular | 20x3.9 | 5 | 998 | 1.672 | 0.355 | 1.585 | 17.5 |
| Rectangular_20x3.9_20 | Rectangular | 20x3.9 | 5 | 998 | 1.673 | 0.355 | 1.585 | 17.5 |
| Rectangular_30x2.6_1 | Rectangular | 30x2.6 | 5 | 998 | 1.593 | 0.338 | 1.585 | 17.7 |
| Rectangular_30x2.6_2 | Rectangular | 30x2.6 | 5 | 998 | 1.653 | 0.351 | 1.585 | 17.9 |
| Rectangular_30x2.6_3 | Rectangular | 30x2.6 | 5 | 998 | 1.618 | 0.343 | 1.585 | 17.9 |
| Rectangular_30x2.6_4 | Rectangular | 30x2.6 | 5 | 998 | 1.596 | 0.339 | 1.585 | 17.9 |
| Rectangular_30x2.6_5 | Rectangular | 30x2.6 | 5 | 998 | 1.540 | 0.327 | 1.585 | 17.9 |
| Rectangular_30x2.6_6 | Rectangular | 30x2.6 | 5 | 998 | 1.655 | 0.351 | 1.585 | 17.9 |
| Rectangular_30x2.6_7 | Rectangular | 30x2.6 | 5 | 998 | 1.653 | 0.351 | 1.585 | 17.9 |
| Rectangular_30x2.6_8 | Rectangular | 30x2.6 | 5 | 998 | 1.644 | 0.349 | 1.585 | 17.9 |
| Rectangular_30x2.6_9 | Rectangular | 30x2.6 | 5 | 998 | 1.623 | 0.344 | 1.585 | 17.9 |
| Rectangular_30x2.6_10 | Rectangular | 30x2.6 | 5 | 998 | 1.654 | 0.351 | 1.585 | 17.9 |
| Rectangular_30x2.6_11 | Rectangular | 30x2.6 | 5 | 998 | 1.713 | 0.364 | 1.585 | 17.9 |
| Rectangular_30x2.6_12 | Rectangular | 30x2.6 | 5 | 998 | 1.649 | 0.350 | 1.585 | 17.9 |
| Rectangular_30x2.6_13 | Rectangular | 30x2.6 | 5 | 998 | 1.679 | 0.356 | 1.585 | 17.9 |
| Rectangular_30x2.6_14 | Rectangular | 30x2.6 | 5 | 998 | 1.709 | 0.363 | 1.585 | 17.9 |
| Rectangular_30x2.6_15 | Rectangular | 30x2.6 | 5 | 998 | 1.661 | 0.352 | 1.585 | 17.9 |
| Rectangular_30x2.6_16 | Rectangular | 30x2.6 | 5 | 998 | 1.688 | 0.358 | 1.585 | 17.9 |
| Rectangular_30x2.6_17 | Rectangular | 30x2.6 | 5 | 998 | 1.670 | 0.354 | 1.585 | 17.9 |
| Rectangular_30x2.6_18 | Rectangular | 30x2.6 | 5 | 998 | 1.603 | 0.340 | 1.585 | 17.9 |
| Rectangular_30x2.6_19 | Rectangular | 30x2.6 | 5 | 998 | 1.627 | 0.345 | 1.585 | 17.9 |
| Rectangular_30x2.6_20 | Rectangular | 30x2.6 | 5 | 998 | 1.658 | 0.352 | 1.585 | 17.9 |

Table 4.2: Used parameters for each experiment

# 5

# Experimental Results

*Before showing the results, it should be noted that all experiments are done by using the setup that was used for other purposes (deep sea mining) and so scaling was not possible. The height of the tank is maximized to reduce bottom effects and also the SSC is reduced to reduce impulse at the bottom. This should be noted before comparing with prototype scales.*

*In this chapter, the results from the experiment are analyzed. The analysis is divided into two parts, where one part consists of the concentration measurements to visualize the profile on the bottom plate, another to determine an entrainment coefficient by using the jet angle and to see differences in travel time with different nozzle shapes.*

*In section 7.1, the results of the concentration measurements are displayed. In this section, the radial dispersion of the plume and the concentration profile of the measurement points on the bottom plate are treated. Section 7.2 shows the results of angle measurements, which are divided in the determination of the entrainment angles and the determination of the entrainment coefficient using chapter 3. Further on, the travel time is calculated between the three different nozzle shapes, to see if momentum is different for the three cases.*

## 5.1. CONCENTRATION MEASUREMENTS

As said in chapter 4, the concentration of the plume is measured at the bottom of the reservoir on a plate with drain points which connects to taps outside the reservoir, where the concentration is measured with the AL450T-IR Turbidity Meter. For each nozzle shape, five concentration measurements are done. An overview of all measurements and an average are visible in appendix E.

### 5.1.1. RADIAL DISPERSION PLUME

As shown in figure 4.13, an expectation of the plume width was made based on the model of Lee & Chu [2003]. Using the topview camera images, the measurement points can be distinguished from the plume and plate. In figure 5.1 an topview image is shown between all three nozzle shapes.

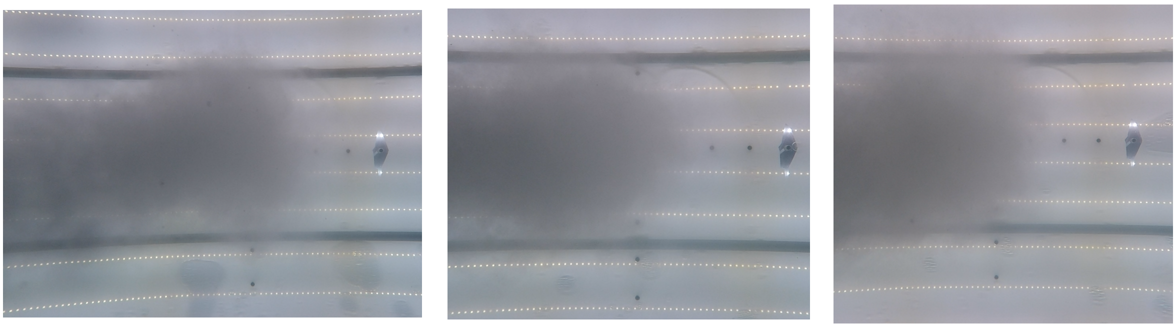

(a) Round (b) Rectangular 20x3.9 (c) Rectangular 30x2.6

Figure 5.1: Topview image for all nozzle shapes

As shown in figure 5.1, it is visible that in all cases, the radius of the plume has a maximum of roughly 200mm where all measurement points with a larger radius are clearly visible. Is it also visible that a rectangular nozzle shape decreases the radius of the plume to roughly less than 100mm (more measurement points are clearly visible). With this noted, the measurement points can be divided into two parts, where some points have a plume from above and a plume current due to the table, which spreads radially on the table. The measurement points which are not visible due to the plume are assumed to have a flow from above and a current sideways due to the table. The measurement points which are clearly visible from the topview image are assumed to have only a sideways current due to table.
Due to the current, some concentrations measured with the turbidity meter are not representative to give a conclusive result. Looking at figure 5.1, all measurement points with a radius > 200mm only have a concentration of a sideways current due to the bending effect of the plume, which is a effect of the tables boundary. In the case of the rectangular nozzles, the radial dispersion is even less. Therefore it is harder to give representative conclusions of measuring points with a radius of > 100mm which will increase change of fluctuation in the results of the concentration measurements.
Connecting this with the model from Lee & Chu [2003] (figure 4.13) which does not have the effect of a hard boundary, the measured concentrations should show a higher value due to the horizontal current added. Looking at a radius of 200mm between the predicted value (30 mg/l) (see figure 4.13) and the averaged measured concentration at this point in case of a round overflow shape, which is 40.64 mg/l (see appendix E), an added value is shown which can be translated to the horizontal current. Noting that a value > 30 mg/l should be found at this radius gives that the concentration measurements satisfies this.

Due to the radial dispersion measured and the connection with the measurement points, it is chosen to focus the concentration measurement on the points with a radius of 100mm, which are the points closest to the middle point.

### 5.1.2. CONCENTRATION PROFILE BOTTOM PLATE

Focusing on the measurement points with a radius of 100mm, which are points 4,5,9 and 11, the measured concentration in case of all nozzle shapes are found in table 5.1 (Round), table 5.2 (Rectangular 20x3.9) and table 5.3 (Rectangular 30x2.6). The numbers shown are the averaged results of each test, which are again averaged to get one value of all tests. The total averaged NTU is then converted to mg/l.

| Round | | | | | | | |
|---|---|---|---|---|---|---|---|
| **Measurement point** | **Test 1** | **Test 2** | **Test 3** | **Test 4** | **Test 5** | **Average NTU** | **Average mg/l** |
| 4 | 13.92 | 11.88 | 9.25 | 10.54 | 10.57 | 11.23 | 46.32 |
| 5 | 13.33 | 12.81 | 9.79 | 11.14 | 10.20 | 11.46 | 48.15 |
| 9 | 13.50 | 13.38 | 10.45 | 10.87 | 10.44 | 11.73 | 50.37 |
| 11 | 12.88 | 12.02 | 10.00 | 10.55 | 10.46 | 11.18 | 45.89 |

Table 5.1: Average results of all 5 tests done with round nozzle shape

| Rectangular 20x3.9 | | | | | | |
|---|---|---|---|---|---|---|
| **Measurement point** | **Test 1** | **Test 2** | **Test 3** | **Test 4** | **Average NTU** | **Average mg/l** |
| 4 | 12.54 | 12.07 | 13.13 | 13.20 | 12.74 | 58.61 |
| 5 | 12.57 | 12.04 | 11.63 | 13.44 | 12.42 | 56.04 |
| 9 | 13.87 | 12.66 | 11.96 | 13.78 | 13.06 | 61.29 |
| 11 | 14.37 | 12.62 | 10.81 | 13.46 | 12.81 | 59.25 |

Table 5.2: Average results of all 4 tests done with rectangular 20x3.9 nozzle shape

| Rectangular 30x2.6 | | | | | | | |
|---|---|---|---|---|---|---|---|
| **Measurement point** | **Test 1** | **Test 2** | **Test 3** | **Test 4** | **Test 5** | **Average NTU** | **Average mg/l** |
| 4 | 12.43 | 10.46 | 12.81 | 12.52 | 12.84 | 12.21 | 54.35 |
| 5 | 13.28 | 11.88 | 11.23 | 13.69 | 12.22 | 12.46 | 56.35 |
| 9 | 11.69 | 12.42 | 12.59 | 12.57 | 12.47 | 12.35 | 55.43 |
| 11 | 13.69 | 13.31 | 11.28 | 14.59 | 12.28 | 13.03 | 61.00 |

Table 5.3: Average results of all 5 tests done with rectangular 30x2.6 nozzle shape

It is clearly shown that a rectangular nozzle shape, with the same outflow area as a round nozzle shape, shows an increase of concentration at a radius of 100mm from the middle point. Taking an average value for all four measurement points (Round = 47.68 mg/l, Rectangular 20x3.9 = 58.80 mg/l, Rectangular 30x2.6 = 56.78 mg/l) shows an increase of roughly 22% in case of a rectangular nozzle shape. Looking at the aspect ratio of the rectangular nozzles, it is difficult to distinguish any difference based on only the concentration measurements. A visualisation is shown in figures 5.2 (side) and 5.3 (top) between the different nozzle shapes. A value of 70 mg/l is given to the middle point, which is in line with the model of Lee & Chu [2003]. For better detail, see appendix E5-22

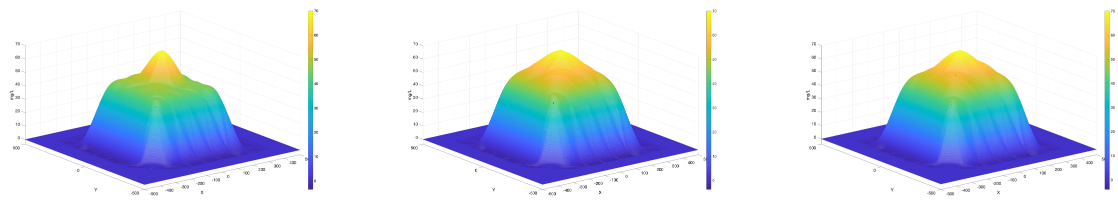

(a) Round (b) Rectangular 20x3.9 (c) Rectangular 30x2.6

Figure 5.2: Visualisation of concentration (mg/l) for all nozzle shapes (sideview, 400x400 grid)

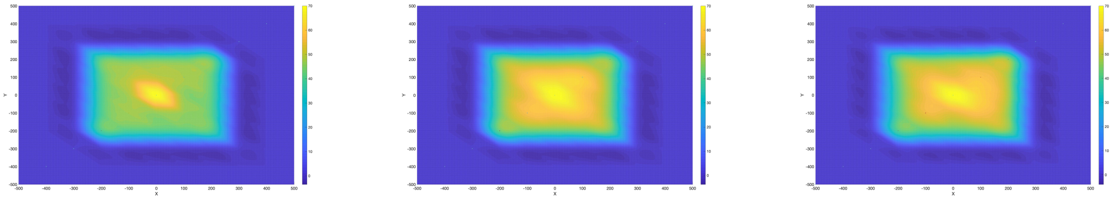

(a) Round (b) Rectangular 20x3.9 (c) Rectangular 30x2.6

Figure 5.3: Visualisation of concentration (mg/l) for all nozzle shapes (topview, 400x400 grid)

The images in case of a round nozzle (figures 5.2a and 5.3a) show a lower concentration comparing to the rectangular nozzles. It should be noted that the middle value (70 mg/l) is a taken value and is not measured, therefore the result of the round nozzle shows a large peak in the middle point. Looking at the measurement points at 200mm radius (3, 6, 10, 12), which are also taken into account in the visualisation, remains almost the same in all three cases. The only noticeable difference is the increase of concentration for a radius < 200mm. Which implies with a more dense area of impact compared to the wider distribution in case of the round outflow shape. It is assumed that the entrainment is better with a rectangular nozzle and so the plume has a smaller angle based on the concentration measurements.

## 5.2. ANGLE MEASUREMENTS

Showing an increase of concentration in case of a rectangular nozzle shape should connect to less entrainment with the surrounding ambient water. A steeper angle of the plume should be measured in this case, which is investigated in this section. The determination of the entrainment angles based on a contour trendlines is shown in appendix F.

### 5.2.1. ENTRAINMENT ANGLES

In a total of 45 experiments, the entrainment angle is measured. It was not possible to capture the total height in the camera frame. Therefore the angle was measured from the moment the plume entered the camera frame until it reached the bottom plate. By following the contour the plume and creating two trendlines (left- and right contour plume), the angle is calculated between the two trendlines. An example is shown in figure 5.4. All snapshots of the plumes, at the point where the angles are measured, are shown in appendix F. An overview of all calculated angles is shown in table 5.4.

| R1_t100 | | | |
|---|---|---|---|
| Left | | Right | |
| Row | Column | Row | Column |
| 23 | 877 | 43 | 1101 |
| 96 | 854 | 84 | 1136 |
| 137 | 824 | 146 | 1151 |
| 187 | 823 | 230 | 1150 |
| 228 | 834 | 314 | 1173 |
| 372 | 828 | 377 | 1213 |
| 490 | 795 | 466 | 1215 |
| 524 | 769 | 573 | 1280 |
| 637 | 750 | 684 | 1281 |
| 773 | 743 | 777 | 1306 |
| 828 | 739 | 843 | 1314 |

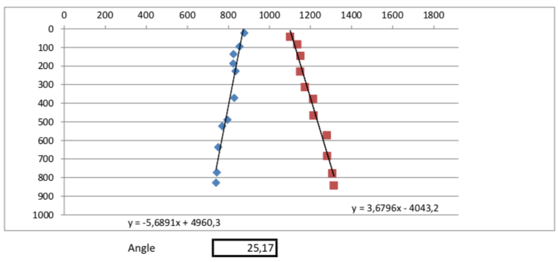


Figure 5.4: Determination of contour trendlines for test Round 1

| Round | |
|---|---|
| **Test #** | **Angle** (°) |
| 1 | 25.17 |
| 2 | 29.56 |
| 3 | 26.27 |
| 4 | 25.81 |
| 5 | 24.97 |

| Rectangular 20x3.9mm | |
|---|---|
| **Test #** | **Angle** (°) |
| 1 | 18.77 |
| 2 | 24.60 |
| 3 | 24.10 |
| 4 | 20.08 |
| 5 | 20.86 |
| 6 | 22.51 |
| 7 | 21.93 |
| 8 | 23.73 |
| 9 | 20.75 |
| 10 | 22.87 |
| 11 | 27.07 |
| 12 | 22.08 |
| 13 | 20.55 |
| 14 | 25.23 |
| 15 | 27.19 |
| 16 | 25.16 |
| 17 | 21.09 |
| 18 | 28.14 |
| 19 | 21.77 |
| 20 | 23.39 |

| Rectangular 30x2.6mm | |
|---|---|
| **Test #** | **Angle** (°) |
| 1 | 22.47 |
| 2 | 23.26 |
| 3 | 17.77 |
| 4 | 22.70 |
| 5 | 20.14 |
| 6 | 23.13 |
| 7 | 19.44 |
| 8 | 23.76 |
| 9 | 20.85 |
| 10 | 20.38 |
| 11 | 19.48 |
| 12 | 23.80 |
| 13 | 22.96 |
| 14 | 18.89 |
| 15 | 24.08 |
| 16 | 19.47 |
| 17 | 19.33 |
| 18 | 21.56 |
| 19 | 23.24 |
| 20 | 20.58 |

Table 5.4: Calculated angles for each nozzle. Note that for the both rectangular nozzles experiments 11-20 the nozzle is turned 90 degrees

Comparing the angles, lower angles are found in case of a rectangular nozzle. Looking at table 5.5, which shows the average calculated angle with error (which should be $< 1°$), it shows that the angle is indeed lower in case of the rectangular nozzles. The average angle is reduced in a range of 8.3% - 19% based on the measured angles.

| **Nozzle shape** | **Average angle** (°) | **Error** (°) |
|---|---|---|
| Round | 26.36 | 0.75 |
| Rectangular 20x3.9 - 3.9 | 22.02 | 0.58 |
| Rectangular 20x3.9 - 20 | 24.17 | 0.83 |
| Rectangular 30x2.6 - 2.6 | 21.39 | 0.59 |
| Rectangular 30x2.6 - 30 | 21.34 | 0.61 |

Table 5.5: Averaged angles and error for each nozzle shape. The last number (- xx) for the rectangular nozzles shows the side which faced the camera

In order to test if the aspect ratio has effect on the entrainment angle, the nozzle in case of rectangular shape is turned 90 degrees (experiments 11-20). Based on the experiments, if shows that when the aspect ratio increases of the rectangular nozzle, the entrainment angles decrease in both orientations and even become nearly constant in the case of the 30x2.6mm nozzle. It should be noted that the rectangular shapes show more fluctuation between measurements, but definitely decrease the averaged entrainment angle of the plume. The finding of the lower entrainment angle connects with the denser concentration near the middle point which is found in the concentration measurements.

### 5.2.2. ENTRAINMENT COEFFICIENT

In order to determine the entrainment coefficient, the literature from chapter 3 is used. Here we combine the knowledge of the reference frame from figure 3.3 where there is a difference between the velocity width and concentration width, which is related to the concentration to velocity ratio ($\lambda_r$). In section 3.3 the entrainment coefficients ($\alpha_G$) and concentration to velocity ratio are shown in case of round jets and plumes, and plane jets ans plumes. Knowing that is assumed that the plume spreads linearly, the velocity width (b) was denoted as $b = \beta_G * z$. Relating this spreading rate back to the measured angles, which measures the plume concentration width, we can find the velocity width with formula 5.1 for all 4 cases. Table 5.6 shows the calculated b and $\beta$ in all cases. The measured half angle is denoted as $\gamma$, where z is the height.

$$tan(\gamma) = \frac{\lambda_r * b}{z} \tag{5.1}$$

| | Round | Rectangular 20x3.9 - 3.9 | Rectangular 20x3.9 - 20 | Rectangular 30x2.6 - 2.6 | Rectangular 30x2.6 - 30 |
|---|---|---|---|---|---|
| **Angle ($\gamma$)** | 13.18 | 11.01 | 12.085 | 10.695 | 10.67 |
| **Concentration width ($\lambda_r b$)** | 0.3712 | 0.3084 | 0.3394 | 0.2993 | 0.2986 |
| **Velocity width ($b$)** | 0.3119 | 0.2284 | 0.2514 | 0.2217 | 0.2212 |
| **Spreading rate ($\beta_G$)** | 0.1968 | 0.1441 | 0.1586 | 0.1399 | 0.1396 |

Table 5.6: Calculated concentration width, velocity width and spreading rated bases on measured angles

Now that the spreading rate is known, the entrainment coefficient can be determined using the relations found in chapter 3, which is summarized in section 3.3. Table 5.7 show the calculated entrainment coefficients in case of a jet and a plume, for all angles measured during the experiment. Looking at the concentration width calculated and the snapshots from above (figure 5.1), they do not coincide. However, the angles where measured at T=100s as where the plumes reached the bottom at T=40S. It was not good possible to measure the angles at this moment, due to the great turbulence of the plume. Therefore, when doing experiments with the same nozzle shape, the angle was totally different. Due to this, it was chosen to measure the angles at a moment where the plume was reasonably stable. This has a drawback due to the effect of table, which cause radial dispersion of the plume. Therefore, the assumption is that the plume width in reality is smaller than the concentration width calculated from the angle experiments, which is also indicated by the topview camera snapshots.

| | Round | Rectangular 20x3.9 - 3.9 | Rectangular 20x3.9 - 20 | Rectangular 30x2.6 - 2.6 | Rectangular 30x2.6 - 30 |
|---|---|---|---|---|---|
| $\boldsymbol{\alpha_G - jet}$ | 0.0984 | 0.0639 | 0.0703 | 0.0620 | 0.0618 |
| $\boldsymbol{\alpha_G - plume}$ | 0.1640 | 0.1277 | 0.1406 | 0.1240 | 0.1237 |

Table 5.7: Calculated entrainment coefficients ($\alpha_G$) by using table 3.1

As determined before, by finding a smaller angle in case of a rectangular nozzle, the entrainment in this case is less compared to a round nozzle. Even that the methods that determine the entrainment coefficient are different in case of round jets and plumes and plane jets and plumes, the rectangular (plane) nozzles show a lower entrainment coefficient, which relates to less entrainment with the ambient water. In case of a jet, the entrainment coefficient is reduced with a range of 28.6% - 37.2%. In case of a plume, the entrainment coefficient is reduced with a range of 14.3% - 24.6%. Connecting this to the reduction found for the averaged angles, it is shown that a relative small angle reduction (8.3%) decreases the entrainment coefficient, both for jets and plumes, with >14%. It is also visible that with a larger decrease in angle, the entrainment coefficient also decreases further and follows the trend of the decreasing line of the angle. Based on the entrainment coefficient, is it visible that a reduction of the angle of the plume has a better effect on a jet than a plume. An overview of the decrease of all angles and entrainment coefficients is shown in figure 5.5.

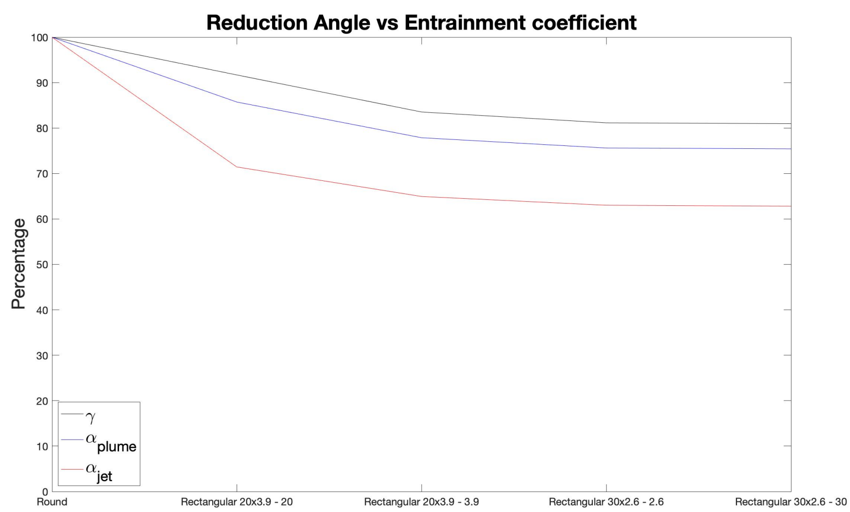


Figure 5.5: Overview reduction of measured angle ($\gamma$) and entrainment coefficient for jet ($\alpha_{jet}$) and plume ($\alpha_{plume}$)

Looking at the aspect ratio, shown in figure 5.6, where the two different orientations are compared with each other, a difference is visible.

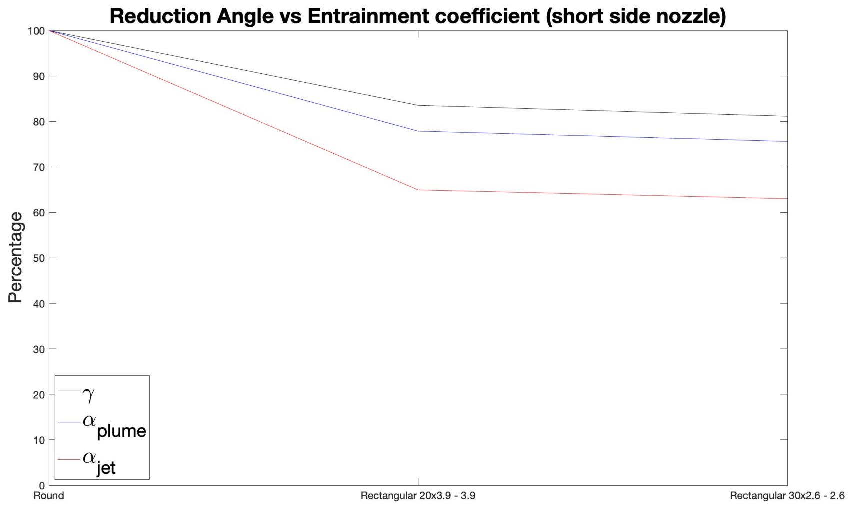


(a) Short side nozzle

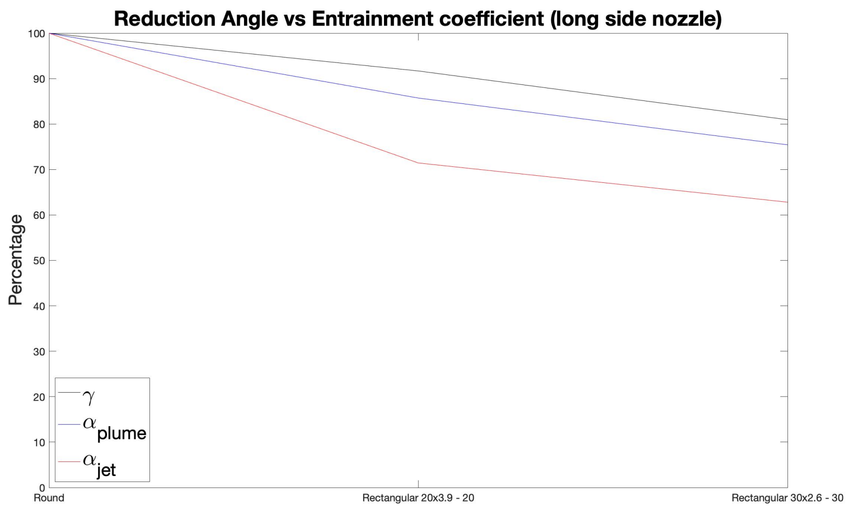


(b) Long side nozzle

Figure 5.6: Difference in reduction between the two possible orientations of the rectangular nozzle

Based on the two aspect ratios measured, both aspect ratios converge nearly to the same reduction value however, following different paths. Looking at the the lower graph, which describes the reduction of the angles measured with the long side of the nozzle facing the camera, the angle and entrainment coefficient of the plume decreases almost line linearly. The entrainment coefficient in the case of a jet, shows a better reduction when changing from round to a rectangular nozzle instead of changing the aspect ratio of the rectangular nozzle. Still a reduction is found, following a less steep line. Same is seen in the upper graph, which describes the reduction of the angles measured with the short side of the nozzle facing the camera.
Comparing the two orientations of the nozzle, it can be seen that in this case, using a higher aspect ratio decreases the entrainment coefficient with nearly the same amount and so interaction with a crossflow has the same influence on both orientations of the nozzle. If the aspect ratio decreases, for example the rectangular 20x3.9mm nozzle, the angle is different for the two orientations and so when in interaction with a crossflow, the orientation of the nozzle has influence on the plume path. The effect of the entrainment coefficient combined with crossflow is further collaborated in chapter 6.

### 5.2.3. TRAVEL TIME

Another way to check a less entrainment due to the change of nozzle shape, the time is measured from the entrance in the camera frame until the plume reached the edge of the bottom frame, which is denoted by the red line in figure 5.7. From each movie that was taken with the camera, both the time when the plume entered the camera frame ($T_{start}$) and reached the red line ($T_{plate}$) where measured. All data is shown in table 5.8.

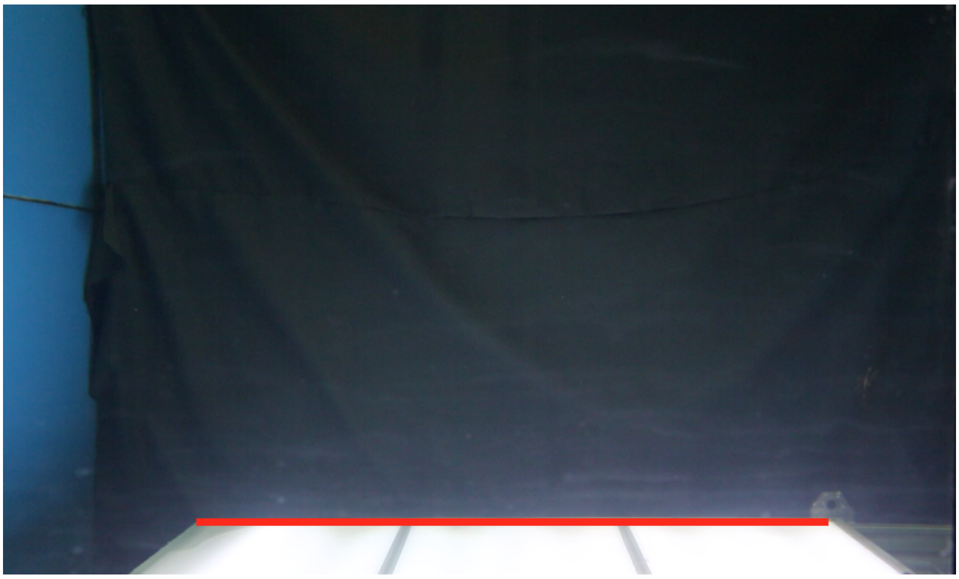

Figure 5.7: Frame used to determine travel time. Red line displays the edge of the table

| Round | | | |
|---|---|---|---|
| Test # | $T_{start}$ | $T_{plate}$ | $\Delta$ |
| 1 | 174 | 208 | 34 |
| 2 | 182 | 205 | 23 |
| 3 | 84 | 110 | 26 |
| 4 | 90 | 121 | 31 |
| 5 | 122 | 154 | 32 |

| Rectangular 20x3.9mm | | | |
|---|---|---|---|
| Test # | $T_{start}$ | $T_{plate}$ | $\Delta$ |
| 1 | 88 | 113 | 25 |
| 2 | 70 | 101 | 31 |
| 3 | 228 | 143 | 25 |
| 4 | 440 | 466 | 26 |
| 5 | 151 | 176 | 25 |
| 6 | 32 | 58 | 26 |
| 7 | 207 | 231 | 24 |
| 8 | 139 | 165 | 26 |
| 9 | 130 | 160 | 30 |
| 10 | 150 | 174 | 24 |
| 11 | 93 | 120 | 27 |
| 12 | 33 | 58 | 25 |
| 13 | 155 | 178 | 23 |
| 14 | 50 | 77 | 27 |
| 15 | 36 | 65 | 29 |
| 16 | 37 | 60 | 23 |
| 17 | 44 | 77 | 33 |
| 18 | 48 | 73 | 25 |
| 19 | 142 | 169 | 27 |
| 20 | 43 | 71 | 28 |

| Rectangular 30x2.6mm | | | |
|---|---|---|---|
| Test # | $T_{start}$ | $T_{plate}$ | $\Delta$ |
| 1 | 289 | 314 | 25 |
| 2 | 60 | 90 | 30 |
| 3 | 75 | 104 | 29 |
| 4 | 75 | 98 | 23 |
| 5 | 145 | 174 | 29 |
| 6 | 120 | 151 | 31 |
| 7 | 77 | 105 | 28 |
| 8 | 107 | 132 | 25 |
| 9 | 151 | 175 | 24 |
| 10 | 49 | 78 | 29 |
| 11 | 109 | 134 | 25 |
| 12 | 82 | 106 | 24 |
| 13 | 90 | 119 | 29 |
| 14 | 95 | 119 | 24 |
| 15 | 123 | 148 | 25 |
| 16 | 74 | 98 | 24 |
| 17 | 119 | 146 | 27 |
| 18 | 109 | 134 | 25 |
| 19 | 119 | 143 | 24 |
| 20 | 100 | 127 | 27 |

Table 5.8: Measured start times and time the plume reaches the back end of the plate for each nozzle shape

Looking at table 5.8, it can be seen that the fluctuation between $T_{start}$ and $T_{plate}$, denoted as $\Delta$, contains of seconds with a larger fluctuation in case of the round nozzle because of the lesser tests. The turbulent entrainment shows a bad predictability when comparing the same parameters. In case of the round nozzle, a maximum difference of $\Delta = 11s$ is found between two tests. In the case of both rectangular nozzles, a maximum difference of $\Delta = 10s$ and $\Delta = 7s$ is found. This shows a great unpredictable influence of the turbulent entrainment.

The effect of starting the test could also have influence of the time measured. During tests, the inflow velocity had to be regulated by using two valves manually. At the start of each test, the valves where regulated slowly until a velocity of 0.35 m/s was reached. However, it is possible that during some experiments, the regulation of the valves happened quicker or slower than other tests, which should be taken into consideration. However, looking at the averaged $\Delta$ values of each nozzle, a shorter time is measured for both rectangular nozzles to reach the edge of the bottom plate, comparing with the round nozzle.

| | **Round** | **Rectangular 20x3.9mm** | **Rectangular 30x2.6mm** |
|---|---|---|---|
| **Average $\Delta$** | 29.2 | 26.45 | 26.35 |

Table 5.9: Average measured $\Delta$ for the three nozzle shapes

This finding coincides with the finding of the steeper angle, which relates to a less entrainment of the plume in the ambient water. Looking at the aspect ratio, the time decreases, however with a negligible margin. Because of the fluctuations of $\Delta$ due to the unpredictable turbulence of the plume, this difference can be neglected. However, the difference between the round nozzle and rectangular nozzle is noticeable and coincides with earlier findings.

## 5.3. SUMMARY

Based on the results of the experiments, it can be seen that a rectangular nozzle does improve the entrainment of the plume in surrounding water. In the concentration tests, the plume measured at the bottom with the measurement points showed a more dense plume in the center of the plume. Connecting this with a steeper angle found in case of rectangular nozzle confirms that the plume showed less entrainment compared to the round case.

When looking at the aspect ratio of the rectangular nozzles, is showed that when increasing the aspect ratio of the nozzle the entrainment is even better. However, the step from round to rectangular is bigger than from increasing the aspect ratio of the rectangular nozzle shape. Therefore further investigation can be done in finding the best aspect ratio of the rectangular nozzle shape. It also should be noted that these experiments are done in still ambient water without any form of crossflow. Therefore a next step is to experiment the outflow with rectangular nozzle shapes with crossflow. However, an indication of the plume trajectory with crossflow can be made in the JETLAG model in chapter 8.

# 6

# Plume Trajectory With Crossflow

*Now the plume in still ambient water is investigated, it is also important to see what happens if a crossflow is added. In this chapter, an indication of the plume trajectory with crossflow is given which is done by the JET-LAG model from Lee & Chu [2003]. This model is tweaked by using the different entrainment coefficients for the different nozzles.*

*Firstly, the model is compared to the finding of the experimental research, so without crossflow. After this, crossflow is added with different values, to see what kind of influence the magnitude of crossflow velocity has on the plume trajectory. Next to that, practical values are scaled back to be implemented in the model.*

## 6.1. JETLAG MODEL

The JETLAG model is introduced by Lee & Cheung [1990] and explained in Lee & Chu [2003]. The model describes initial mixing of buoyant wastewater discharged in a current in case of, for example, environmental impact assessments.

### 6.1.1. OVERVIEW OF MODEL

The JETLAG model predicts the mixing of buoyant jets with two-dimensional trajectories and is developed after extensive testing against laboratory data. The model does not solve the Eulerian governing differential equations of fluid motion and mass transport but simulates the key physical processes expressed by the governing equations. The unknown jet trajectory is viewed as a sequential series of plume-elements (figure 6.1) which increase in mass as a result of shear induced entrainment (due to the jet discharge) and vortex entrainment (due to the crossflow).

The model tracks the evolution of the average properties of a plume element at each step by conservation of horizontal- and vertical momentum, conservation of mass accounting for the entrainment and conservation of tracer mass. The vortex entrainment is determined by a Projected Area Entrainment (PAE) hypothesis originally proposed by Frick [1984].

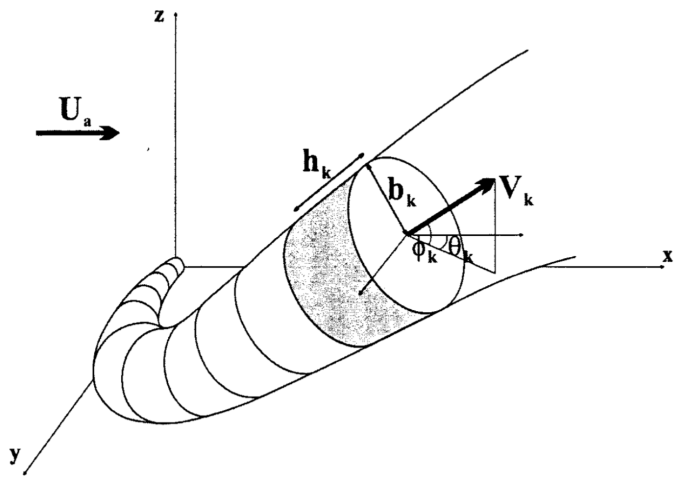


Figure 6.1: Schematic diagram of jet trajectory traced out by Lagrangian plume elements

**Model formulation**

At each time step, the following parameters are calculated: (see for detailed version Lee & Chu [2003])

- Mass (M)
- Concentration (c)
- Salinity (S)
- Density ($\rho$)
- Horizontal momentum (u,v)
- Vertical momentum (w)
- Radius / Thickness plume (b,h)
- Jet orientation ($\theta, \phi$)
- Location (x,y,z,s)

Next to that, there are initial conditions consisting of the outflow velocities (u,v,w), half width of the plume at outflow, thickness of the plume at outflow (defined as proportional tot the magnitude of the outflow velocity), salinity, temperature, density and concentration at outflow. Using the averaged properties of the jet cross section, no distinction can be made between the zone of flow establishment (ZFE) and zone of established flow (ZEF). Pressure drag is neglected in the model.
The increase in mass of the plume element at each time step ($\Delta M$) is computed as a function of two components: the shear entrainment due to relative velocity between the plume element and the ambient velocity in the direction to the jet axis ($\Delta M_s$) and the vortex entrainment due to the ambient crossflow ($\Delta M_f$).

**Shear entrainment**

The JETLAG model uses the following expression for the shear entrainment ($\Delta M_s = E_s$), which is calculated at each time step, as shown in figure 6.1.

$$E_s = 2\pi\alpha_s b_k h_k \Delta U \Delta t \tag{6.1}$$

Where $V_k$ is the jet velocity and $\Delta U = |V_k - U_a cos\phi_k cos\theta_k|$ is the relative jet velocity in the direction of the jet axis. Further $b_k, h_k$ are the radius and thickness of the plume element (figure 6.1). Here we see the entrainment coefficient ($\alpha_s$) again, which is implemented to calculate the shear entrainment. In this thesis, the entrainment coefficient is calculated by doing angle measurements in still ambient water. This entrainment coefficient is therefore a constant, where it could be argued that the entrainment coefficient is not constant in case with a crossflow. However, in this case, the constant entrainment coefficient is used which is obtained from the experiments.

**Vortex entrainment**

The vortex entrainment due to the crossflow is modelled using the PAE hypothesis (figure 6.2). The total vortex entrainment has three contributing terms to the projected area: the entrainment due to the projected plume area normal to the crossflow ($E_p$), a correction term due to the increase in plume width ($E_w$) and a correction term due to the plume curvature ($E_c$). An estimate of $\Delta M_f$ is shown in equation 6.2.

$$\begin{aligned} \Delta M_f &= E_p + E_w + E_c \\ &= \rho_a U_a (A_p + A_w + A_c)\Delta t \end{aligned} \tag{6.2}$$

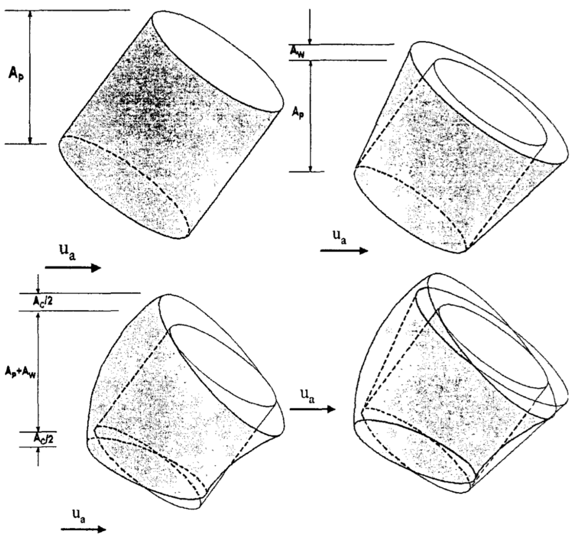


Figure 6.2: Illustrations of the three contributions of the Projected Area Entrainment (PAE): projected area ($A_p$), increase in area due to plume growth ($A_w$) and correction in area due to plume curvature ($A_c$). A sum of all is shown in the right low corner

**Total entrainment**

The total entrainment can be obtained from a maximum hypothesis ($\Delta M = max(\Delta M_s, \Delta M_f)$ or an additive hypothesis ($\Delta M = \Delta M_s + \Delta M_f$). Comparison with laboratory data shows better results when selecting the maximum hypothesis. However, using the maximum hypothesis can give unreasonable predictions for a weak ambient crossflow.

## 6.2. RESULTS BY IMPLEMENTING EXPERIMENT VALUES

By using the entrainment coefficient, which can be seen as a shear entrainment only ($\alpha_s$), the path of the plume can be modelled. Firstly, the maximum hypothesis is checked in our case, with zero crossflow, to see if the model connects with the angle measurements. In figure 6.3, the plume path is shown for both the round case ($\alpha_s = 0.164$), as the best rectangular case ($\alpha_s = 0.1237$). The height is set to equal the height of the experiment setup to find the modelled plume width. All graphs are based on the following input parameters:

- d = 0.01m
- $W_0$ = 0.35 m/s
- c = 5 g/L
- $\rho_s = 2650\ kg/m^3$
- $\rho_{amb} = 1000\ kg/m^3$
- $\Delta T = 0\ ^\circ$
- $\Delta S$ = 0 PSU

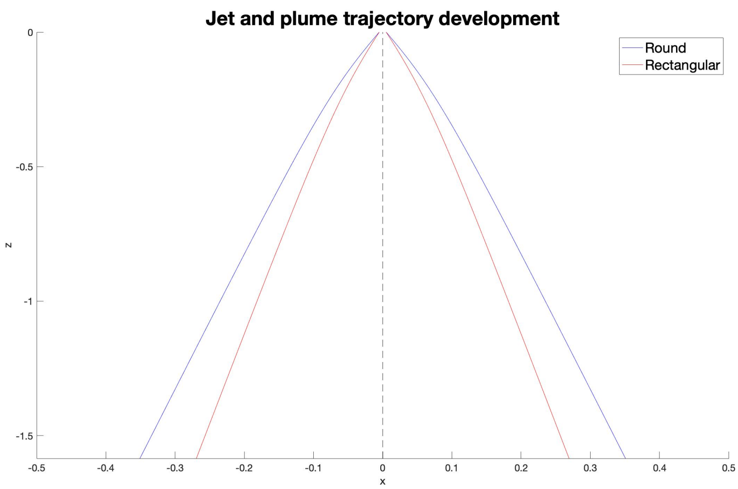


Figure 6.3: Modelled plume width by using experiment height and entrainment coefficient

Following the graph, in case of the round nozzle, the plume width is 0.3498m and in case of the rectangular nozzle, the modelled plume width is 0.2684m. This is roughly 0.02-0.03m smaller than the concentration width found with the angles from the experiments. However, as said before, the plume in reality will have a smaller angle than measured in the experiments. Therefore it is fair to say that the model is sufficient enough to give an indication of the plume trajectory when interacting with crossflow.

**Model with crossflow**

To give an indication of the plume trajectory with crossflow, the plumes are modelled with several crossflow velocities, to see if a higher crossflow velocity decreases the effect of the nozzle shape. The plume trajectories are compared with each other with a crossflow velocity of 0.02, 0.035 and 0.05 m/s. The reservoir used for the experiments is set as reference frame for the plume trajectory. The three modelled plume trajectories are shown in figure 6.4.

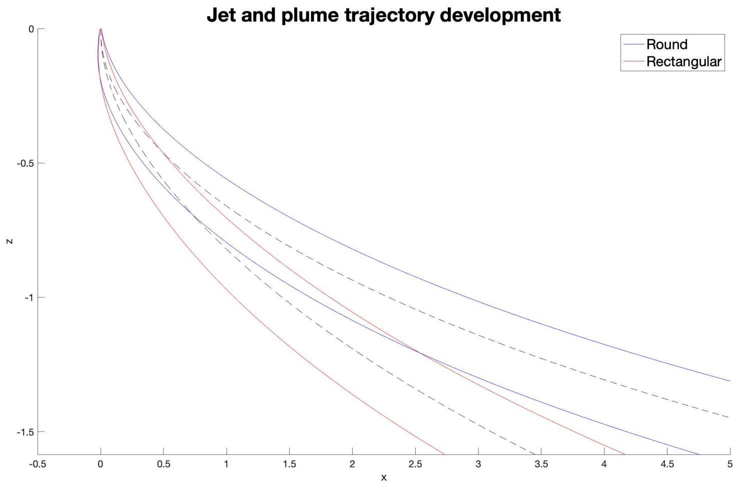


(a) $U_{cf} = 0.02$ m/s

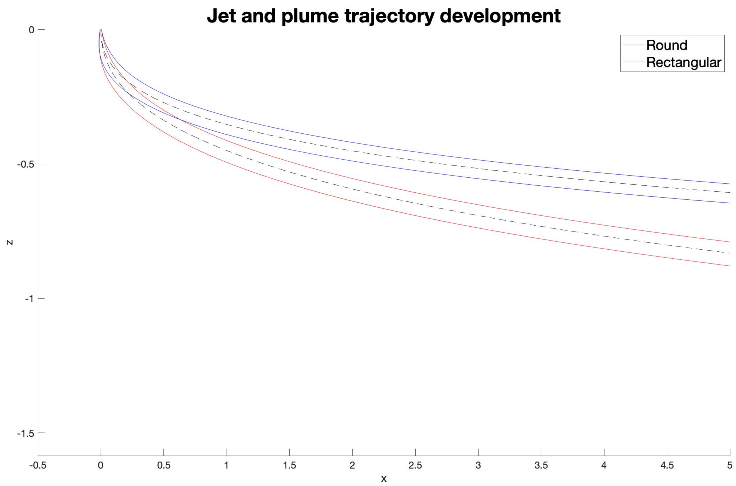


(b) $U_{cf} = 0.035$ m/s

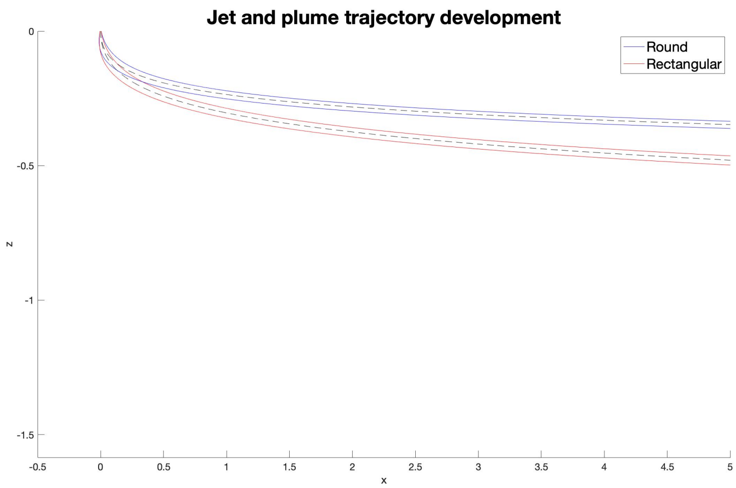


(c) $U_{cf} = 0.05$ m/s

Figure 6.4: Modelled plume trajectories with different crossflow velocities with boundary set as the experiment reservoir width (5.5m)

The model shows results that are expected. Based on the findings in the experiments, the entrainment is less in case of a rectangular outflow shape. Figure 6.4 also shows that an increase in crossflow velocity keeps the plume higher in the ambient water. An increase in crossflow velocity also decreases the thickness of the plume, due to the stronger current. The stronger current decreases the vortex entrainment.
To see the effect of the model better on the depth, the plume trajectory is not locked anymore for the reservoir, but for the simulation time set in the model. Therefore the cases with $U_{cf}$ = 0.035 and 0.01 m/s are further investigated for the simulation time set in the model, which is showed in figure 6.5.

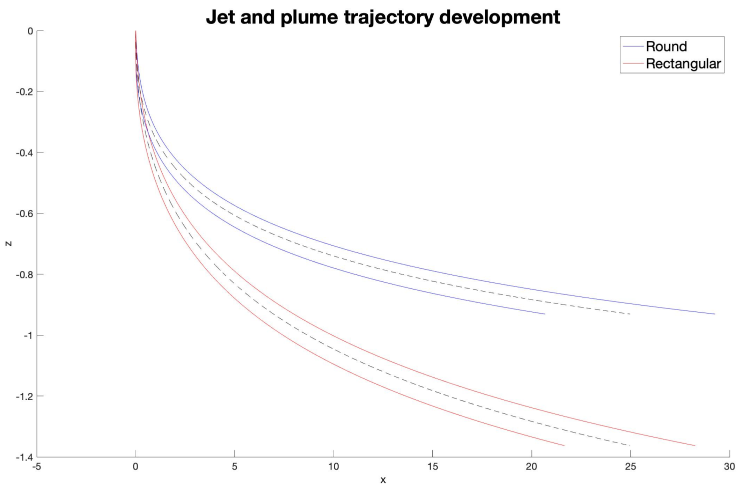


(a) $U_{cf}$ = 0.035 m/s

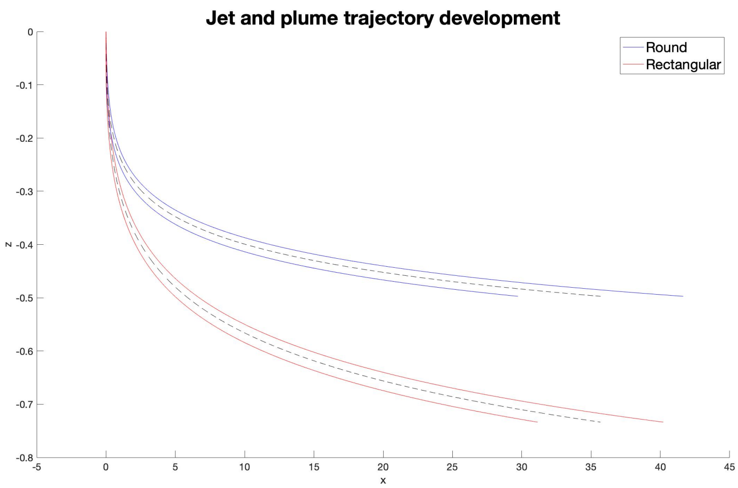


(b) $U_{cf}$ = 0.05 m/s

Figure 6.5: Modelled plume trajectories with different crossflow velocities and simulation time of 5000s

Showing the results based on the total simulation time of 5000s, the difference in plume trajectory is even more visible. In case of $U_{cf}$=0.035m/s, the rectangular nozzle brings the plume to 1.363m depth, whereas the round nozzle brings the plume only to 0.93m depth. This shows a 46% increase in depth. In the case of $U_{cf}$=0.05m/s, the rectangular nozzle brings the plume to a depth of 0.7337m, while the round nozzle reached a maximum depth of 0.4974m. This shows a increase of depth of 47.5%. However, is should be noted that in the model, the effect of depth is not taken into consideration. The resuspension effect is therefore not taken into account. However, it can be seen that a higher crossflow velocity (factor 1.43) brings the plume further (factor 1.44), but keeps the plume significantly higher (factor 1.85).

**Scaling model to practical values**

With the entrainment coefficient found from experiments, it is interesting to see what the plume trajectory is when scaled to practical values. The scaling is done with the two most important mixing parameters of a buoyant jet in crossflow, the densimetric Froude number ($F_\delta$) and the jet-to-crossflow velocity ratio ($\lambda$) which are shown below.

$$F_\Delta = \frac{W_0}{\sqrt{Dg\frac{\Delta\rho}{\rho_w}}} \tag{6.3}$$

$$\lambda = \frac{W_0}{U_{cf}} \tag{6.4}$$

During the experimental tests, it was not possible to scale the parameters properly, due to the boundaries of height of the tank, diameter of the outflow pipe and capability of the pump. However, with the JETLAG model, an indication can be given based on practical values used in the model of Decrop [2016]. Two cases can be considered, a case with low dredging speed and a case with a higher dredging speed. An overview of all parameters is shown in table 6.1.

| **Case** | $\boldsymbol{\rho_0}$ | $\boldsymbol{W_0}$ | **D** | $\boldsymbol{\rho_a}$ | $\boldsymbol{u_{TSHD}}$ |
|---|---|---|---|---|---|
| - | *[$kg/m^3$]* | *[m/s]* | *[m]* | *[$kg/m^3$]* | *[m/s]* |
| 1 | 1034 | 1.9 | 2 | 1000 | 1 |
| 2 | 1034 | 1.9 | 2 | 1000 | 3 |

Table 6.1: Practical values from Decrop [2016] to scale to lab model

With this practical values, both the densimetric Froude number and the jet-to-crossflow velocity ratio can be scaled and implemented in the model. With the experimental setup, the scaling of the densimetric Froude number was not doable, due to the high concentration needed to meet these practical values from Decrop [2016] without a crossflow which can be seen in table 6.2. Based on the scaling, the following properties are used in the model:

| **Case** | $\boldsymbol{W_0*}$ | $\boldsymbol{D*}$ | $\boldsymbol{C_0*}$ | $\boldsymbol{u_{cf}*}$ |
|---|---|---|---|---|
| - | *[m/s]* | *[m]* | *[g/l]* | *[m/s]* |
| 1 | 0.35 | 0.01 | 371 | 0.184 |
| 2 | 0.35 | 0.01 | 371 | 0.555 |

Table 6.2: Scaled lab values implemented in the model

The results of the plume trajectory of Case 1 and Case 2 are shown in figure 6.6. Both cases are modelled with no boundaries and so is based on the simulation time of 5000s. In both cases, the rectangular shape (based on the entrainment coefficient found in the experiment) brings the plume quicker into depth. Comparing the both cases, the effect of $\lambda$ is clearly visible with $\lambda$>1 for case 1 and $\lambda$<1 for case 2. $\lambda$>1 complies with $W_0 > u_{cf}$ and shows this parameter is very important on the effect of the change of shape of the overflow exit.

A high crossflow, will pickup the plume sooner so it cannot reach the depth compared to a lower crossflow. Therefore it can be seen that the plume in case 2 only reach a limited depth compared to case 1. When looking at the depth improvement between the round and rectangular shape, both cases show an improvement of roughly 58%. This complies with the results of the experiments, where the rectangular nozzle created a more dense and less wide plume. With a more dense plume, the effect of for example air entrainment is expected to be less. The added effect of quicker descent of the plume should lead to less interaction with the propeller and a better vertical distribution over the water column, with more sediment in the lower water column.

Decrop [2016] showed with his model a 25-50% decrease of concentration in the upper water column. As the JETLAG model used in this thesis only looks at the different entrainment coefficients between round and rectangular overflow shape, it is likely that other effects that are not modelled in this thesis, like air entrainment and limiting factors like water depth which will induce resuspension of concentration, will decrease the depth improvement found using the JETLAG model.

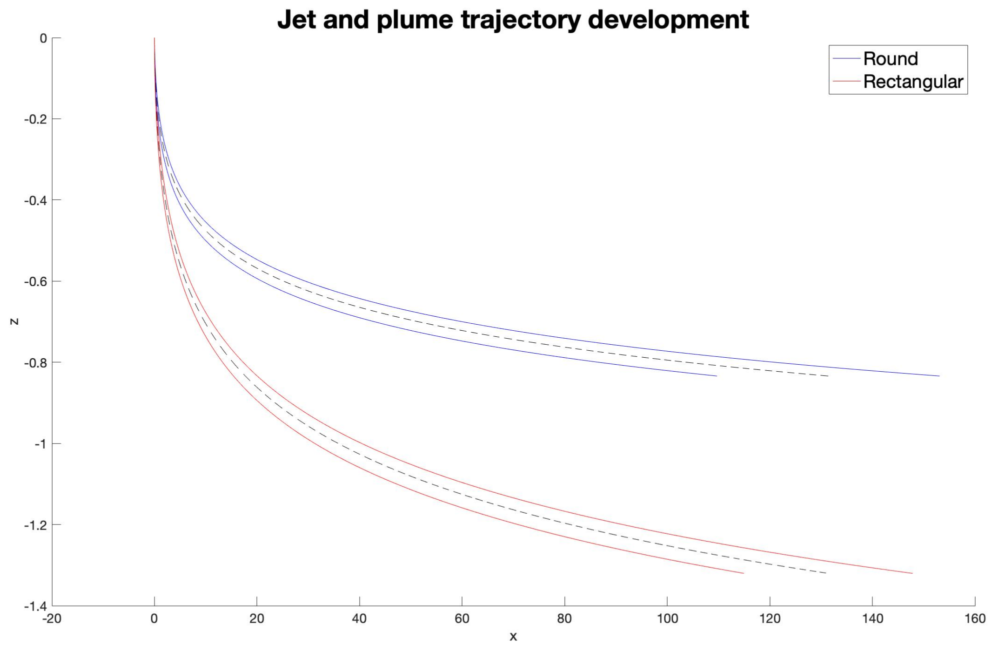


(a) Plume trajectory based on values Case 1 ($U_{cf} = 0.184 m/s, \lambda > 1$)

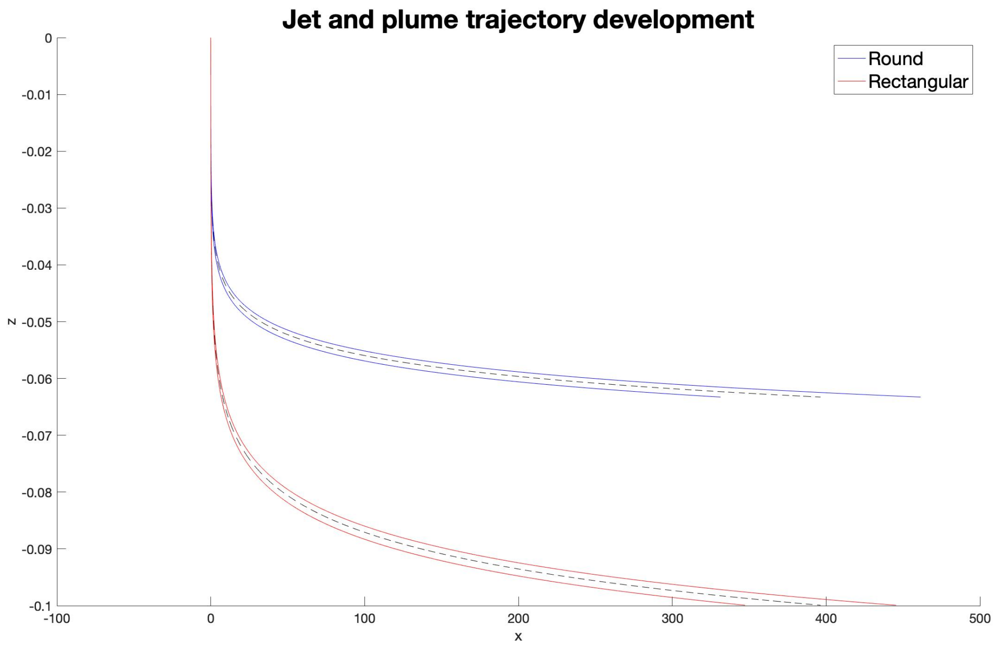


(b) Plume trajectory based on values Case 2 ($U_{cf} = 0.555 m/s, \lambda < 1$)

Figure 6.6: Modelled plume trajectories based on scaled practical values (a) Case 1 (b) Case 2

# 7

# Conclusion & Recommendations

In this chapter, the general outcome of the research is evaluated according to the goals set before the start. The aim of the research was to provide inside which factors influence the amount of surface turbidity and investigate a solution to decrease the surface turbidity. The change of overflow shape was chosen to investigate further by doing experiments in stable water and using the JETLAG model to give an indication of the plume trajectory with crossflow. This leaded to the following research question:

***Can a change in overflow shape cause a decrease of the surface plume***

## 7.1. Conclusion

**Experimental Results**

Changing the overflow shape was achieved by using a rectangular nozzle. Two aspect ratios are tested, both rectangular which can be compared to literature found about jet/plume entrainment with a plane- and round nozzle. The experiments contained concentration- and angle measurements.

Based on all experiments done, the main finding is that the rectangular nozzle shape does decrease the entrainment of the plume in still ambient water. The concentration measurements showed a denser plume in the middle of the plume, which implies that the plume had a smaller angle which indeed was found with the angle measurements.

As said before, the angle measurements did show a smaller angle when changing the nozzle shape from round to rectangular, in both cases. With the corresponding equations, the entrainment coefficient for the rectangular nozzle shapes did decrease, which implies with the finding of a smaller angle. When increasing the aspect ratio, the angle decreases even further, which gives that a higher aspect ratio gives improves the entrainment of the plume in still ambient water. This investigation only showed that increasing the aspect ratio does show positive impact on the plume entrainment. However, at this point, it cannot be said if there is a perfect aspect ratio, which should be further investigated.

It should be noted, that scaling was not possible due to setup used. All results found are based maintaining a turbulent plume but with low velocity to decrease bottom effects. However, bottom effects did show. The bottom plate created radial dispersion of the plume with horizontal currents. Therefore the concentration measurements are less usable, but give an indication of the concentration at that point. Due to the insufficient scaling also the sizing of the nozzles are small. Therefore the effect of the aspect ratio could show other conclusions when using it in practice.

Also the time when measured had effect. The angle of the plume is measured when the plume reached a certain steady state. It was not possible to get a good average angle based on plumes that did not reach the bottom plate yet. The bottom plates creates radial dispersion and so a bigger radius. With the calculation of the angles, the bottom current was neglected (the angle was measured above the horizontal current), but it can be assumed that the table also has effect further above the plate. Therefore measured angles are assumed bigger than angles without a physical boundary.

Concluding the experimental results, the change of overflow shape from round to rectangular shows less entrainment, finding higher concentrations in the middle of the plume and smaller plume angles in still ambient water. Increase in aspect ratio of the rectangular nozzle showed smaller angles no difference in concentration. However, the notes mentioned above should be taken into consideration when reviewing the results.

**Results JETLAG model**
The JETLAG model is used to give an indication of the plume trajectory when it has interaction with a crossflow. Same as for the experiments, the model shows less entrainment in case of the rectangular shape which is logical, based on the smaller entrainment coefficient found for the rectangular shape. When practical values are scaled to lab model scale, the same results are found. The change of overflow shape does have a positive influence on the plume trajectory (smaller plume width, quicker descent) but the effect of crossflow velocity is an important factor in this case.

Concluding the results of the JETLAG model, the change of overflow shape from round to rectangular shows less sediment in the upper water column and so decreases the surface plume. However, it should be noted that the model is purely an indication, because experiments with the same conditions are not done and other influence factors are not taken into account for example water depth and air entrainment.

## 7.2. RECOMMENDATIONS

Recommendations are based on the experimental setup and numerical model, which are presented in this section.

**Experimental**
The experimental setup used, is designed for another purpose: deepsea mining. Therefore with the setup used, scaling was not possible. The limiting factor of depth, outflow diameter and pump where the main problems. Due to the limiting depth, the pump discharge was adjusted to maintain a turbulent plume, but keeping a low velocity to decrease bottom effects. Also it was not possible to have the whole height in the frame of the camera. Therefore to do better experiments, a whole new setup should be created to reach the scaling with reality. Two experimental setups can be thought of, one with and one without crossflow.
*Without crossflow*

- Use a deep tank, width less important
- Good pipe diameter and pump discharge to scale to reality
- Use other method to measure concentration. Not at the bottom plate, but at a certain depth (without physical bottom) which can give more reliable values.
- Capture total height in camera frame
- Implement a frame with physical measuring units, in order to give a good estimation of, for example, plume width beforehand.

*With crossflow*

- Length of tank more important than depth in combination with the ambient velocity
- Good pipe diameter and pump discharge to scale to reality
- Use other method to measure concentration. Not at the bottom plate, but at a certain depth (without physical bottom) which can give more reliable values.
- Capture total height/width in camera frame
- Implement a frame with physical measuring units, in order to give a good estimation of, for example, plume width beforehand.

**Numerical**
The JETLAG model is based on a round outflow exit. Therefore differences on momentum of round / plane outflow shapes are not implemented in the model. Chapter 3 showed differences between round (3D) and plane (2D) outflow exits. When it is possible to create a 3D model with a rectangular outflow exit, the models can be better compared to give even more reliable information. Instead of this, the only difference in the JETLAG model is the entrainment coefficient which is implemented as a constant. Combining shear entrainment and vortex entrainment in a crossflow the entrainment coefficient can differ over time. Comparing the model with experiments with crossflow will improve the indication of the plume trajectory in this model.

Next to that is the fact that the aspect ratio of the rectangular nozzle should be further investigated to see if there is a perfect aspect ratio for the best entrainment of the plume. This thesis showed that increasing the aspect ratio does show less entrainment, however it did not show if there is a perfect aspect ratio spot. This could be done both experimental or numerical.

# A

# Current designs to decrease overflow turbidity

The surface turbidity is a problem in the present and future. Certain partial solutions are existing these days, which are described in this appendix. Both solutions are solvers for the air problem.

**Green valve / Environmental valve**

The green valve, or so called environmental valve, is a valve which is placed inside the overflow. The valve can be set to certain angles to choke the flow in the overflow in such a way that a constant fluid level in the hopper in maintained and so reduce the plunging manner of inflow. The valve nowadays is integrated in the automation system of the TSHD and entering a few settings is sufficient to activate the system. Pump velocity, dredged concentration, amount of pumps are some things the automatic system works with. A picture of an environmental valve is shown in figure A.1.


Figure A.1: Environmental valve inside the overflow

Numerical research is done investigating the environmental valve, for example by [Saremi & Jensen, 2014b] and [Decrop, 2016]. Saremi & Jensen [2014b] created a two-phase numerical model implemented in OpenFOAM based on the Volume of Fluid method [Hirt & Nichols, 1981]. This numerical model is used to simulate the performance of the environmental valve. Figure A.2 shows the air-water interface from the CFD results.
The numerical results confirm the effectiveness of the valve in reducing the rate of entrainment of the air bubbles into the overflow. The presence of the valve causes an extra hydraulic resistance to the flow passing through the shaft and reduces the flow rate. This reduction results in smaller Froude numbers inside the shaft and therefore reduces the critical submergence at the shaft intake which then results in less air entrainment.

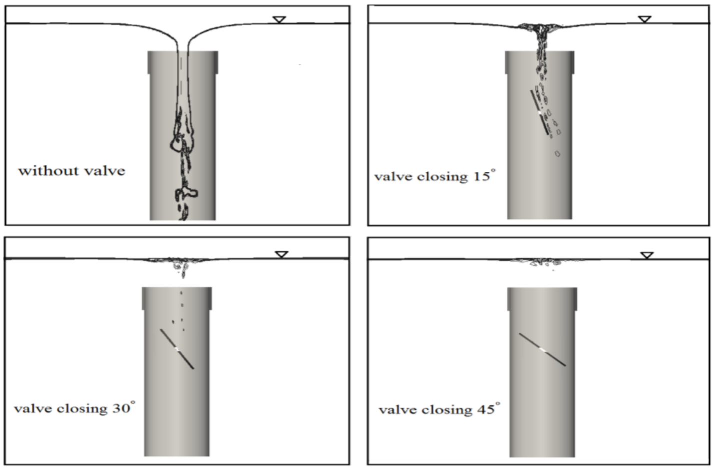


Figure A.2: Air-water interface from the CFD results

The results from the numerical model also show the reduction in the flow rate through the shaft (figure A.3), which is always been considered as a draw back of using the green valve. However, the results tell that the rate of reduction in the air entrainment due to closure of the valve is far more higher than the relative reduction in the flow rate for the corresponding valve closure.

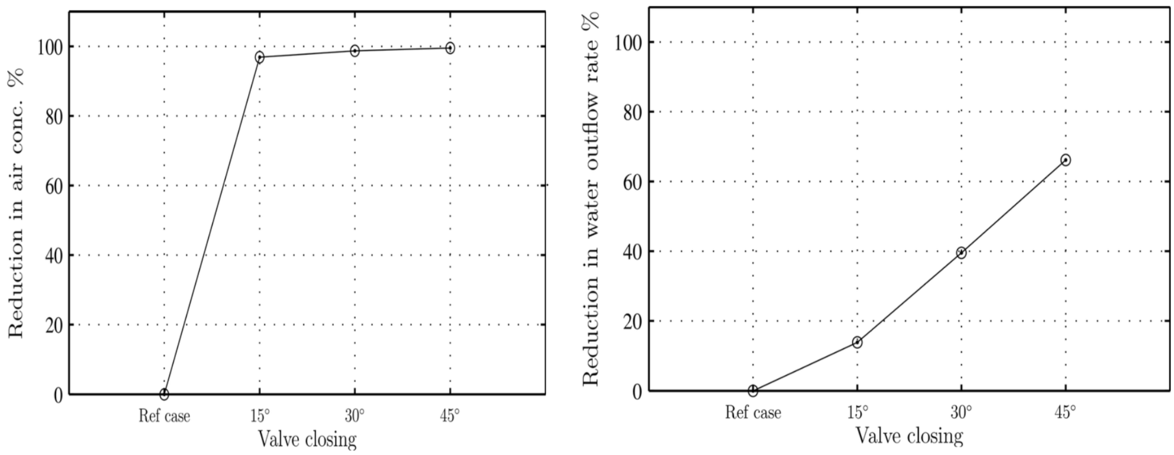


Figure A.3: Reduction in air entrainment (left) and water flux (right)

Decrop [2016] concluded that the environmental valves indeed can reduce the surface plumes with a high efficiency in many cases. However, it is also shown that under certain circumstances the efficiency can drop significantly, to nearly zero in some cases. It is shown that the valve efficiency is a function of (i) the distance from the overflow to the stern, (ii) the overflow shaft diameter, (iii) the overflow sediment concentration and (iv) the relative speed of the vessel through the water.
It was found that an environmental valve positioned close to the stern increases the probability that the efficiency will drop during operation. In case of such unfavourable overflow position, the operation of the vessel is dominant in the valve's efficiency. In case an unfavourable overflow position is combined with a high sailing speed or head-on current, the efficiency of the valve drops to nearly zero.
On the other hand, in case of a favourable overflow construction - a narrow shaft, positioned at large distance from stern - only exceptional operational circumstances will reduce the efficiency of the valve significantly.

The environmental valve is a great way to decrease the surface plume of a TSHD. However, the main drawback is the valve it self which is located in the overflow and so hard reachable to maintain. Also the valve has moving parts which will suffer from the water-sediment mixture that flows trough the overflow and so must be replaced every now and then. These factors brought to the fact that another solution could be investigated.

**Royal IHC Plumigator® Overflow**

In 2017, Royal IHC [2017] came with the patented plumigator® overflow which is an upgrade to the telescopic overflow system. It is designed to guarantee an optimal, non-turbulent flow inside the hopper. Additional, the plumigator® overflow has no additional moving parts unlike the traditional green valve, is an integration with newly-built vessels or can be retrofitted to current TSHD's and has a reduction of a vessel's ecological impact. An image of the plumigator® overflow is shown below in figure A.4.


Figure A.4: Royal IHC Plumigator® Overflow

Royal IHC claims that the plumigator® overflow tackles the undesirable plume created around the vessel, which is know to harm marine life. A loss of performance can also be incurred, as well as additional downtime and maintenance costs. In addition, draft sensors can sometimes give inaccurate readings, which can have an impact on overall vessel performance.

The issues occur when air is released beneath the vessel by the regular overflow. This combines with entrapped fine soil particles, and the mixture remains near the hull. As it moves through the propellers, a large surface area will be covered and this appears as a plume. By entering the intake valves of the pumps and auxiliary equipment, the performance and lifetime of the system are affected.

Royal IHC claims that the patented design significantly limits the influx of air in the overflow, and contributes to a hassle-free operation. The multiple inlet openings also reduce the velocity in the hopper, allowing the mixture extra time to settle. However, the amount of influx of air that is reduced is not made public.

# B

# Chronological work plan experiment

| Preperations | | |
|---|---|---|
| *Step 1* | ☐ | Fill the reservoir (25m³) with tap water by using fire hose |
| Step 2 | ☐ | Sieving of quartz powder to remove bigger flocs that could cause damage to the KATFLOW sensor |
| Step 3 | ☐ | Clean the table in the reservoir before each test to remove sediment from the table, done by a submersible vacuum cleaner |
| | ☐ | Clean vials and sample trays for turbidity experiment |
| Step 4 | ☐ | Install jet pipe at right height (158,5cm) from table |
| | ☐ | Check KATflow sensor alignment |
| | ☐ | Install right outflow shape (rectangular 20x3.9 or 30x2.6) or not (round) |
| Step 5 | ☐ | Prepare the water-sediment mixture in the mixing tank of the required initial SSC (5g/L) |
| | | |
| **Video recording** | | |
| Step 6 | ☐ | Adjust camera to right preferences |
| | ☐ | Fix camera on tripod |
| | ☐ | Fix camera in right position |
| | ☐ | Go Pro inside water |
| | ☐ | Camera outside water |
| Step 7 | ☐ | Start the mixing pump ant wait until the water-sediment mixture is homogeneous |
| Step 8 | ☐ | Measure water temperature of the reservoir |
| | ☐ | Maintain same temperature in the mixing tank |
| Step 9 | ☐ | Start KATflow meter |
| Step 10 | ☐ | Start video recording |
| Step 11 | ☐ | Start the jet pump |
| | ☐ | Open carefully the jet valve and regulate the flow to an uniform and constant flow (0.3m/s) with the KATflow meter. |
| | ☐ | Keep the temperature in the mixing tank constant by adding ice to decrease the temperature due to mixing pump heat emission |
| Step 12 | ☐ | Record experiment until steady state is reached |
| | ☐ | Stop camera recording |
| | ☐ | Go Pro inside water |
| | ☐ | Camera outside water |

| | | |
|---|---|---|
| **Local Turbidity measurement** | | |
| Step 13 | ☐ | Sample from the tubes 100 ml for each location on measurement map starting from points closer to IP (impingement point). Points of equal distance from IP in x-axis and y- axis should be sampled simultaneously. |
| Step 14 | ☐ | Stop jet pump |
| | ☐ | Close jet valve |
| | ☐ | Stop KATflow meter |
| | ☐ | Stop mixing pump |
| Step 15 | ☐ | Resample three vials for each sample of step 13 |
| | ☐ | Clean and wipe outside of vial |
| | ☐ | Shake for one minute to create homogeneous mixture |
| | ☐ | Place in Turbidimeter AL450T-IR |
| | ☐ | Measure amount of NTU (read button) |
| **END local turbidity measurement** | | |

# C

# Schematic overview experimental setup

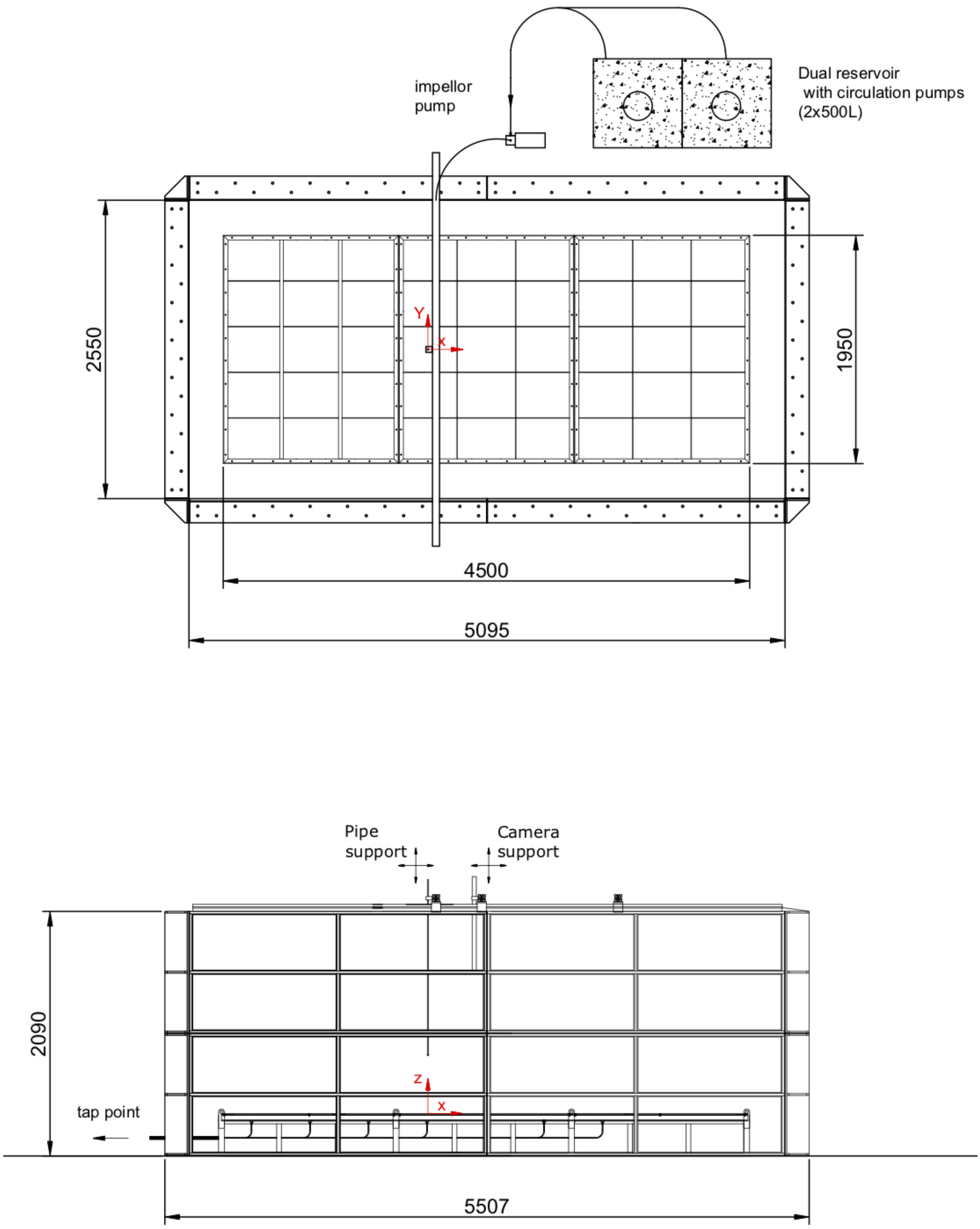


Figure C.1: Schematic overview of the experimental setup used at TU Delft

# D

# Overview Calibration Turbidimeter AL450T-IR

| mg/l | g/l | NTU measured #1 | NTU measured #2 | NTU treasured #3 | Mean NTU | St. Dev (mean NTU) | Formula | St dev. (Formule) |
|---|---|---|---|---|---|---|---|---|
| 50 | 0,05 | 15,15 | 14,8 | 13,05 | 14,3 | 0,9 | 14,0 | 1,0 |
| 100 | 0,1 | 19 | 22,85 | 22,7 | 21,5 | 1,8 | 19,6 | 2,6 |
| 125 | 0,125 | 19,65 | 20,5 | 21,35 | 20,5 | 0,7 | 22,4 | 2,1 |
| 150 | 0,15 | 26,1 | 23,75 | 26,35 | 25,4 | 1,2 | 25,3 | 1,2 |
| 175 | 0,175 | 30,05 | 25,45 | 25,65 | 27,1 | 2,1 | 28,1 | 2,4 |
| 200 | 0,2 | 32,9 | 28,7 | 31 | 30,9 | 1,7 | 30,9 | 1,7 |
| 250 | 0,25 | 38,35 | 36,95 | 37,55 | 37,6 | 0,6 | 36,5 | 1,2 |
| 300 | 0,3 | 40,15 | 41,85 | 46 | 42,7 | 2,5 | 42,2 | 2,5 |
| 350 | 0,35 | 45,45 | 47,4 | 45,4 | 46,1 | 0,9 | 47,8 | 2,0 |
| 400 | 0,4 | 47,65 | 59,55 | 53,1 | 53,4 | 4,9 | 53,5 | 4,9 |
| 500 | 0,5 | 63,85 | 63,7 | 69 | 65,5 | 2,5 | 64,7 | 2,6 |

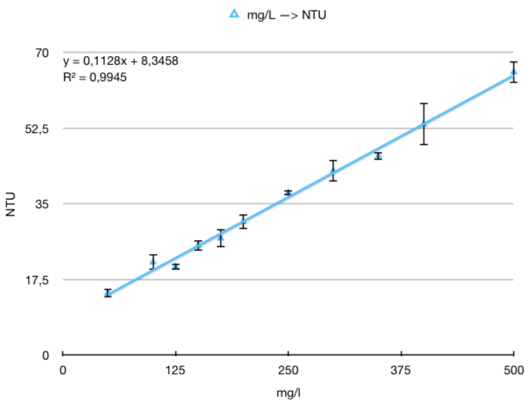


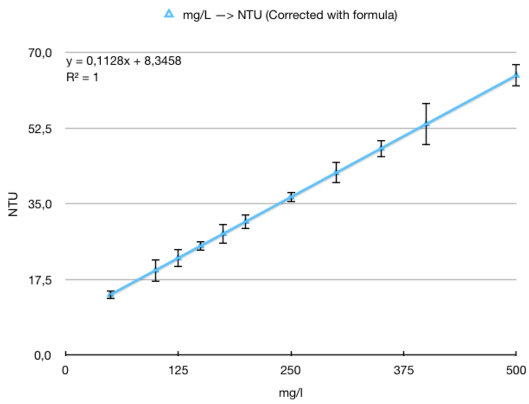


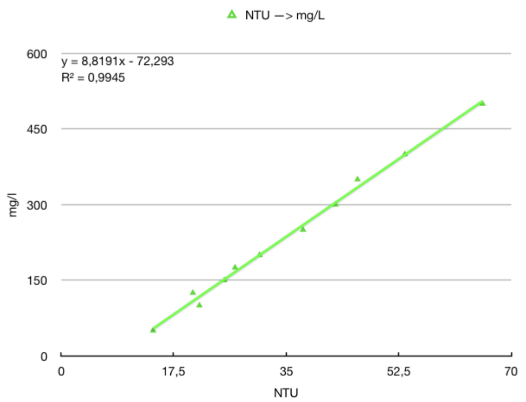

# E

# Overview Concentration measurement results

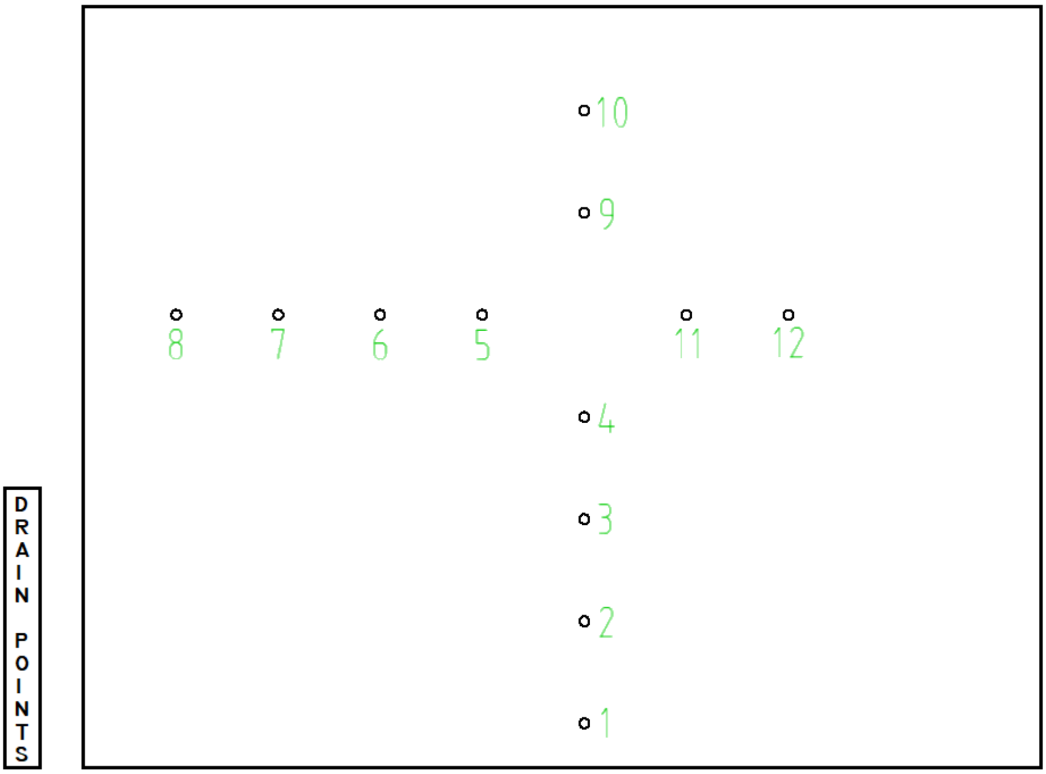


Figure E.1: Overview of measuring points. All of the points have a certain radius from the centre point. (4,5,9,11 = 100mm / 3,6,10,12 = 200mm / 2,7 = 300mm / 1,8 = 400mm)

*Average 5 Measurements Round*

| Measuring point | Test 1 | Test 2 | Test 3 | Test 4 | Test 5 | Average NTU | Average mg/l |
|---|---|---|---|---|---|---|---|
| 1 | 7,02 | 6,51 | 8,46 | 7,68 | 7,88 | 7,51 | 15,91 |
| 2 | 11,41 | 9,74 | 6,31 | 7,92 | 8,76 | 8,83 | 26,67 |
| 3 | 11,96 | 11,34 | 8,75 | 9,91 | 10,00 | 10,39 | 39,45 |
| 4 | 13,92 | 11,88 | 9,25 | 10,54 | 10,57 | 11,23 | 46,32 |
| 5 | 13,33 | 12,81 | 9,79 | 11,14 | 10,20 | 11,46 | 48,15 |
| 6 | 12,38 | 11,14 | 9,73 | 9,54 | 9,20 | 10,40 | 39,51 |
| 7 | 10,77 | 8,68 | 7,18 | 8,17 | 7,42 | 8,44 | 23,54 |
| 8 | 8,81 | 7,30 | 8,20 | 7,29 | 7,08 | 7,74 | 17,76 |
| 9 | 13,50 | 13,38 | 10,45 | 10,87 | 10,44 | 11,73 | 50,37 |
| 10 | 12,60 | 10,78 | 10,53 | 10,15 | 9,81 | 10,78 | 42,59 |
| 11 | 12,88 | 12,02 | 10,00 | 10,55 | 10,46 | 11,18 | 45,89 |
| 12 | 11,59 | 11,58 | 9,68 | 10,09 | 9,98 | 10,58 | 41,02 |
| | | | | | | | |
| | | | | | | | |
| | | | | | | Average | 47,68 |
| | | | | | | | 40,64 |
| | | | | | | | 25,10 |
| | | | | | | | 16,83 |

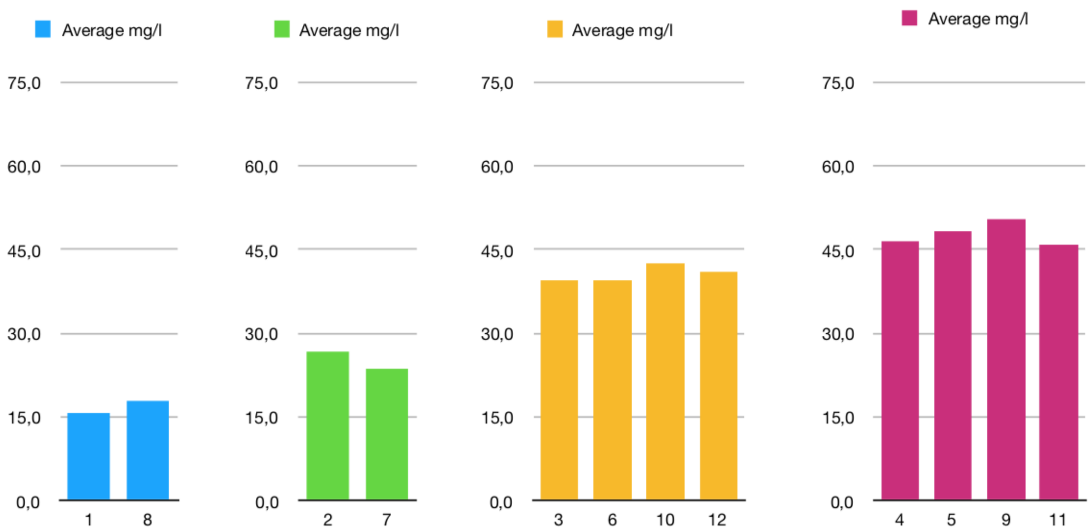


Figure E.2: Overview of concentration measurements with round overflow shape

**Average 4 Measurements Rectangular 20x3.9**

| Measuring point | Test 1 | Test 2 | Test 3 | Test 4 | | Average NTU | Average mg/l | |
|---|---|---|---|---|---|---|---|---|
| 1 | 8,77 | 6,83 | 9,38 | 9,09 | | 8,52 | 24,15 | |
| 2 | 9,69 | 7,74 | 9,59 | 9,62 | | 9,16 | 29,40 | |
| 3 | 11,33 | 10,47 | 10,61 | 10,57 | | 10,75 | 42,36 | |
| 4 | 12,54 | 12,07 | 13,13 | 13,20 | | 12,74 | 58,61 | |
| 5 | 12,57 | 12,04 | 11,63 | 13,44 | | 12,42 | 56,04 | |
| 6 | 11,39 | 10,73 | 10,20 | 10,92 | | 10,81 | 42,87 | |
| 7 | 9,36 | 8,95 | 8,48 | 9,68 | | 9,12 | 29,04 | |
| 8 | 9,07 | 6,72 | 7,94 | 9,23 | | 8,24 | 21,87 | |
| 9 | 13,87 | 12,66 | 11,96 | 13,78 | | 13,06 | 61,29 | |
| 10 | 11,58 | 10,91 | 9,91 | 10,81 | | 10,80 | 42,83 | |
| 11 | 14,37 | 12,62 | 10,81 | 13,46 | | 12,81 | 59,25 | |
| 12 | 11,89 | 11,60 | 9,62 | 10,85 | | 10,99 | 44,33 | |
| | | | | | | | | |
| | | | | | | | | |
| | | | | | | Average | 58,80 | |
| | | | | | | | 43,10 | |
| | | | | | | | 29,22 | |
| | | | | | | | 23,01 | |
| | | | | | | | | |

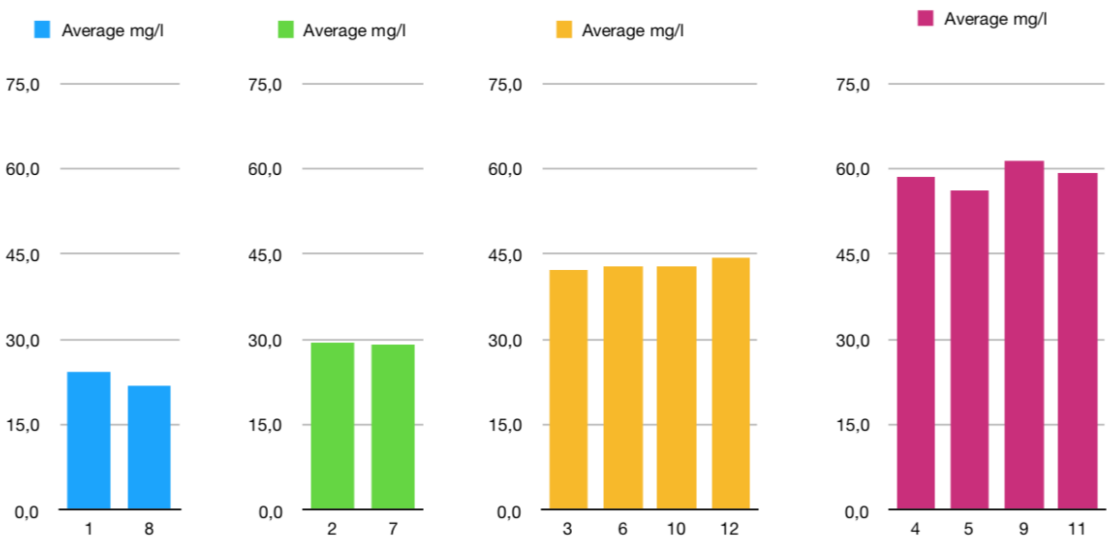


Figure E.3: Overview of concentration measurements with rectangular (20x3.9mm) overflow shape

**Average 5 Measurements Rectangular 30x2.6**

| Measuring point | Test 1 | Test 2 | Test 3 | Test 4 | Test 5 | Average NTU | Average mg/l |
|---|---|---|---|---|---|---|---|
| 1 | 5,85 | 7,33 | 8,20 | 7,77 | 7,66 | 7,36 | 14,71 |
| 2 | 6,51 | 8,52 | 9,52 | 9,73 | 10,07 | 8,87 | 27,03 |
| 3 | 9,93 | 9,50 | 11,36 | 10,61 | 10,84 | 10,45 | 39,94 |
| 4 | 12,43 | 10,46 | 12,81 | 12,52 | 12,84 | 12,21 | 54,35 |
| 5 | 13,28 | 11,88 | 11,23 | 13,69 | 12,22 | 12,46 | 56,35 |
| 6 | 10,96 | 10,28 | 9,61 | 10,96 | 10,36 | 10,43 | 39,78 |
| 7 | 9,60 | 8,62 | 8,51 | 9,55 | 9,16 | 9,09 | 28,80 |
| 8 | 7,91 | 7,28 | 8,36 | 7,53 | 7,83 | 7,78 | 18,13 |
| 9 | 11,69 | 12,42 | 12,59 | 12,57 | 12,47 | 12,35 | 55,43 |
| 10 | 10,16 | 11,69 | 11,37 | 10,98 | 11,12 | 11,06 | 44,93 |
| 11 | 13,69 | 13,31 | 11,28 | 14,59 | 12,28 | 13,03 | 61,00 |
| 12 | 12,07 | 12,28 | 9,72 | 11,79 | 11,41 | 11,45 | 48,13 |
| | | | | | | Average | 56,78 |
| | | | | | | | 43,19 |
| | | | | | | | 27,91 |
| | | | | | | | 16,42 |

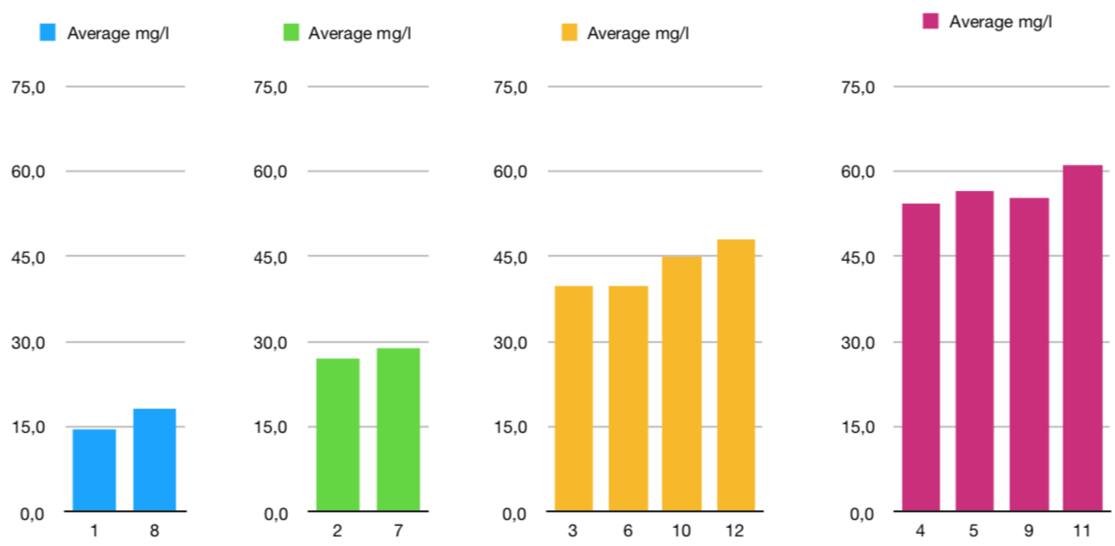


Figure E.4: Overview of concentration measurements with rectangular (30x2.6mm) overflow shape

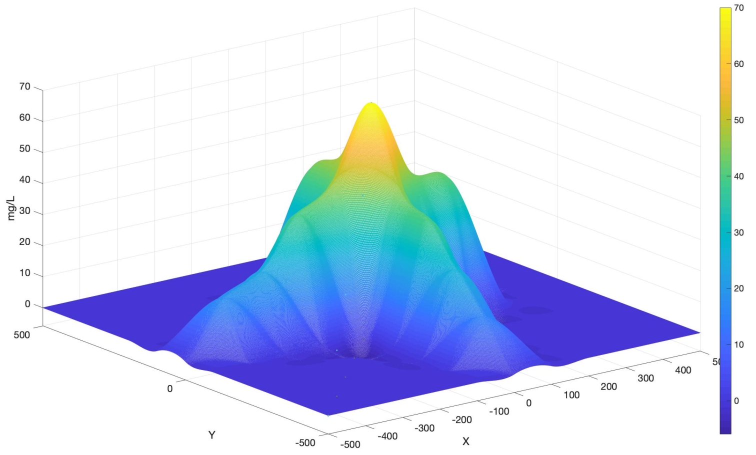


Figure E.5: Side view visualisation Round nozzle shape (measurement points only)

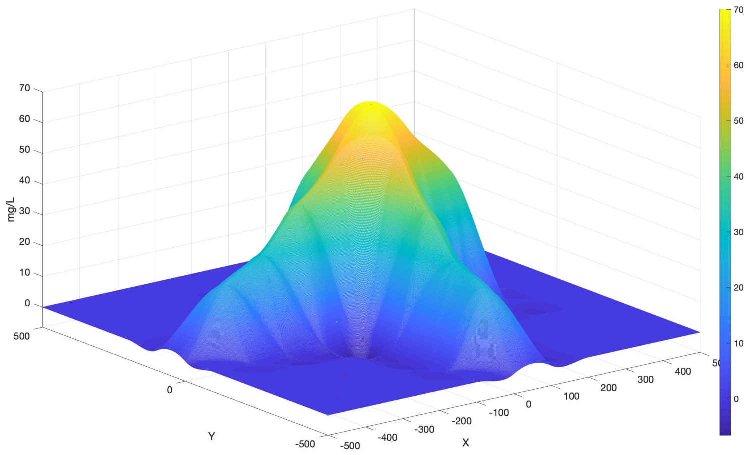


Figure E.6: Side view visualisation Rectangular 20x3.6 nozzle shape (measurement points only)

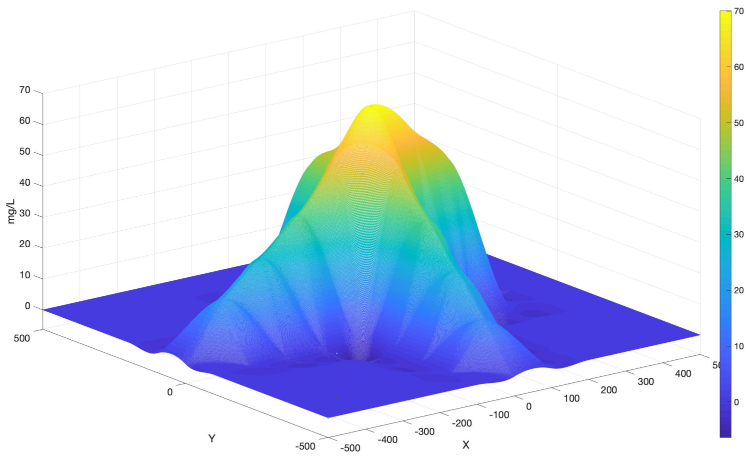


Figure E.7: Side view visualisation Rectangular 30x2.6 nozzle shape (measurement points only)

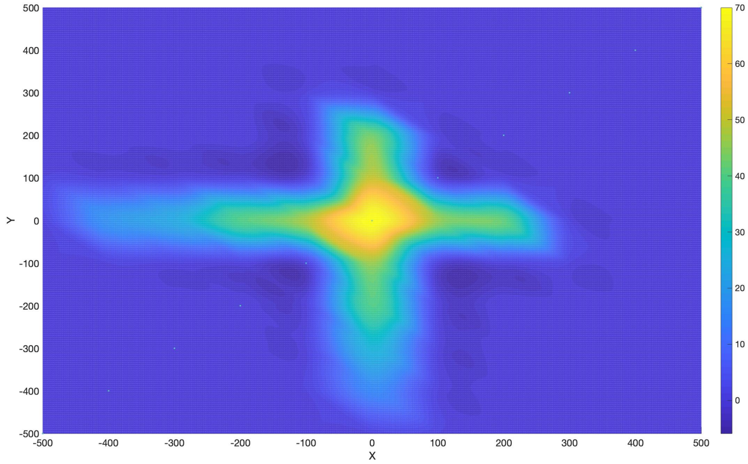


Figure E.8: Top view visualisation Round nozzle shape (measurement points only)

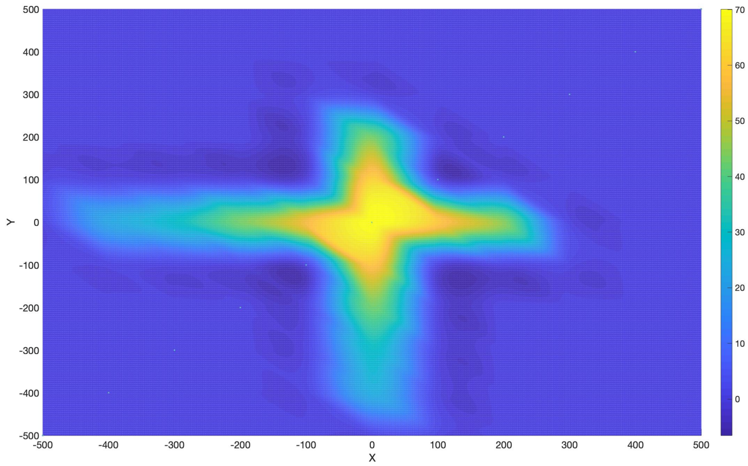


Figure E.9: Top view visualisation Rectangular 20x3.6 nozzle shape (measurement points only)

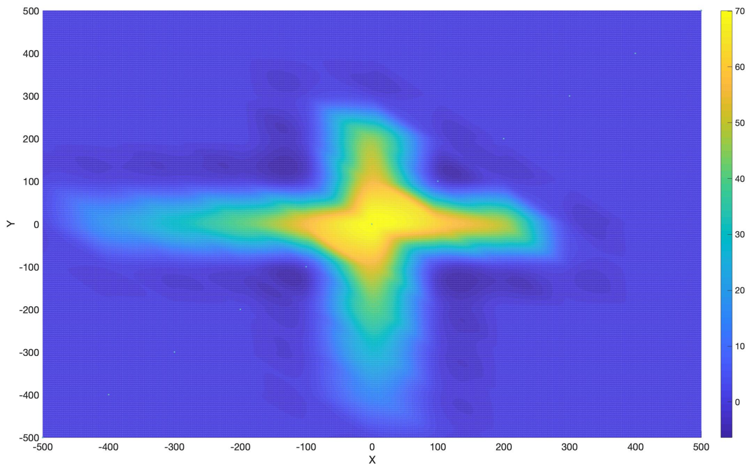


Figure E.10: Top view visualisation Rectangular 30x2.6 nozzle shape (measurement points only)

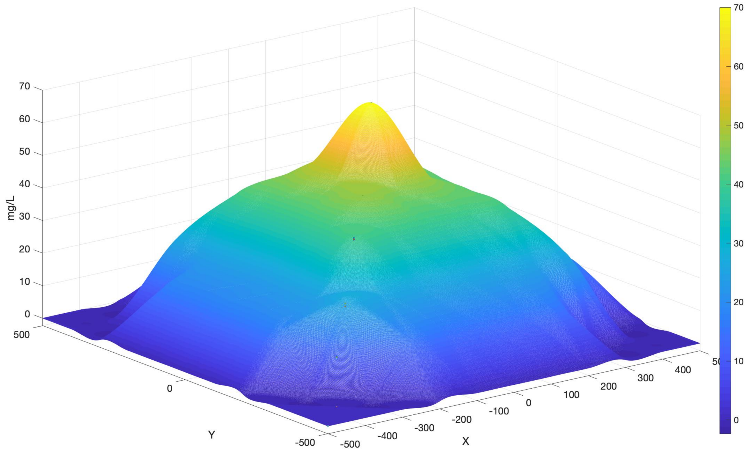


Figure E.11: Side view visualisation Round nozzle shape (800x800 grid)

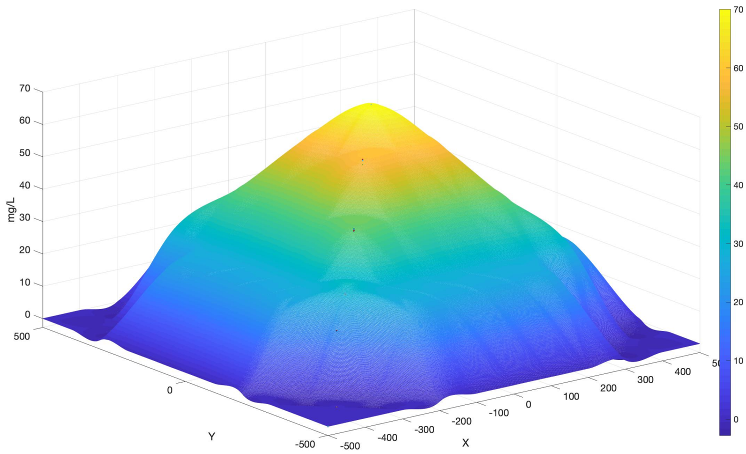


Figure E.12: Side view visualisation Rectangular 20x3.6 nozzle shape (800x800 grid)

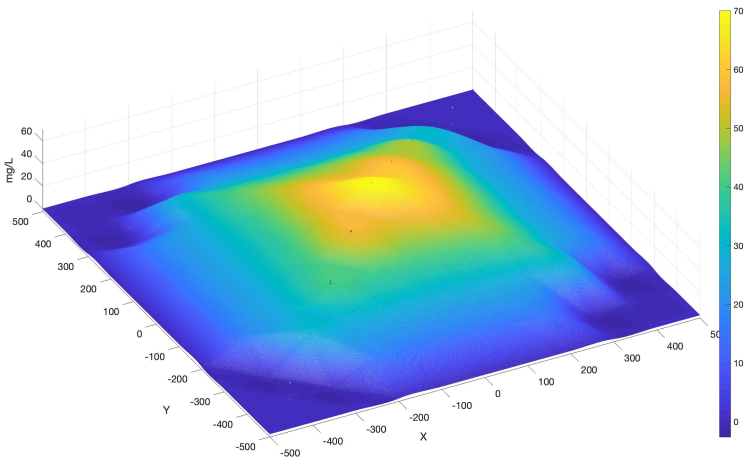


Figure E.13: Side view visualisation Rectangular 30x2.6 nozzle shape (800x800 grid)

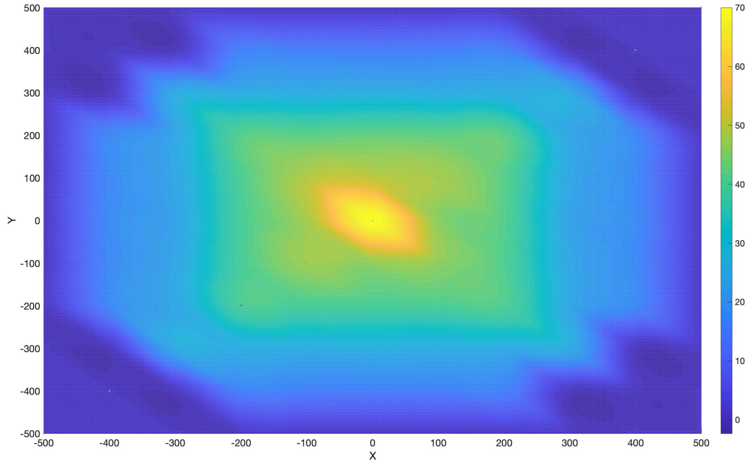


Figure E.14: Top view visualisation Round nozzle shape (800x800 grid)

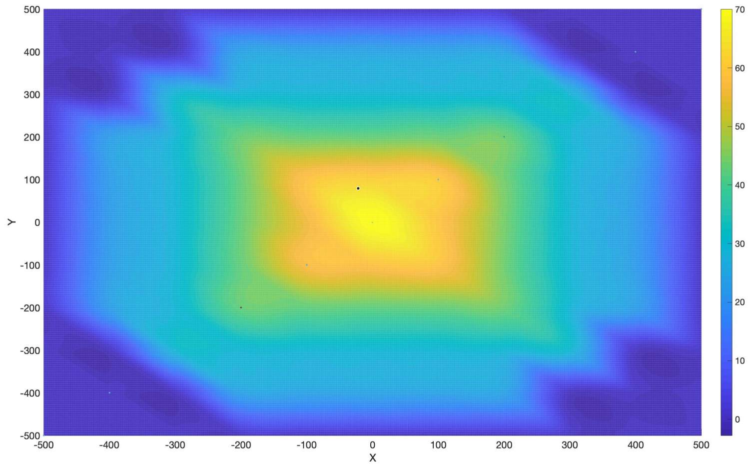


Figure E.15: Top view visualisation Rectangular 20x3.6 nozzle shape (800x800 grid)

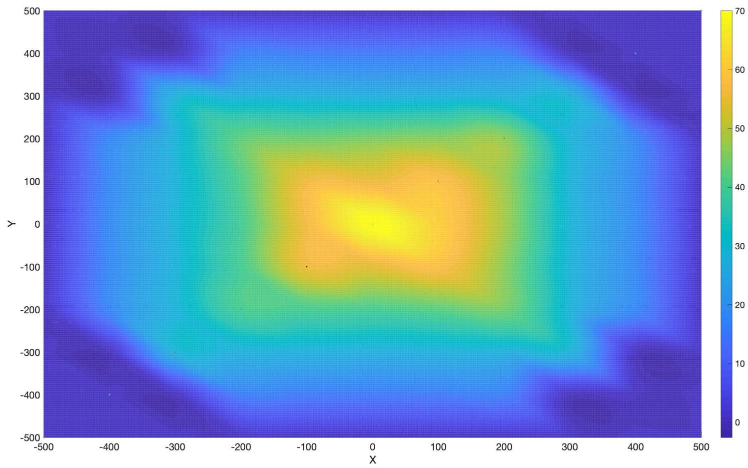


Figure E.16: Top view visualisation Rectangular 30x2.6 nozzle shape (800x800 grid)

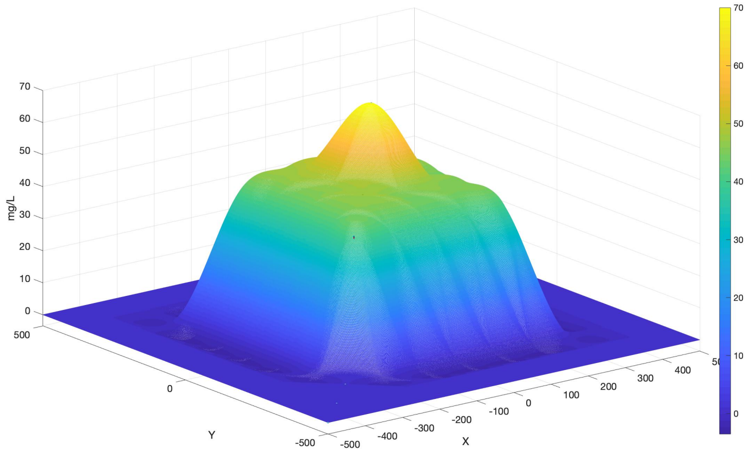


Figure E.17: Side view visualisation Round nozzle shape (400x400 grid)

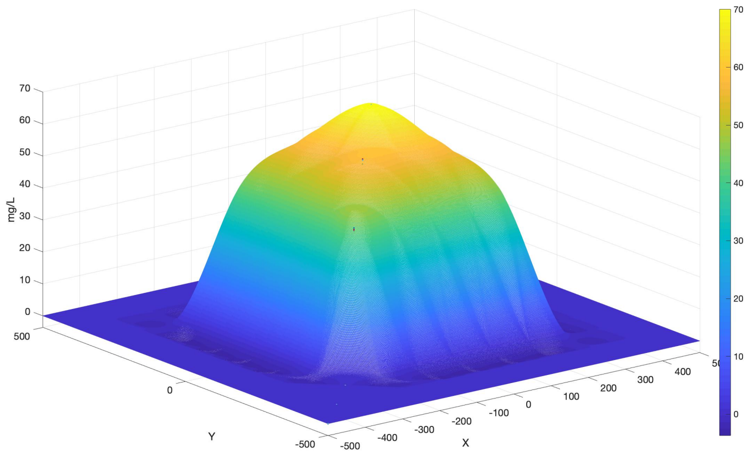


Figure E.18: Side view visualisation Rectangular 20x3.6 nozzle shape (400x400 grid)

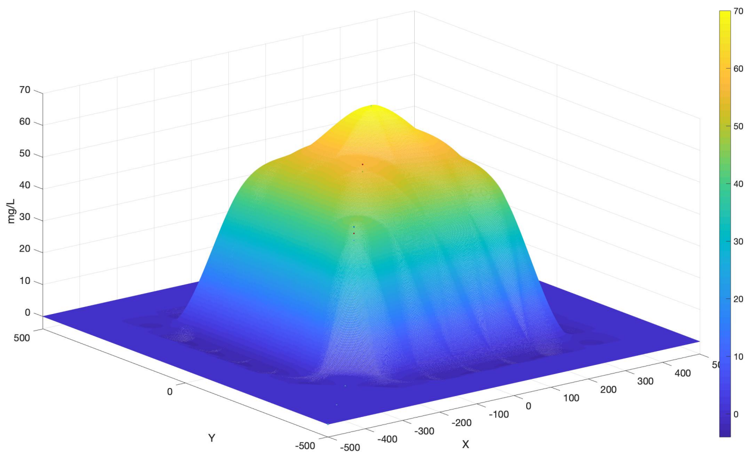


Figure E.19: Side view visualisation Rectangular 30x2.6 nozzle shape (400x400 grid)

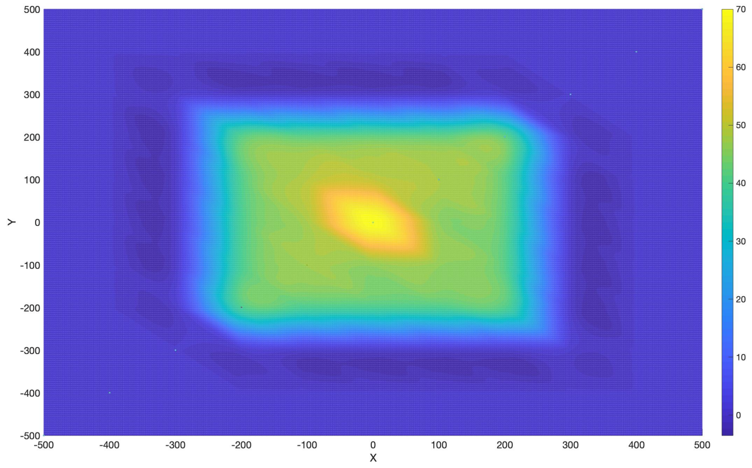


Figure E.20: Top view visualisation Round nozzle shape (400x400 grid)

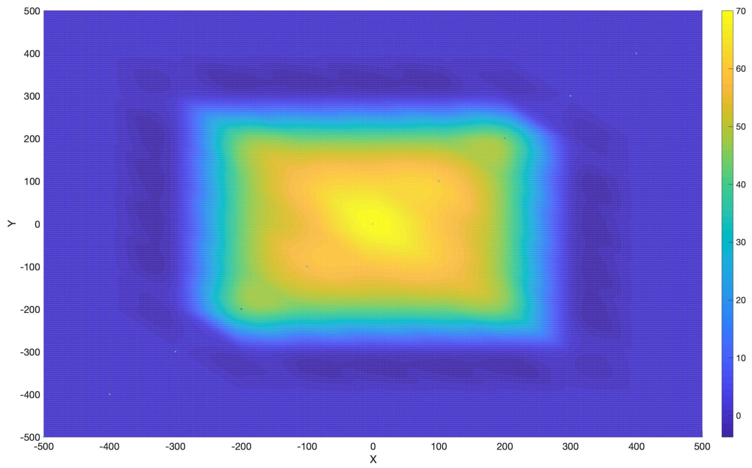


Figure E.21: Top view visualisation Rectangular 20x3.6 nozzle shape (400x400 grid)

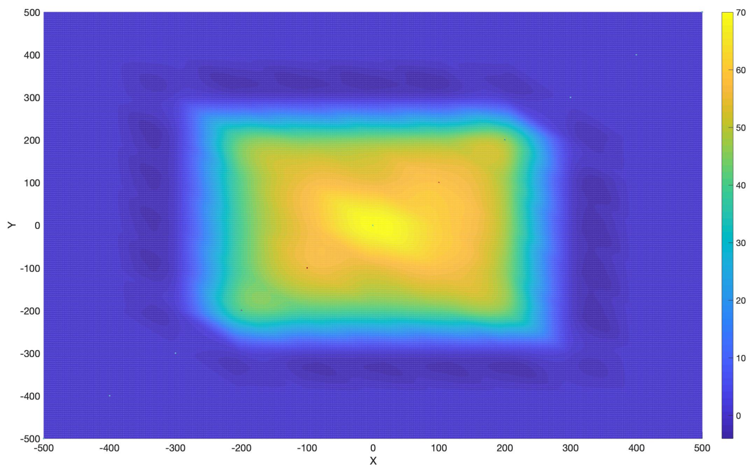


Figure E.22: Top view visualisation Rectangular 30x2.6 nozzle shape (400x400 grid)

# F

# Overview Angle measurement results

| R1_t100 | | | |
|---|---|---|---|
| Left | | Right | |
| Row | Column | Row | Column |
| 23 | 877 | 43 | 1101 |
| 96 | 854 | 84 | 1136 |
| 137 | 824 | 146 | 1151 |
| 187 | 823 | 230 | 1150 |
| 228 | 834 | 314 | 1173 |
| 372 | 828 | 377 | 1213 |
| 490 | 795 | 466 | 1215 |
| 524 | 769 | 573 | 1280 |
| 637 | 750 | 684 | 1281 |
| 773 | 743 | 777 | 1306 |
| 828 | 739 | 843 | 1314 |

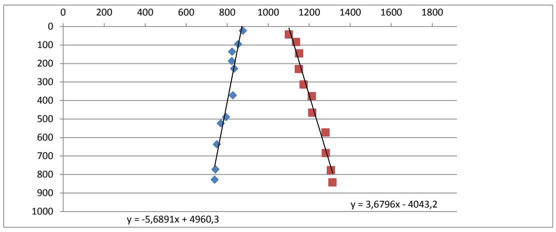


Angle 25,17

| R2_t100 | | | |
|---|---|---|---|
| Left | | Right | |
| Row | Column | Row | Column |
| 42 | 859 | 12 | 1128 |
| 81 | 852 | 90 | 1175 |
| 120 | 870 | 235 | 1186 |
| 261 | 910 | 290 | 1208 |
| 333 | 902 | 429 | 1211 |
| 443 | 846 | 190 | 1236 |
| 533 | 826 | 537 | 1271 |
| 572 | 800 | 644 | 1276 |
| 668 | 822 | 720 | 1318 |
| 739 | 834 | 792 | 1377 |

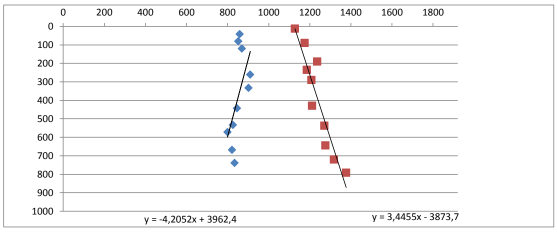


Angle 29,56

| R3_t100 | | | |
|---|---|---|---|
| Left | | Right | |
| Row | Column | Row | Column |
| 39 | 906 | 9 | 1175 |
| 110 | 905 | 92 | 1155 |
| 176 | 896 | 163 | 1162 |
| 242 | 870 | 231 | 1155 |
| 285 | 855 | 324 | 1184 |
| 374 | 806 | 389 | 1184 |
| 439 | 809 | 461 | 1166 |
| 527 | 858 | 527 | 1230 |
| 643 | 795 | 586 | 1284 |
| 679 | 787 | 690 | 1279 |
| 797 | 808 | 762 | 1283 |

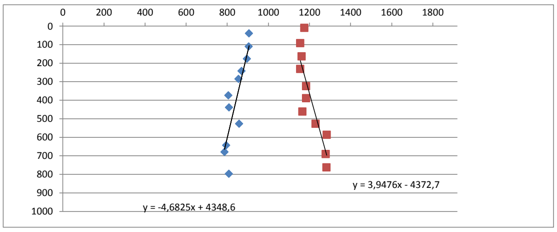


Angle 26,27

| R4_t100 | | | |
|---|---|---|---|
| Left | | Right | |
| Row | Column | Row | Column |
| 23 | 905 | 22 | 1107 |
| 73 | 898 | 127 | 1108 |
| 132 | 890 | 226 | 1093 |
| 191 | 920 | 344 | 1118 |
| 244 | 881 | 472 | 1129 |
| 343 | 859 | 531 | 1185 |
| 382 | 842 | 615 | 1233 |
| 444 | 886 | 686 | 1248 |
| 586 | 863 | 743 | 1275 |
| 664 | 847 | 824 | 1298 |
| 769 | 822 | | |
| 818 | 800 | | |

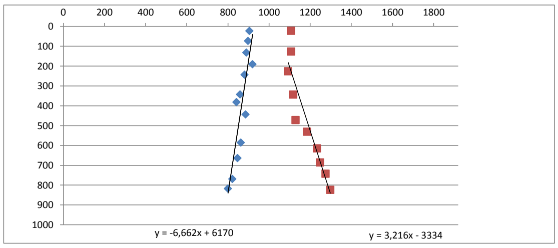


Angle 25,81

| R5_t100 | | | |
|---|---|---|---|
| Left | | Right | |
| Row | Column | Row | Column |
| 13 | 834 | 10 | 1074 |
| 96 | 828 | 67 | 1077 |
| 126 | 824 | 137 | 1107 |
| 228 | 825 | 231 | 1123 |
| 281 | 841 | 294 | 1137 |
| 340 | 799 | 378 | 1130 |
| 409 | 800 | 443 | 1110 |
| 472 | 760 | 539 | 1134 |
| 585 | 763 | 597 | 1151 |
| 647 | 724 | 666 | 1214 |
| 699 | 686 | 740 | 1214 |
| 780 | 679 | 796 | 1192 |

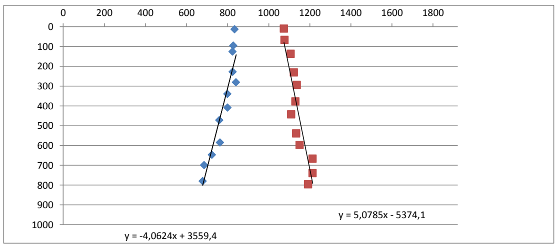


Angle 24,97

**Measurments 1-5 with concentration**

| | measurements | |
|---|---|---|
| mean angle | 5 | 26,36 |
| st dev | 5 | 0,75 |

Figure F.1: Measured angles for the Round nozzle shape

| REC20_1_t100 | | | |
|---|---|---|---|
| Left | | Right | |
| Row | Column | Row | Column |
| 10 | 869 | 23 | 1193 |
| 91 | 846 | 68 | 1216 |
| 182 | 892 | 141 | 1220 |
| 233 | 822 | 192 | 1209 |
| 298 | 833 | 282 | 1218 |
| 368 | 795 | 338 | 1262 |
| 472 | 803 | 426 | 1252 |
| 538 | 822 | 484 | 1281 |
| 616 | 803 | 575 | 1282 |
| 695 | 803 | 641 | 1271 |
| 774 | 764 | 772 | 1283 |
| 835 | 736 | 841 | 1314 |
| | | | |
| | | | |

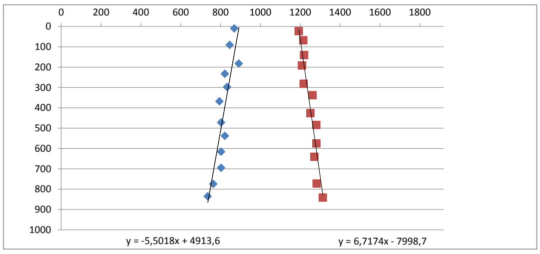


Angle 18,77

| REC20_2_t100 | | | |
|---|---|---|---|
| Left | | Right | |
| Row | Column | Row | Column |
| 7 | 928 | 7 | 1127 |
| 66 | 895 | 89 | 1131 |
| 149 | 887 | 183 | 1142 |
| 211 | 867 | 224 | 1132 |
| 293 | 887 | 259 | 1148 |
| 369 | 938 | 331 | 1131 |
| 397 | 882 | 444 | 1111 |
| 446 | 870 | 548 | 1126 |
| 534 | 840 | 578 | 1204 |
| 642 | 816 | 560 | 1236 |
| 720 | 788 | 706 | 1230 |
| 772 | 804 | 764 | 1202 |
| 831 | 758 | 834 | 1203 |
| 888 | 764 | 896 | 1199 |

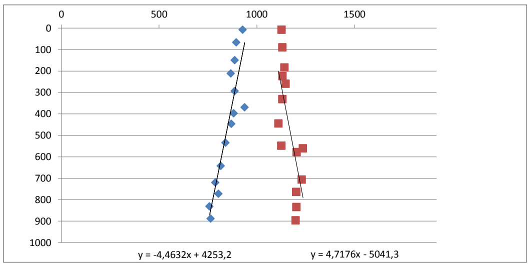


Angle 24,6

| REC20_3_t100 | | | |
|---|---|---|---|
| Left | | Right | |
| Row | Column | Row | Column |
| 8 | 835 | 8 | 1057 |
| 68 | 863 | 87 | 1085 |
| 154 | 848 | 182 | 1082 |
| 215 | 824 | 266 | 1032 |
| 263 | 763 | 374 | 1051 |
| 323 | 746 | 419 | 1101 |
| 387 | 784 | 491 | 1101 |
| 437 | 804 | 560 | 1119 |
| 490 | 748 | 625 | 1080 |
| 574 | 744 | 690 | 1113 |
| 670 | 759 | 745 | 1145 |
| 743 | 706 | 832 | 1167 |
| 816 | 676 | 885 | 1148 |
| | | 915 | 1095 |
| | | | |

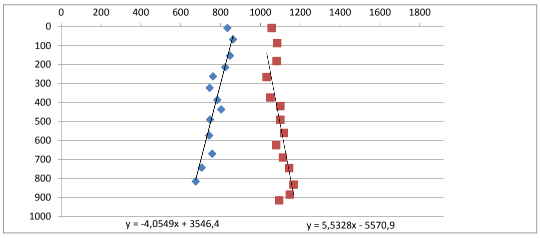


Angle 24,1

| REC20_4_t100 | | | |
|---|---|---|---|
| Left | | Right | |
| Row | Column | Row | Column |
| 10 | 876 | 6 | 1107 |
| 97 | 870 | 67 | 1111 |
| 157 | 900 | 139 | 1134 |
| 212 | 843 | 197 | 1164 |
| 296 | 820 | 292 | 1187 |
| 350 | 864 | 368 | 1205 |
| 462 | 866 | 422 | 1220 |
| 556 | 850 | 506 | 1195 |
| 627 | 843 | 548 | 1133 |
| 684 | 817 | 633 | 1172 |
| 769 | 822 | 754 | 1193 |
| 854 | 806 | 855 | 1223 |
| | | | |
| | | | |

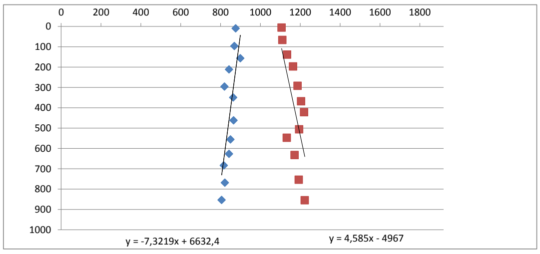


Angle 20,08

| REC20_5_t100 | | | |
|---|---|---|---|
| Left | | Right | |
| Row | Column | Row | Column |
| 11 | 928 | 12 | 1201 |
| 74 | 937 | 83 | 1149 |
| 104 | 903 | 153 | 1160 |
| 179 | 895 | 169 | 1188 |
| 221 | 868 | 247 | 1178 |
| 289 | 863 | 273 | 1219 |
| 367 | 843 | 318 | 1235 |
| 423 | 862 | 440 | 1242 |
| 484 | 853 | 500 | 1279 |
| 548 | 868 | 593 | 1271 |
| 634 | 870 | 688 | 1270 |
| 692 | 859 | 794 | 1282 |
| 775 | 844 | 855 | 1285 |
| 814 | 795 | | |
| 853 | 788 | | |

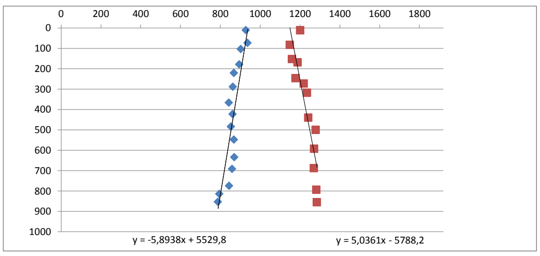


Angle 20,86

**Measurments 1-5 with concentration**
**Measurments 6-10 angle only**

Figure F.2: Measured angles for the Rectangular 20x3.9 - 3.9 nozzle shape (experiments 1-5)

| REC20_6_t100 | | | |
|---|---|---|---|
| Left | | Right | |
| Row | Column | Row | Column |
| 16 | 917 | 14 | 1121 |
| 106 | 907 | 63 | 1151 |
| 211 | 899 | 137 | 1170 |
| 299 | 890 | 218 | 1193 |
| 341 | 849 | 343 | 1200 |
| 412 | 858 | 375 | 1255 |
| 487 | 828 | 488 | 1268 |
| 576 | 837 | 562 | 1239 |
| 642 | 831 | 643 | 1249 |
| 785 | 802 | 764 | 1280 |

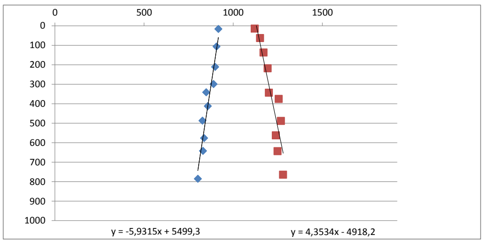


Angle 22,51

| REC20_7_t100 | | | |
|---|---|---|---|
| Left | | Right | |
| Row | Column | Row | Column |
| 10 | 905 | 24 | 1118 |
| 100 | 902 | 94 | 1134 |
| 167 | 902 | 138 | 1154 |
| 241 | 884 | 236 | 1173 |
| 292 | 857 | 323 | 1157 |
| 407 | 867 | 388 | 1169 |
| 535 | 896 | 448 | 1176 |
| 590 | 842 | 553 | 1158 |
| 634 | 842 | 628 | 1228 |
| 718 | 871 | 725 | 1240 |
| 815 | 892 | 809 | 1276 |
| 886 | 879 | 864 | 1308 |
| 966 | 820 | 897 | 1320 |

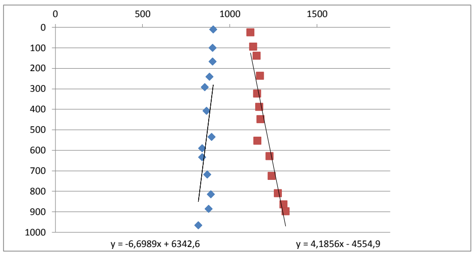


Angle 21,93

| REC20_8_t100 | | | |
|---|---|---|---|
| Left | | Right | |
| Row | Column | Row | Column |
| 10 | 776 | 11 | 988 |
| 67 | 758 | 86 | 1010 |
| 140 | 774 | 183 | 1021 |
| 240 | 733 | 262 | 1037 |
| 332 | 712 | 338 | 1010 |
| 441 | 699 | 415 | 973 |
| 544 | 651 | 465 | 1028 |
| 645 | 637 | 536 | 1046 |
| 760 | 615 | 558 | 1074 |
| 833 | 611 | 686 | 1080 |
| 889 | 608 | 778 | 1120 |
| | | 835 | 1118 |
| | | 894 | 1120 |

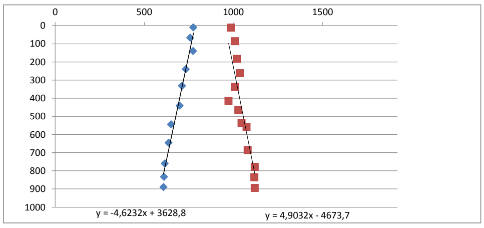


Angle 23,73

| REC20_9_t100 | | | |
|---|---|---|---|
| Left | | Right | |
| Row | Column | Row | Column |
| 7 | 877 | 10 | 1093 |
| 68 | 869 | 90 | 1096 |
| 146 | 884 | 168 | 1096 |
| 205 | 884 | 251 | 1113 |
| 274 | 855 | 333 | 1148 |
| 324 | 838 | 423 | 1125 |
| 415 | 861 | 488 | 1091 |
| 484 | 811 | 564 | 1128 |
| 597 | 830 | 595 | 1170 |
| 654 | 793 | 687 | 1206 |
| 764 | 868 | 781 | 1186 |
| 911 | 831 | 888 | 1135 |

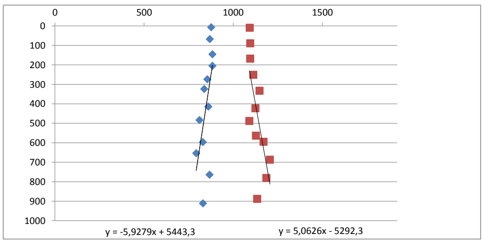


Angle 20,75

| REC20_10_t100 | | | |
|---|---|---|---|
| Left | | Right | |
| Row | Column | Row | Column |
| 5 | 938 | 11 | 1127 |
| 37 | 949 | 86 | 1133 |
| 103 | 922 | 185 | 1161 |
| 155 | 882 | 157 | 1178 |
| 248 | 878 | 331 | 1140 |
| 295 | 907 | 401 | 1193 |
| 390 | 906 | 405 | 1278 |
| 483 | 903 | 490 | 1270 |
| 547 | 912 | 576 | 1250 |
| 657 | 910 | 669 | 1237 |
| 703 | 846 | 737 | 1277 |
| 765 | 851 | 815 | 1283 |
| 797 | 824 | 903 | 1304 |
| 863 | 862 | | |
| 906 | 850 | | |

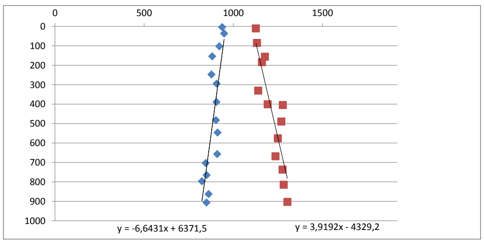


Angle 22,87

| | measurements | |
|---|---|---|
| mean angle | 5 | 21,68 |
| st dev | 5 | 1,02 |
| mean angle | 10 | 22,02 |
| st dev | 10 | 0,58 |

Figure F.3: Measured angles for the Rectangular 20x3.9 - 3.9 nozzle shape (experiments 6-10)

| REC20_11_t100 | | | |
|---|---|---|---|
| Left | | Right | |
| Row | Column | Row | Column |
| 7 | 882 | 9 | 1114 |
| 68 | 889 | 88 | 1132 |
| 120 | 834 | 150 | 1161 |
| 178 | 816 | 218 | 1175 |
| 239 | 858 | 257 | 1195 |
| 291 | 907 | 342 | 1178 |
| 375 | 908 | 390 | 1214 |
| 432 | 857 | 472 | 1201 |
| 493 | 831 | 505 | 1244 |
| 578 | 925 | 559 | 1220 |
| 679 | 801 | 625 | 1232 |
| 760 | 816 | 697 | 1198 |
| 821 | 771 | 782 | 1232 |
| 883 | 759 | 883 | 1256 |

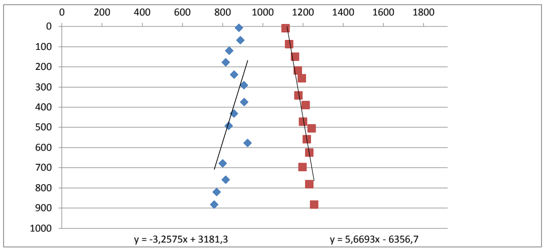


Angle 27,07

| REC20_12_t100 | | | |
|---|---|---|---|
| Left | | Right | |
| Row | Column | Row | Column |
| 11 | 907 | 17 | 1059 |
| 63 | 887 | 87 | 1091 |
| 140 | 888 | 179 | 1104 |
| 213 | 872 | 238 | 1122 |
| 282 | 853 | 282 | 1142 |
| 348 | 851 | 367 | 1159 |
| 393 | 821 | 470 | 1182 |
| 461 | 830 | 542 | 1120 |
| 521 | 837 | 612 | 1186 |
| 586 | 829 | 701 | 1200 |
| 667 | 840 | 774 | 1242 |
| 745 | 844 | 865 | 1223 |
| 786 | 761 | 927 | 1213 |
| 881 | 745 | | |

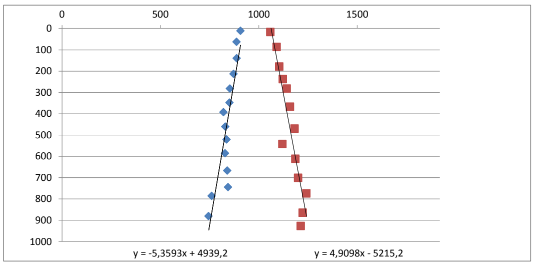


Angle 22,08

| REC20_13_t100 | | | |
|---|---|---|---|
| Left | | Right | |
| Row | Column | Row | Column |
| 16 | 909 | 17 | 1060 |
| 73 | 889 | 92 | 1090 |
| 160 | 888 | 184 | 1105 |
| 215 | 875 | 248 | 1126 |
| 292 | 850 | 300 | 1144 |
| 361 | 845 | 374 | 1168 |
| 404 | 819 | 413 | 1190 |
| 473 | 831 | 489 | 1179 |
| 579 | 825 | 556 | 1120 |
| 679 | 838 | 617 | 1189 |
| 781 | 843 | 820 | 1200 |
| 804 | 801 | 775 | 1247 |
| 874 | 790 | 877 | 1219 |

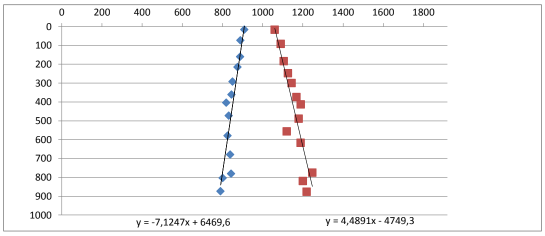


Angle 20,55

| REC20_14_t100 | | | |
|---|---|---|---|
| Left | | Right | |
| Row | Column | Row | Column |
| 6 | 891 | 7 | 1137 |
| 79 | 920 | 49 | 1215 |
| 128 | 883 | 138 | 1198 |
| 199 | 870 | 215 | 1145 |
| 221 | 851 | 325 | 1142 |
| 338 | 882 | 410 | 1244 |
| 394 | 863 | 513 | 1232 |
| 451 | 823 | 566 | 1251 |
| 495 | 817 | 654 | 1209 |
| 628 | 782 | 738 | 1243 |
| 704 | 796 | 839 | 1257 |
| 765 | 775 | | |
| 834 | 735 | | |

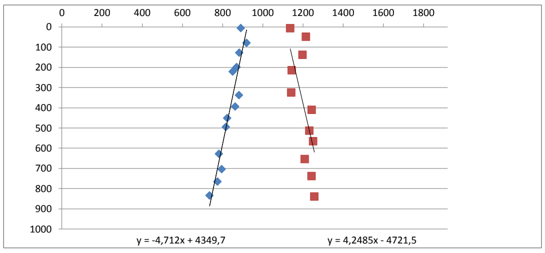


Angle 25,23

| REC20_15_t100 | | | |
|---|---|---|---|
| Left | | Right | |
| Row | Column | Row | Column |
| 6 | 889 | 7 | 1094 |
| 65 | 874 | 51 | 1116 |
| 124 | 914 | 74 | 1171 |
| 232 | 891 | 142 | 1157 |
| 343 | 862 | 267 | 1121 |
| 402 | 847 | 291 | 1173 |
| 459 | 805 | 373 | 1170 |
| 543 | 837 | 433 | 1148 |
| 612 | 865 | 456 | 1200 |
| 704 | 844 | 540 | 1235 |
| 800 | 849 | 612 | 1312 |
| | | 680 | 1276 |
| | | 794 | 1274 |

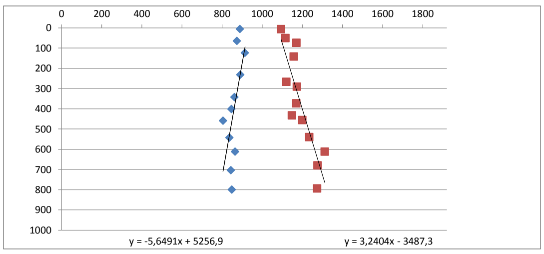


Angle 27,19

**Only angle measurements**

Figure F.4: Measured angles for the Rectangular 20x3.9 - 20 nozzle shape (experiments 11-15)

| REC20_16_t100 | | | |
|---|---|---|---|
| Left | | Right | |
| Row | Column | Row | Column |
| 16 | 909 | 12 | 1085 |
| 58 | 897 | 63 | 1110 |
| 112 | 896 | 98 | 1133 |
| 174 | 886 | 162 | 1166 |
| 230 | 903 | 187 | 1201 |
| 285 | 888 | 265 | 1201 |
| 379 | 866 | 341 | 1192 |
| 457 | 876 | 425 | 1207 |
| 520 | 889 | 487 | 1183 |
| 605 | 882 | 540 | 1154 |
| 661 | 825 | 603 | 1211 |
| 712 | 784 | 694 | 1215 |
| 755 | 819 | 710 | 1286 |
| 795 | 857 | 795 | 1299 |

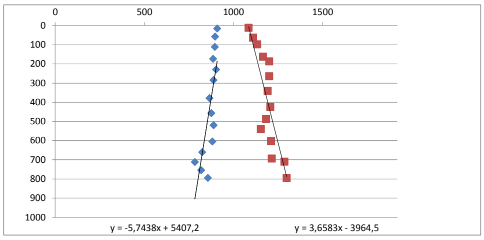


Angle 25,16

| REC20_17_t100 | | | |
|---|---|---|---|
| Left | | Right | |
| Row | Column | Row | Column |
| 10 | 935 | 17 | 1144 |
| 73 | 921 | 53 | 1154 |
| 139 | 881 | 89 | 1141 |
| 212 | 892 | 147 | 1170 |
| 274 | 882 | 189 | 1195 |
| 352 | 870 | 270 | 1208 |
| 388 | 838 | 338 | 1237 |
| 478 | 913 | 397 | 1219 |
| 539 | 850 | 486 | 1209 |
| 648 | 861 | 514 | 1246 |
| 724 | 843 | 580 | 1277 |
| 841 | 801 | 641 | 1256 |
| | | 715 | 1256 |
| | | 830 | 1265 |

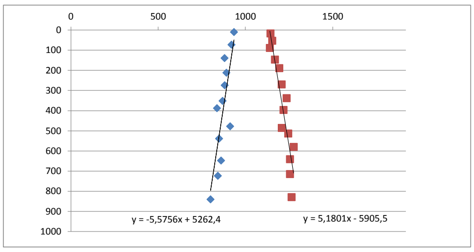


Angle 21,09

| REC20_18_t100 | | | |
|---|---|---|---|
| Left | | Right | |
| Row | Column | Row | Column |
| 6 | 885 | 7 | 1157 |
| 76 | 907 | 62 | 1172 |
| 123 | 873 | 98 | 1212 |
| 206 | 881 | 188 | 1218 |
| 268 | 856 | 270 | 1212 |
| 316 | 842 | 331 | 1238 |
| 382 | 874 | 387 | 1272 |
| 477 | 851 | 470 | 1291 |
| 541 | 884 | 529 | 1275 |
| 670 | 834 | 604 | 1320 |
| 735 | 803 | 665 | 1424 |
| 825 | 812 | 770 | 1430 |
| | | 885 | 1440 |
| | | | |
| | | | |

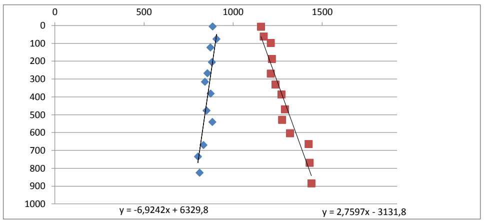


Angle 28,14

| REC20_19_t100 | | | |
|---|---|---|---|
| Left | | Right | |
| Row | Column | Row | Column |
| 12 | 930 | 10 | 1084 |
| 42 | 864 | 80 | 1094 |
| 87 | 864 | 134 | 1084 |
| 152 | 879 | 193 | 1106 |
| 264 | 875 | 249 | 1126 |
| 343 | 874 | 306 | 1152 |
| 428 | 861 | 389 | 1139 |
| 529 | 851 | 435 | 1159 |
| 604 | 883 | 510 | 1154 |
| 675 | 870 | 618 | 1159 |
| 734 | 845 | 654 | 1235 |
| 793 | 834 | 768 | 1247 |
| 871 | 803 | 845 | 1276 |
| | | | |

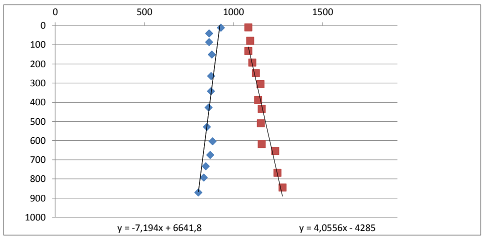


Angle 21,77

| REC20_20_t100 | | | |
|---|---|---|---|
| Left | | Right | |
| Row | Column | Row | Column |
| 15 | 870 | 5 | 1055 |
| 90 | 866 | 82 | 1074 |
| 179 | 846 | 146 | 1077 |
| 245 | 864 | 214 | 1078 |
| 302 | 847 | 298 | 1086 |
| 360 | 868 | 366 | 1100 |
| 411 | 891 | 447 | 1089 |
| 480 | 863 | 522 | 1111 |
| 527 | 841 | 592 | 1155 |
| 569 | 804 | 664 | 1146 |
| 616 | 770 | 754 | 1168 |
| 676 | 726 | 857 | 1183 |
| 797 | 817 | 940 | 1200 |
| 921 | 808 | 947 | 1230 |
| 973 | 749 | | |

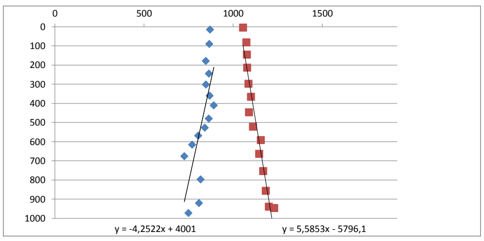


Angle 23,39

| | measurements | |
|---|---|---|
| mean angle | 5 | 24,42 |
| st dev | 5 | 1,20 |
| mean angle | 10 | 24,17 |
| st dev | 10 | 0,83 |

Figure F.5: Measured angles for the Rectangular 20x3.9 - 20 nozzle shape (experiments 16-20)

| REC30_1_t100 | | | |
|---|---|---|---|
| Left | | Right | |
| Row | Column | Row | Column |
| 9 | 951 | 8 | 1162 |
| 58 | 927 | 80 | 1162 |
| 101 | 887 | 145 | 1174 |
| 188 | 905 | 210 | 1158 |
| 270 | 896 | 287 | 1152 |
| 356 | 921 | 316 | 1194 |
| 384 | 953 | 388 | 1213 |
| 439 | 902 | 463 | 1196 |
| 499 | 860 | 540 | 1215 |
| 586 | 866 | 590 | 1280 |
| 645 | 861 | 693 | 1261 |
| 734 | 853 | 753 | 1257 |
| 808 | 859 | 834 | 1318 |
| 836 | 826 | | |

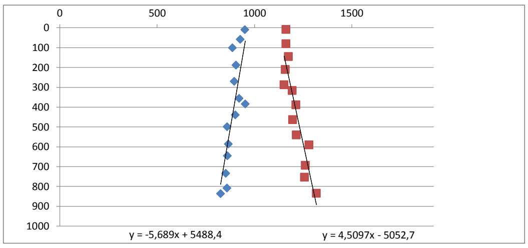


Angle 22,47

| REC30_2_t100 | | | |
|---|---|---|---|
| Left | | Right | |
| Row | Column | Row | Column |
| 7 | 862 | 11 | 1077 |
| 50 | 860 | 70 | 1100 |
| 93 | 855 | 147 | 1145 |
| 171 | 853 | 241 | 1151 |
| 244 | 896 | 383 | 1155 |
| 303 | 863 | 482 | 1145 |
| 392 | 854 | 543 | 1179 |
| 477 | 838 | 587 | 1210 |
| 578 | 813 | 688 | 1231 |
| 650 | 790 | 791 | 1220 |
| 734 | 771 | 861 | 1231 |
| 808 | 728 | | |
| 863 | 704 | | |
| | | | |
| | | | |

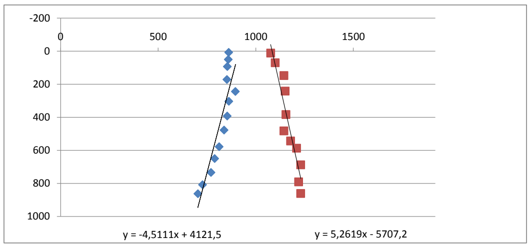


Angle 23,26

| REC30_3_t100 | | | |
|---|---|---|---|
| Left | | Right | |
| Row | Column | Row | Column |
| 11 | 822 | 6 | 1075 |
| 54 | 831 | 53 | 1098 |
| 104 | 851 | 119 | 1136 |
| 149 | 814 | 193 | 1131 |
| 222 | 818 | 254 | 1092 |
| 274 | 803 | 332 | 1100 |
| 349 | 792 | 365 | 1148 |
| 416 | 780 | 463 | 1141 |
| 533 | 767 | 511 | 1114 |
| 626 | 796 | 559 | 1167 |
| 698 | 808 | 620 | 1136 |
| 753 | 833 | 705 | 1138 |
| 810 | 803 | 779 | 1148 |
| 858 | 747 | 837 | 1125 |
| 892 | 731 | 898 | 1175 |

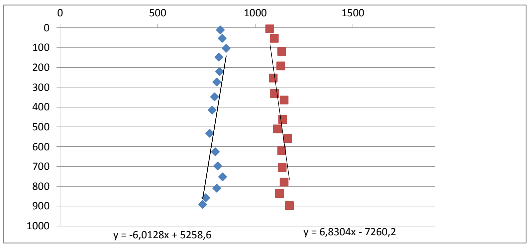


Angle 17,77

| REC30_4_t100 | | | |
|---|---|---|---|
| Left | | Right | |
| Row | Column | Row | Column |
| 6 | 876 | 10 | 1065 |
| 60 | 866 | 70 | 1096 |
| 150 | 854 | 145 | 1115 |
| 208 | 829 | 239 | 1151 |
| 260 | 832 | 328 | 1132 |
| 320 | 854 | 393 | 1086 |
| 381 | 806 | 473 | 1113 |
| 457 | 823 | 557 | 1138 |
| 530 | 788 | 627 | 1156 |
| 585 | 751 | 698 | 1210 |
| 723 | 754 | 786 | 1245 |
| 765 | 785 | 844 | 1239 |
| 819 | 817 | 890 | 1210 |
| 894 | 795 | | |

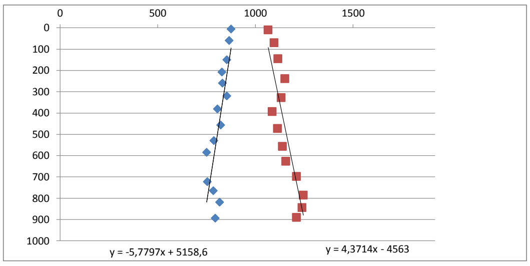


Angle 22,7

| REC30_5_t100 | | | |
|---|---|---|---|
| Left | | Right | |
| Row | Column | Row | Column |
| 7 | 780 | 6 | 1105 |
| 53 | 746 | 48 | 1123 |
| 98 | 728 | 128 | 1096 |
| 144 | 765 | 244 | 1098 |
| 241 | 767 | 303 | 1149 |
| 335 | 755 | 420 | 1153 |
| 407 | 792 | 505 | 1191 |
| 494 | 762 | 602 | 1203 |
| 558 | 738 | 693 | 1165 |
| 614 | 712 | 735 | 1188 |
| 692 | 677 | 763 | 1214 |
| 775 | 711 | 821 | 1206 |
| 811 | 751 | 886 | 1226 |
| 875 | 718 | | |

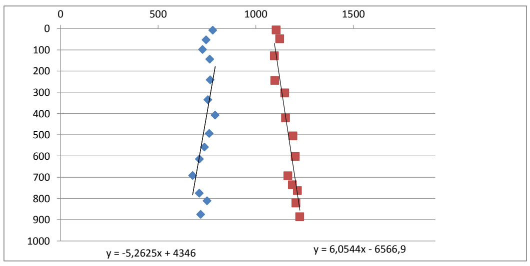


Angle 20,14

**Measurments 1-5 with concentration**
**Measurments 6-10 angle only**

Figure F.6: Measured angles for the Rectangular 30x2.6 - 2.6 nozzle shape (experiments 1-5)

**REC30_6_t100**

| Left | | Right | |
|---|---|---|---|
| Row | Column | Row | Column |
| 7 | 847 | 9 | 1104 |
| 41 | 835 | 66 | 1123 |
| 119 | 884 | 129 | 1112 |
| 214 | 879 | 189 | 1132 |
| 300 | 895 | 271 | 1136 |
| 394 | 866 | 358 | 1142 |
| 464 | 837 | 477 | 1169 |
| 542 | 806 | 558 | 1192 |
| 634 | 790 | 615 | 1224 |
| 706 | 773 | 686 | 1190 |
| 749 | 796 | 743 | 1244 |
| 795 | 822 | 821 | 1277 |
| 868 | 790 | 882 | 1303 |
| 891 | 760 | | |

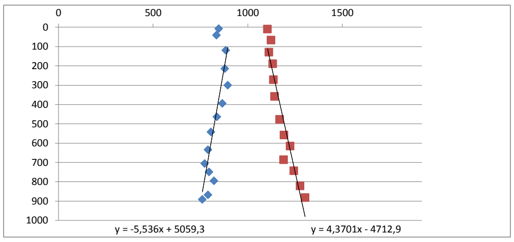


Angle 23,13

**REC30_7_t100**

| Left | | Right | |
|---|---|---|---|
| Row | Column | Row | Column |
| 7 | 915 | 10 | 1084 |
| 54 | 916 | 45 | 1111 |
| 99 | 929 | 119 | 1116 |
| 176 | 930 | 156 | 1136 |
| 283 | 898 | 241 | 1149 |
| 349 | 865 | 339 | 1168 |
| 426 | 875 | 413 | 1179 |
| 501 | 861 | 489 | 1193 |
| 574 | 849 | 565 | 1169 |
| 608 | 804 | 641 | 1183 |
| 682 | 829 | 742 | 1198 |
| 739 | 865 | 814 | 1222 |
| 841 | 875 | 872 | 1270 |
| 910 | 861 | | |
| 962 | 804 | | |

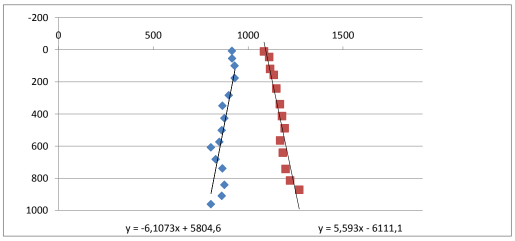


Angle 19,44

**REC30_8_t100**

| Left | | Right | |
|---|---|---|---|
| Row | Column | Row | Column |
| 12 | 885 | 12 | 1121 |
| 72 | 927 | 99 | 1130 |
| 156 | 919 | 165 | 1147 |
| 221 | 887 | 245 | 1173 |
| 297 | 909 | 302 | 1201 |
| 348 | 925 | 372 | 1220 |
| 406 | 936 | 431 | 1208 |
| 474 | 886 | 474 | 1247 |
| 530 | 871 | 561 | 1236 |
| 589 | 851 | 623 | 1271 |
| 701 | 843 | 701 | 1292 |
| 757 | 814 | 761 | 1285 |
| 811 | 839 | 825 | 1320 |
| 910 | 857 | 912 | 1318 |

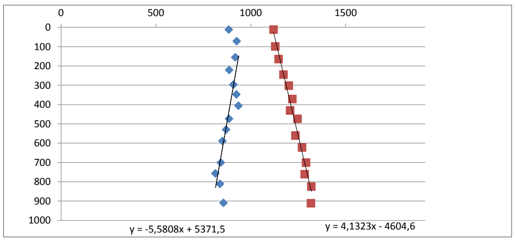


Angle 23,76

**REC30_9_t100**

| Left | | Right | |
|---|---|---|---|
| Row | Column | Row | Column |
| 6 | 858 | 7 | 1112 |
| 50 | 848 | 43 | 1130 |
| 106 | 881 | 95 | 1109 |
| 181 | 860 | 198 | 1131 |
| 227 | 840 | 254 | 1135 |
| 302 | 855 | 293 | 1180 |
| 391 | 830 | 416 | 1189 |
| 476 | 825 | 469 | 1210 |
| 571 | 780 | 573 | 1225 |
| 646 | 793 | 672 | 1243 |
| 764 | 759 | 746 | 1258 |
| 802 | 740 | 780 | 1235 |
| 871 | 738 | 845 | 1234 |

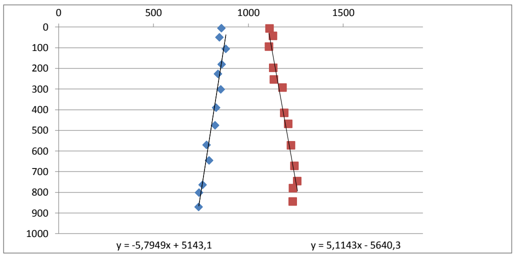


Angle 20,85

**REC30_10_t100**

| Left | | Right | |
|---|---|---|---|
| Row | Column | Row | Column |
| 6 | 920 | 9 | 1205 |
| 56 | 901 | 72 | 1251 |
| 131 | 900 | 154 | 1266 |
| 216 | 904 | 245 | 1242 |
| 276 | 877 | 359 | 1238 |
| 362 | 903 | 439 | 1292 |
| 416 | 877 | 546 | 1300 |
| 495 | 854 | 636 | 1330 |
| 572 | 833 | 710 | 1349 |
| 645 | 863 | 753 | 1375 |
| 681 | 909 | 824 | 1331 |
| 756 | 845 | | |
| 814 | 867 | | |

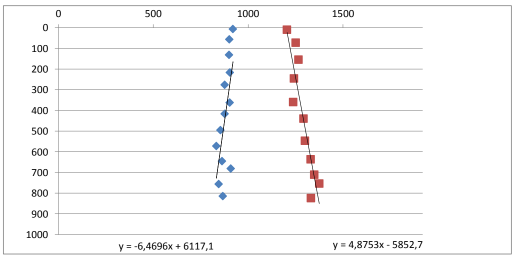


Angle 20,38

| | measurements | |
|---|---|---|
| mean angle | 5 | 21,27 |
| st dev | 5 | 0,92 |
| mean angle | 10 | 21,39 |
| st dev | 10 | 0,59 |

Figure F.7: Measured angles for the Rectangular 30x2.6 - 2.6 nozzle shape (experiments 6-10)

| REC30_11_t100 | | | |
|---|---|---|---|
| Left | | Right | |
| Row | Column | Row | Column |
| 7 | 862 | 8 | 1118 |
| 84 | 859 | 40 | 1130 |
| 152 | 841 | 95 | 1112 |
| 218 | 832 | 182 | 1128 |
| 290 | 799 | 262 | 1144 |
| 347 | 820 | 312 | 1165 |
| 390 | 849 | 396 | 1200 |
| 467 | 840 | 455 | 1211 |
| 580 | 831 | 546 | 1197 |
| 649 | 833 | 618 | 1231 |
| 713 | 811 | 701 | 1263 |
| 767 | 786 | 789 | 1242 |
| 814 | 774 | 859 | 1231 |
| 895 | 737 | 902 | 1257 |

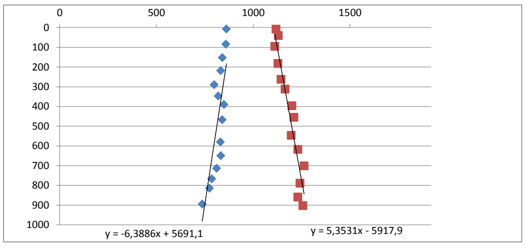


Angle 19,48

| REC30_12_t100 | | | |
|---|---|---|---|
| Left | | Right | |
| Row | Column | Row | Column |
| 10 | 858 | 9 | 1107 |
| 75 | 880 | 75 | 1112 |
| 160 | 894 | 159 | 1130 |
| 241 | 879 | 210 | 1112 |
| 295 | 858 | 255 | 1148 |
| 378 | 825 | 363 | 1163 |
| 440 | 861 | 440 | 1131 |
| 494 | 820 | 494 | 1182 |
| 571 | 849 | 566 | 1196 |
| 638 | 869 | 636 | 1232 |
| 741 | 812 | 744 | 1235 |
| 826 | 806 | 849 | 1245 |
| 889 | 773 | | |
| | | | |

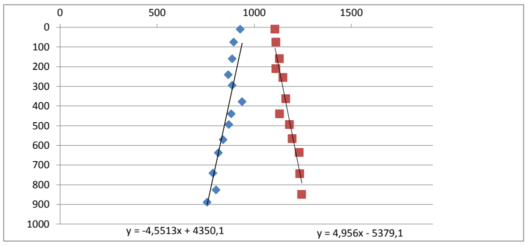


Angle 23,8

| REC30_13_t100 | | | |
|---|---|---|---|
| Left | | Right | |
| Row | Column | Row | Column |
| 4 | 790 | 7 | 1051 |
| 63 | 823 | 91 | 1062 |
| 128 | 803 | 148 | 1044 |
| 176 | 766 | 209 | 1059 |
| 243 | 774 | 268 | 1082 |
| 302 | 744 | 318 | 1124 |
| 366 | 793 | 402 | 1147 |
| 459 | 772 | 473 | 1118 |
| 541 | 751 | 545 | 1150 |
| 635 | 724 | 603 | 1179 |
| 742 | 740 | 674 | 1225 |
| 833 | 767 | 760 | 1231 |
| 877 | 732 | 831 | 1221 |
| | | | |
| | | | |

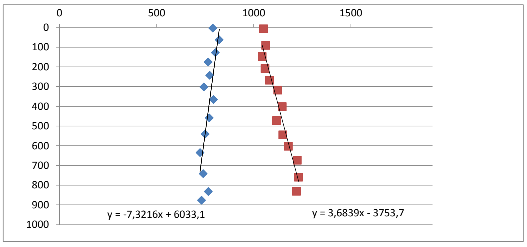


Angle 22,96

| REC30_14_t100 | | | |
|---|---|---|---|
| Left | | Right | |
| Row | Column | Row | Column |
| 10 | 854 | 7 | 1047 |
| 56 | 830 | 60 | 1072 |
| 136 | 821 | 145 | 1069 |
| 210 | 825 | 236 | 1078 |
| 286 | 806 | 322 | 1097 |
| 349 | 822 | 411 | 1117 |
| 414 | 835 | 496 | 1105 |
| 497 | 831 | 580 | 1104 |
| 560 | 752 | 642 | 1149 |
| 641 | 775 | 708 | 1172 |
| 691 | 807 | 781 | 1163 |
| 758 | 770 | 852 | 1197 |
| 815 | 770 | | |
| 856 | 728 | | |

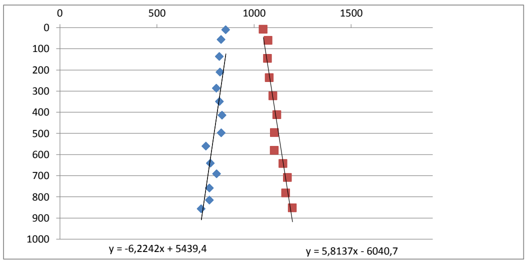


Angle 18,89

| REC30_15_t100 | | | |
|---|---|---|---|
| Left | | Right | |
| Row | Column | Row | Column |
| 9 | 821 | 7 | 1066 |
| 60 | 786 | 47 | 1091 |
| 144 | 766 | 103 | 1074 |
| 195 | 809 | 199 | 1092 |
| 280 | 828 | 291 | 1107 |
| 361 | 813 | 342 | 1155 |
| 421 | 796 | 402 | 1186 |
| 484 | 776 | 473 | 1171 |
| 580 | 759 | 518 | 1137 |
| 666 | 738 | 605 | 1155 |
| 745 | 683 | 651 | 1195 |
| 840 | 672 | 671 | 1166 |
| | | 774 | 1189 |
| | | 853 | 1207 |

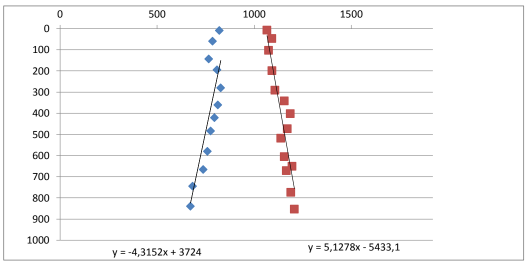


Angle 24,08

**Measurments 1-5 with concentration**
**Measurments 6-10 angle only**

Figure F.8: Measured angles for the Rectangular 30x2.6 - 30) nozzle shape (experiments 11-15)

| REC30_16_t100 | | | |
|---|---|---|---|
| Left | | Right | |
| Row | Column | Row | Column |
| 7 | 817 | 9 | 1048 |
| 53 | 839 | 86 | 1049 |
| 131 | 835 | 156 | 1063 |
| 196 | 808 | 229 | 1092 |
| 267 | 797 | 289 | 1101 |
| 334 | 825 | 359 | 1127 |
| 404 | 829 | 409 | 1139 |
| 464 | 823 | 495 | 1138 |
| 529 | 792 | 569 | 1159 |
| 608 | 776 | 644 | 1128 |
| 667 | 750 | 693 | 1230 |
| 750 | 771 | 781 | 1213 |
| 830 | 774 | 840 | 1195 |
| 915 | 761 | 927 | 1195 |

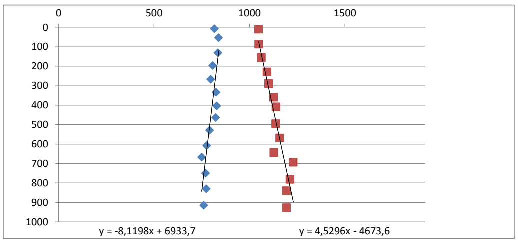


Angle 19,47

| REC30_17_t100 | | | |
|---|---|---|---|
| Left | | Right | |
| Row | Column | Row | Column |
| 5 | 840 | 7 | 1073 |
| 33 | 822 | 87 | 1077 |
| 93 | 860 | 132 | 1090 |
| 165 | 844 | 221 | 1083 |
| 200 | 830 | 292 | 1104 |
| 262 | 853 | 374 | 1090 |
| 359 | 870 | 459 | 1089 |
| 419 | 833 | 529 | 1115 |
| 488 | 857 | 574 | 1157 |
| 559 | 827 | 670 | 1167 |
| 622 | 829 | 752 | 1151 |
| 731 | 825 | 811 | 1194 |
| 814 | 823 | 872 | 1168 |
| 847 | 763 | 909 | 1221 |

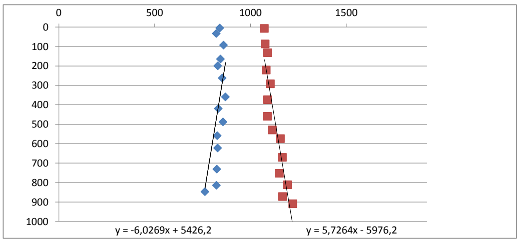


Angle 19,33

| REC30_18_t100 | | | |
|---|---|---|---|
| Left | | Right | |
| Row | Column | Row | Column |
| 17 | 848 | 9 | 1107 |
| 87 | 849 | 65 | 1123 |
| 154 | 820 | 125 | 1107 |
| 214 | 780 | 209 | 1111 |
| 281 | 771 | 316 | 1132 |
| 374 | 797 | 376 | 1158 |
| 441 | 813 | 418 | 1229 |
| 500 | 817 | 516 | 1207 |
| 567 | 785 | 595 | 1253 |
| 665 | 789 | 674 | 1278 |
| 737 | 793 | 728 | 1238 |
| 784 | 778 | 776 | 1276 |
| 866 | 786 | 855 | 1254 |
| 916 | 767 | 902 | 1299 |
| 966 | 748 | 943 | 1324 |

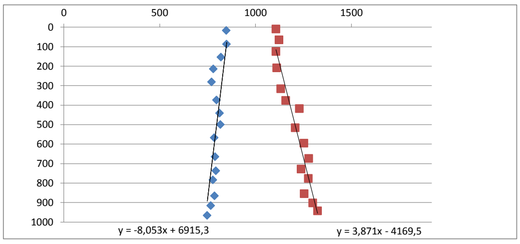


Angle 21,56

| REC30_19_t100 | | | |
|---|---|---|---|
| Left | | Right | |
| Row | Column | Row | Column |
| 5 | 822 | 9 | 1056 |
| 75 | 828 | 76 | 1068 |
| 133 | 813 | 104 | 1107 |
| 218 | 796 | 179 | 1087 |
| 294 | 789 | 256 | 1086 |
| 358 | 830 | 288 | 1157 |
| 419 | 802 | 386 | 1187 |
| 493 | 777 | 465 | 1142 |
| 574 | 778 | 548 | 1173 |
| 636 | 701 | 606 | 1194 |
| 735 | 734 | 684 | 1202 |
| 776 | 787 | 765 | 1173 |
| 840 | 746 | 821 | 1229 |
| 895 | 700 | 875 | 1244 |

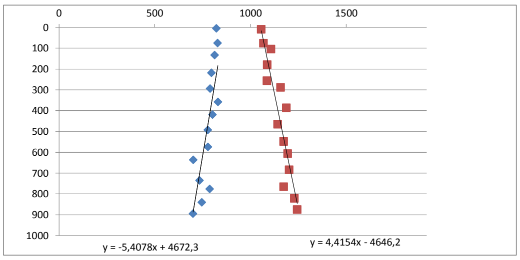


Angle 23,24

| REC30_20_t100 | | | |
|---|---|---|---|
| Left | | Right | |
| Row | Column | Row | Column |
| 6 | 792 | 9 | 1061 |
| 40 | 788 | 91 | 1080 |
| 98 | 801 | 146 | 1095 |
| 172 | 777 | 228 | 1090 |
| 248 | 801 | 312 | 1100 |
| 295 | 737 | 372 | 1135 |
| 355 | 714 | 409 | 1175 |
| 464 | 736 | 513 | 1158 |
| 525 | 774 | 593 | 1148 |
| 622 | 789 | 668 | 1166 |
| 702 | 767 | 726 | 1181 |
| 767 | 732 | 794 | 1184 |
| 815 | 718 | 871 | 1205 |
| 855 | 707 | 929 | 1234 |

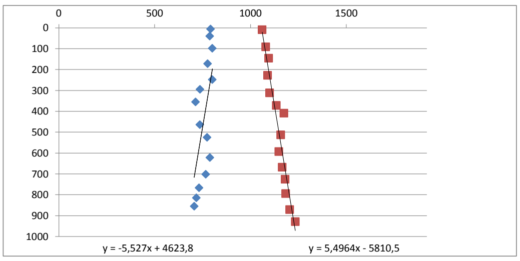


Angle 20,58

| | measurements | |
|---|---|---|
| mean angle | 5 | 21,84 |
| st dev | 5 | 0,99 |
| mean angle | 10 | 21,34 |
| st dev | 10 | 0,61 |

Figure F.9: Measured angles for the Rectangular 30x2.6 - 30) nozzle shape (experiments 16-20)

# G

# Snapshots used for angle measurements at T=100s

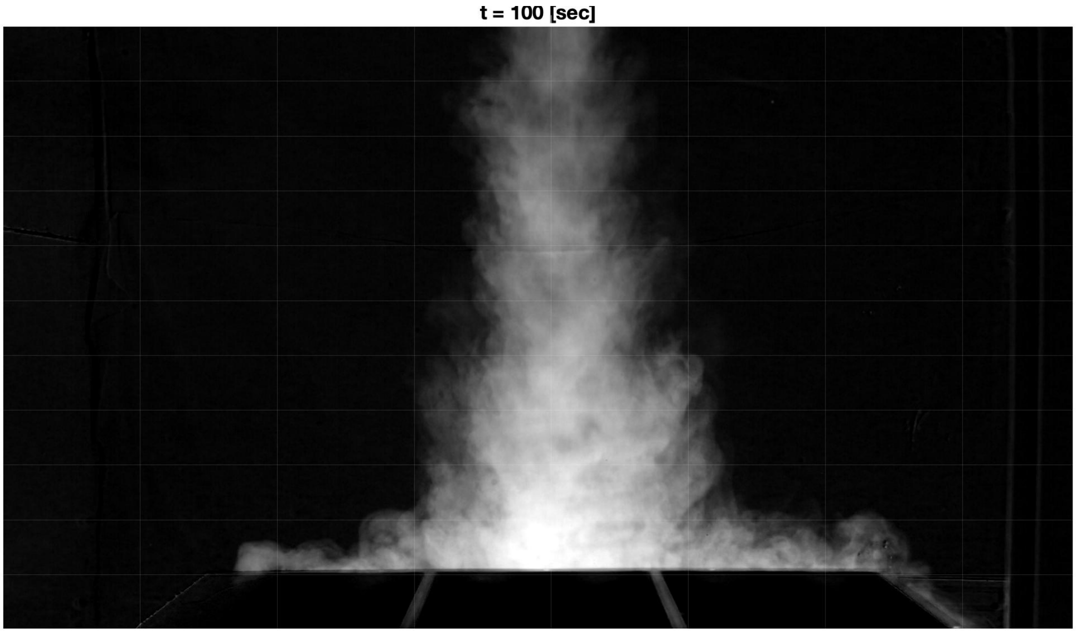


Figure G.1: Snapshot test Round 1


Figure G.2: Snapshot test Round 2

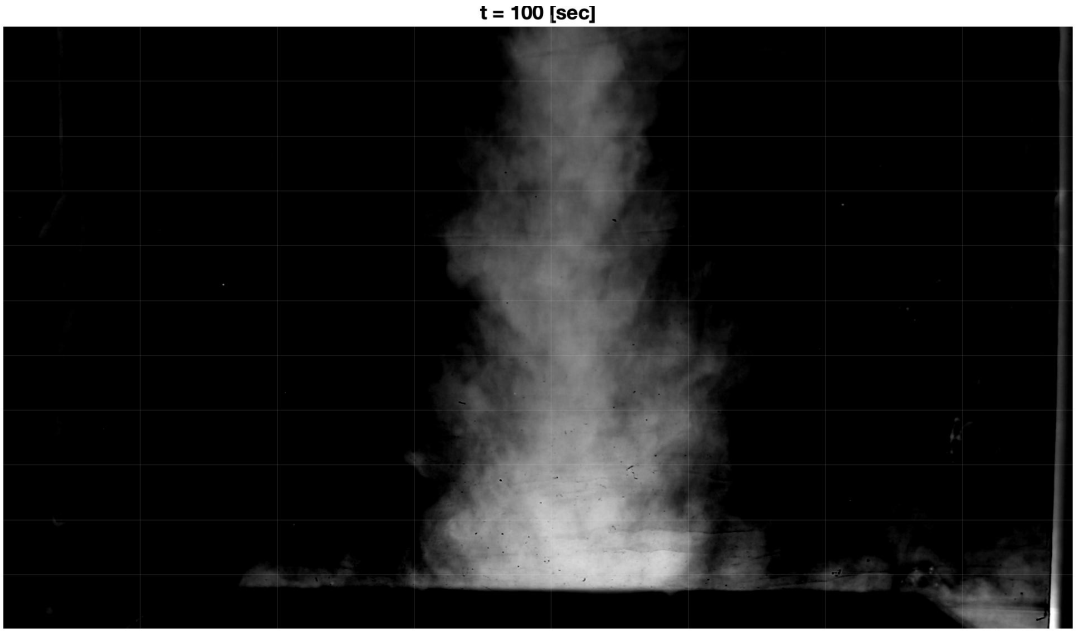


Figure G.3: Snapshot test Round 3

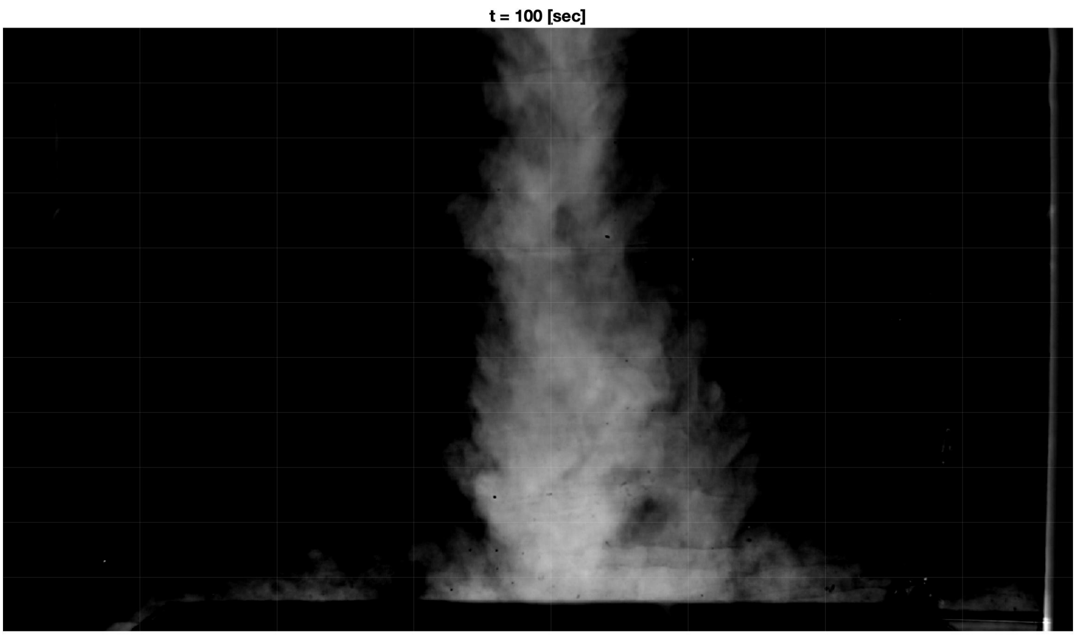


Figure G.4: Snapshot test Round 4

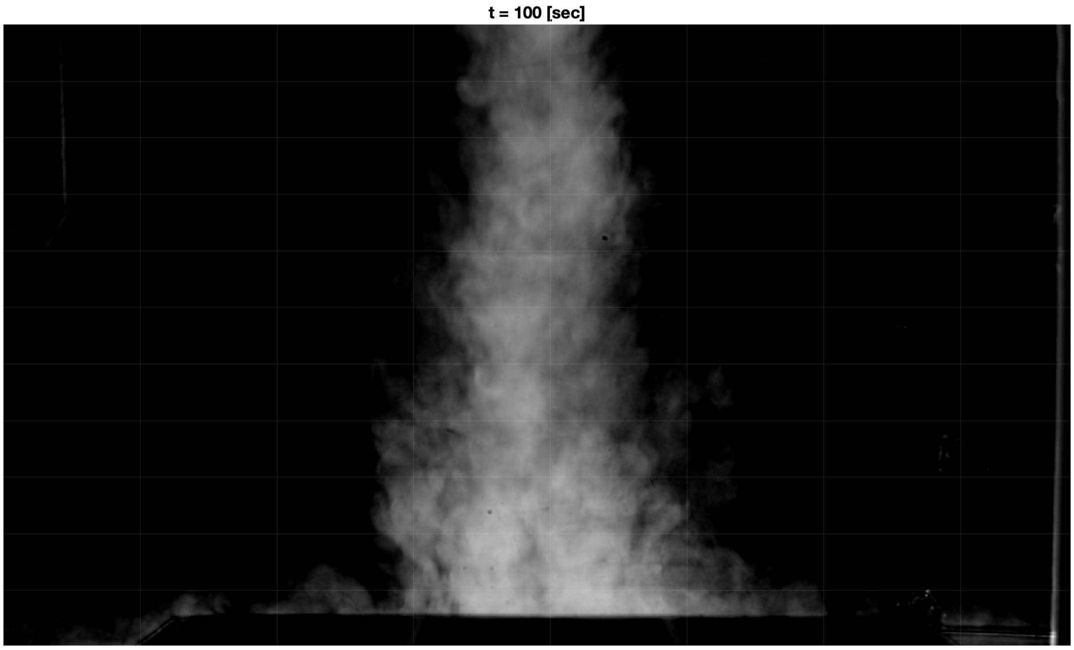


Figure G.5: Snapshot test Round 5

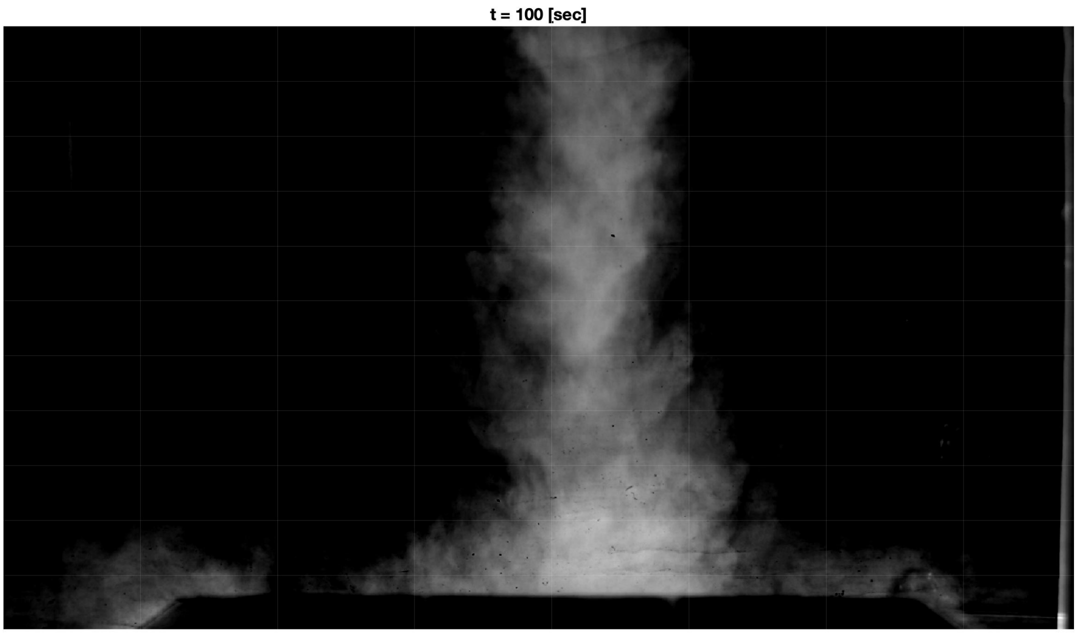


Figure G.6: Snapshot test Rectangular (20x3.9) 1

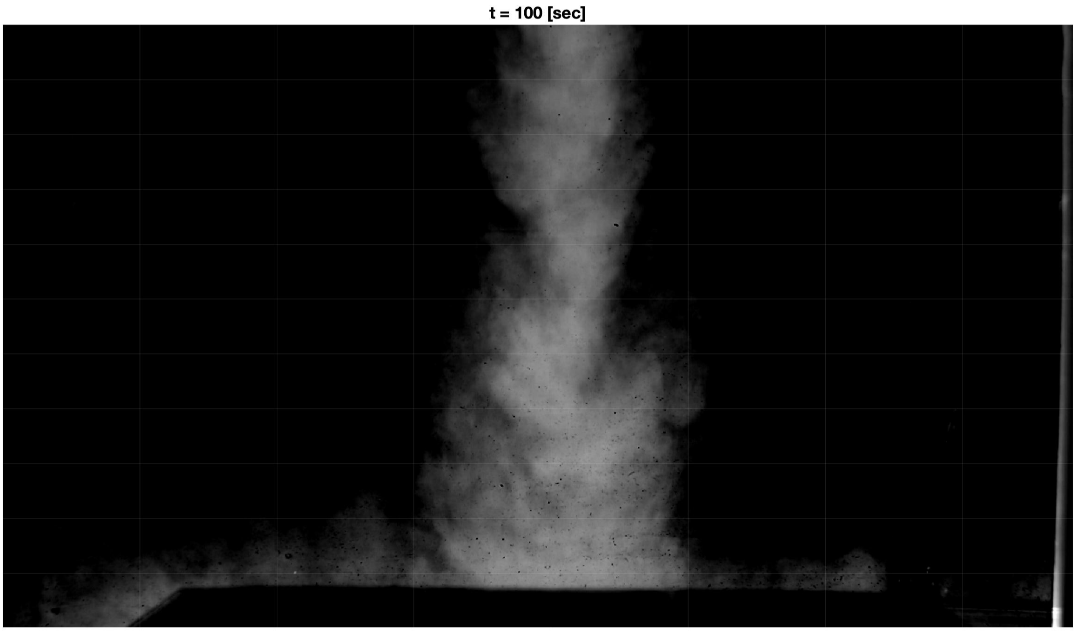


Figure G.7: Snapshot test Rectangular (20x3.9) 2

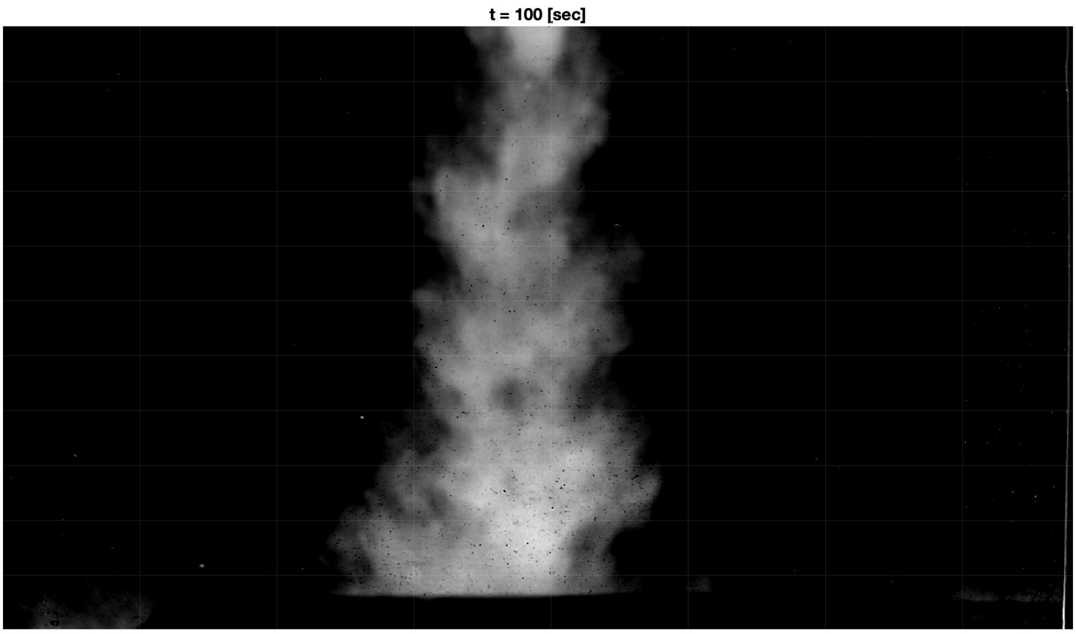


Figure G.8: Snapshot test Rectangular (20x3.9) 3

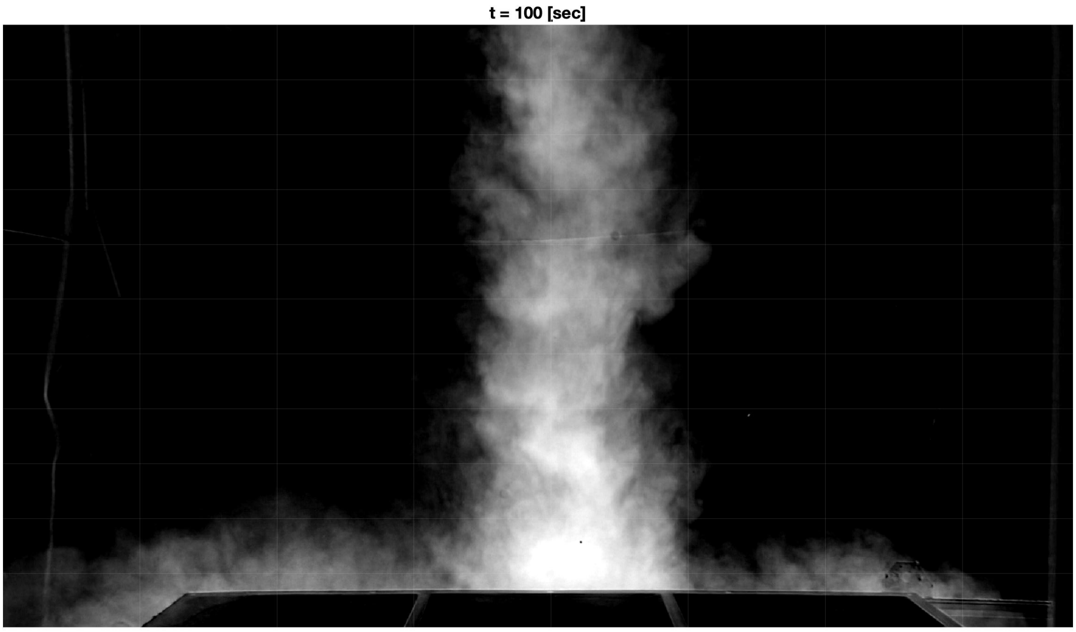


Figure G.9: Snapshot test Rectangular (20x3.9) 4

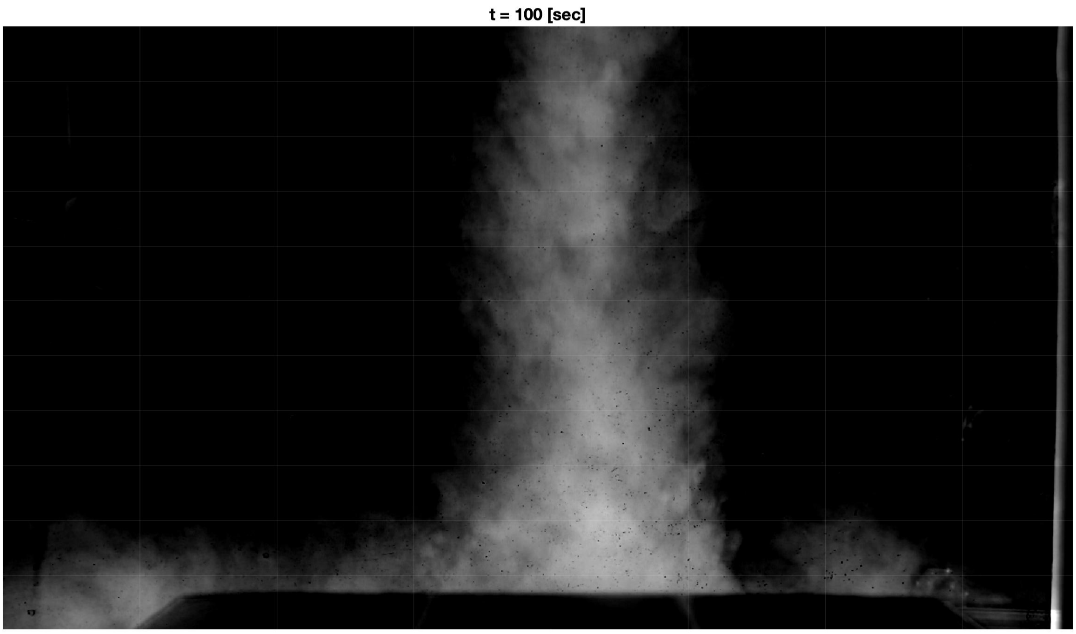


Figure G.10: Snapshot test Rectangular (20x3.9) 5

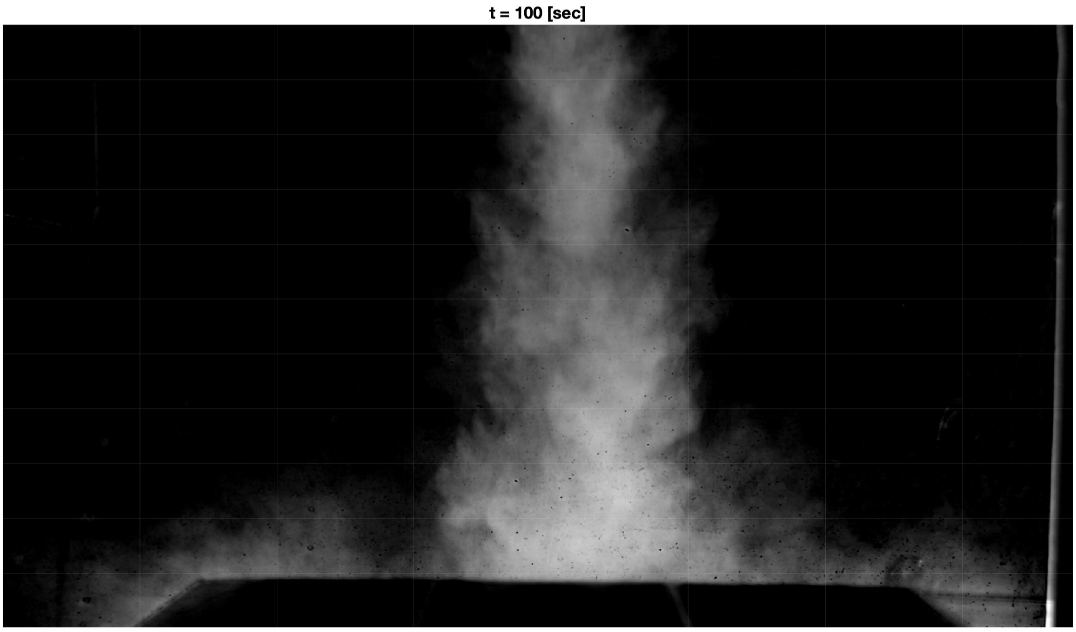


Figure G.11: Snapshot test Rectangular (20x3.9) 6

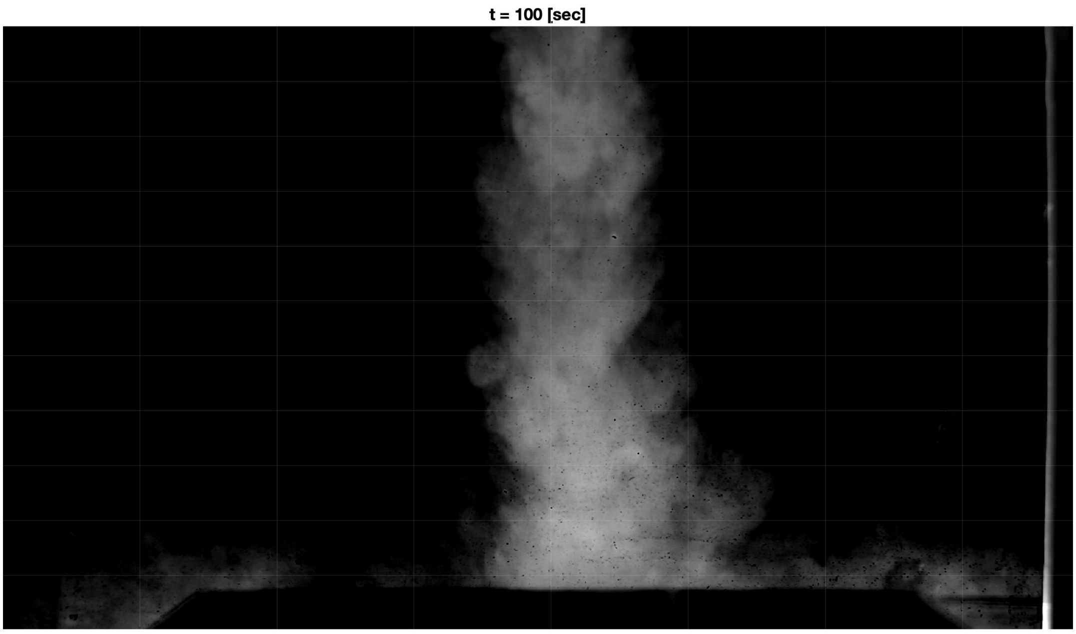


Figure G.12: Snapshot test Rectangular (20x3.9) 7

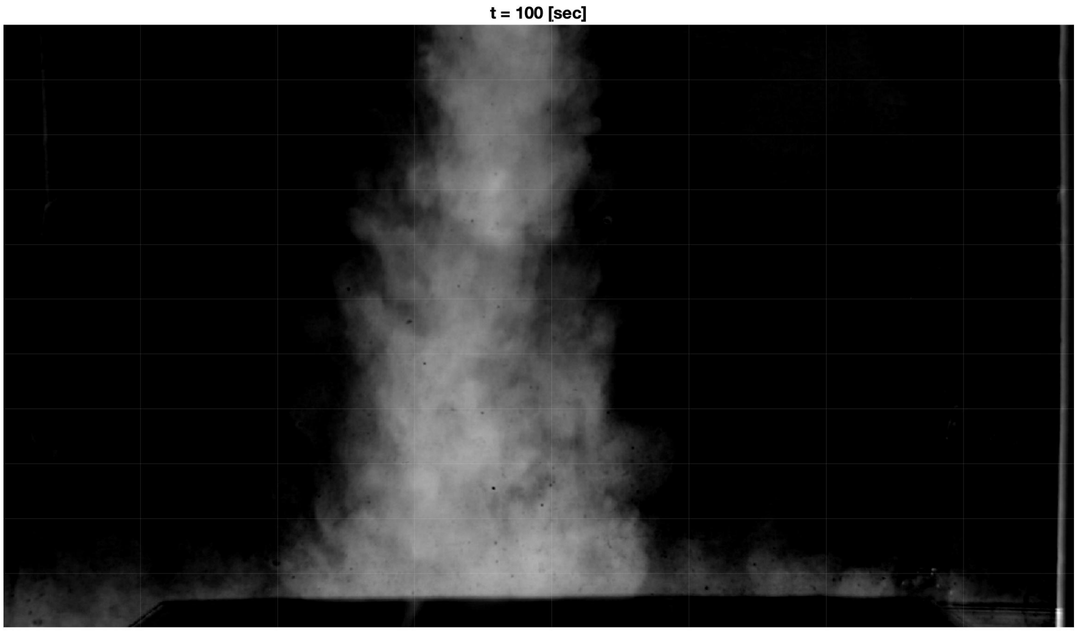


Figure G.13: Snapshot test Rectangular (20x3.9) 8

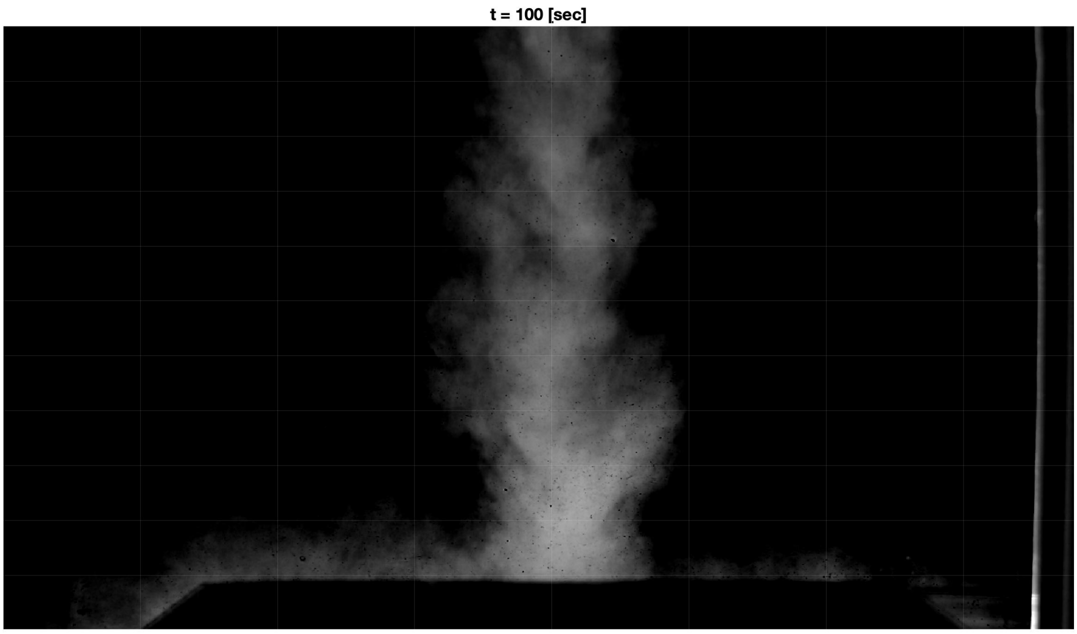


Figure G.14: Snapshot test Rectangular (20x3.9) 9

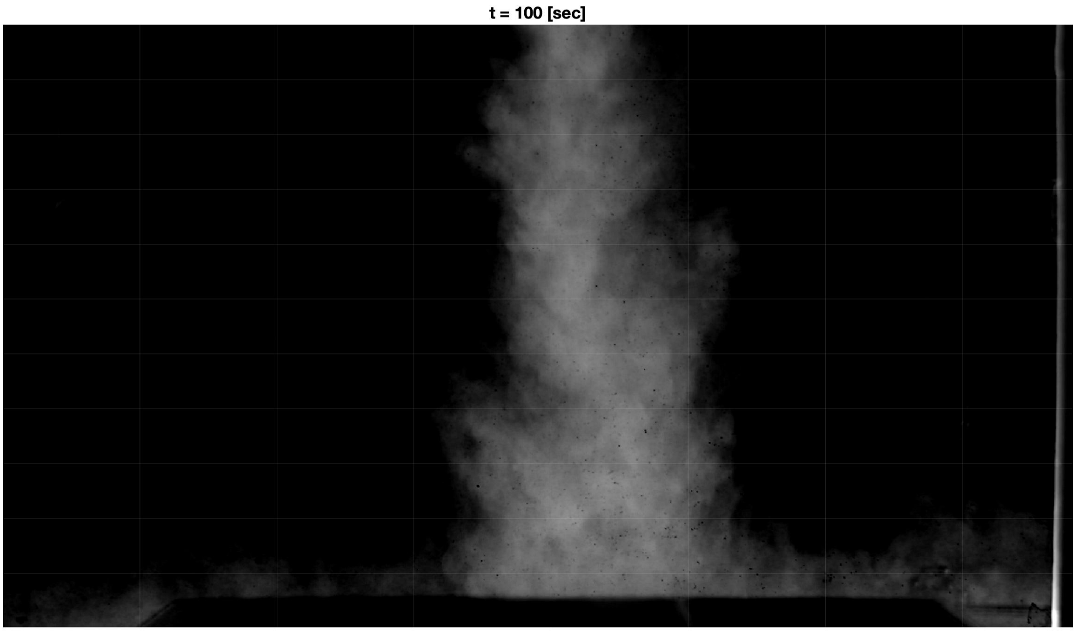


Figure G.15: Snapshot test Rectangular (20x3.9) 10

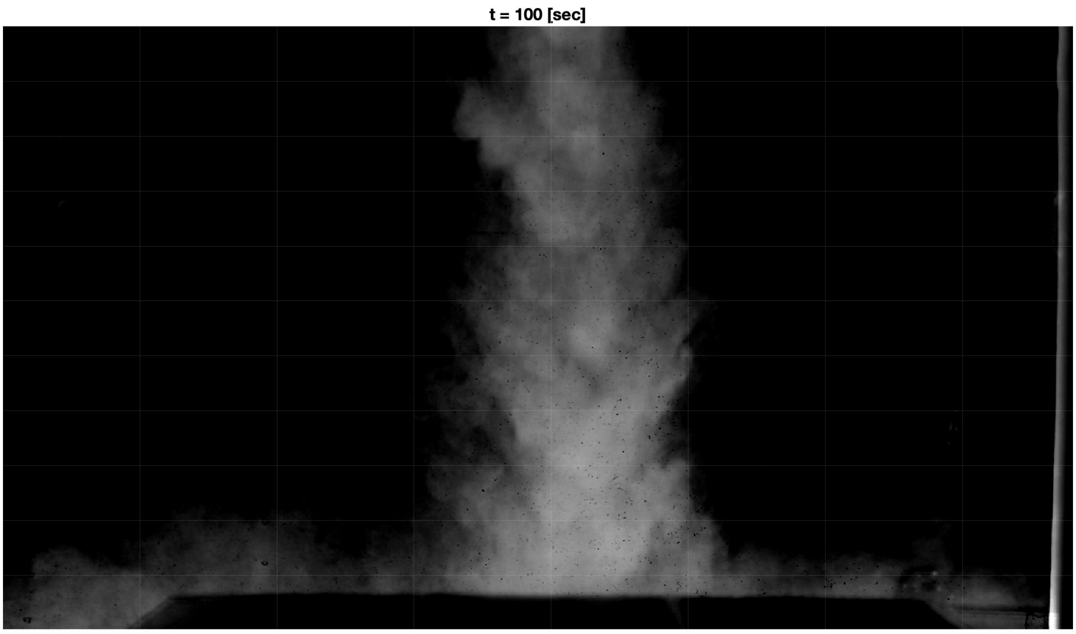


Figure G.16: Snapshot test Rectangular (20x3.9) 11

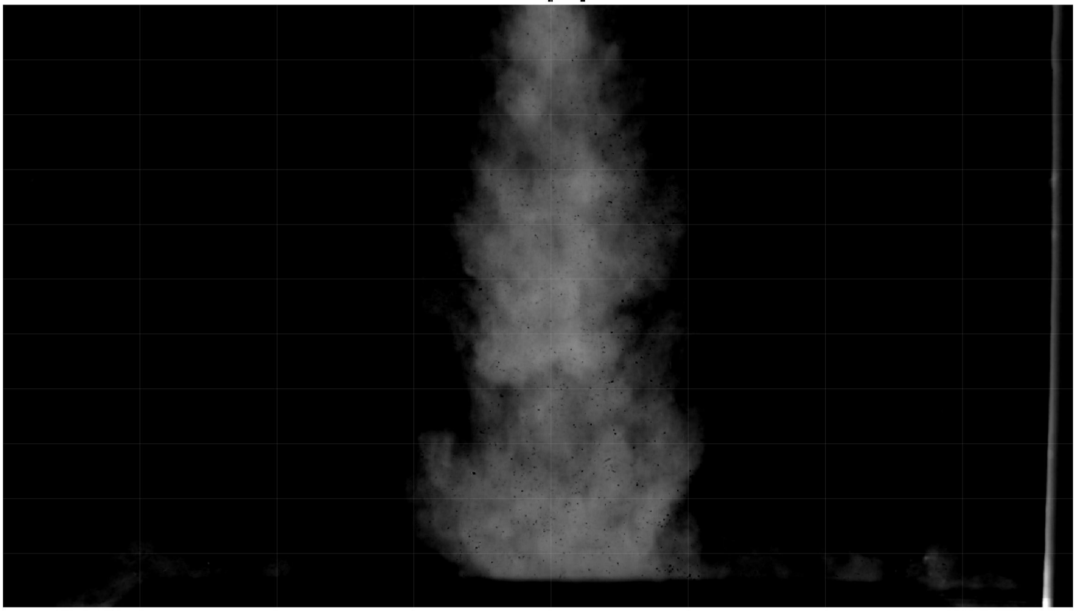


Figure G.17: Snapshot test Rectangular (20x3.9) 12

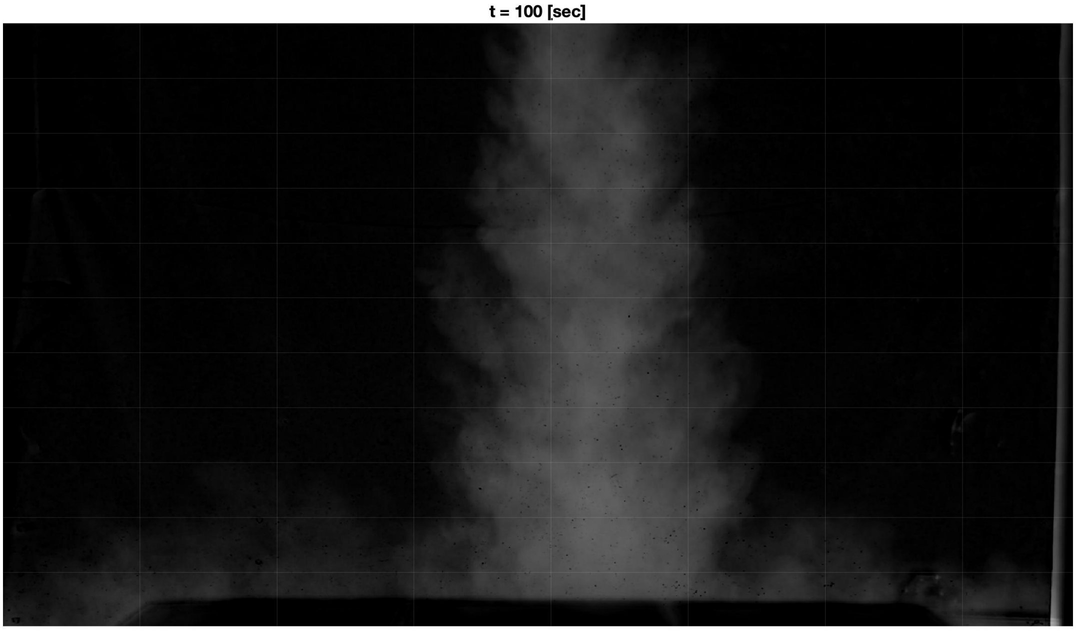


Figure G.18: Snapshot test Rectangular (20x3.9) 13

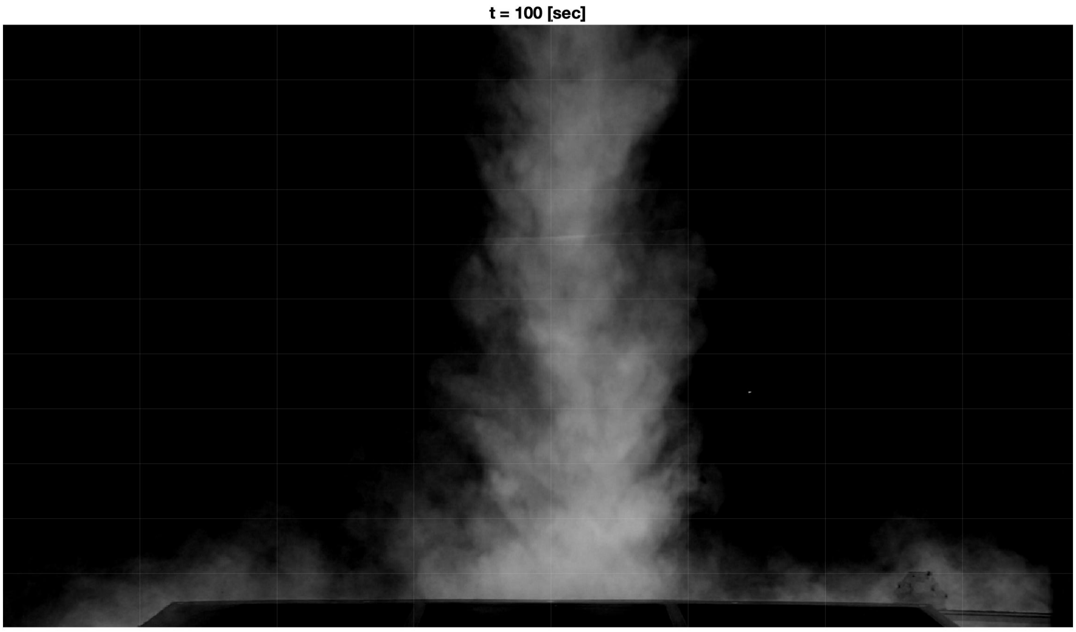


Figure G.19: Snapshot test Rectangular (20x3.9) 14

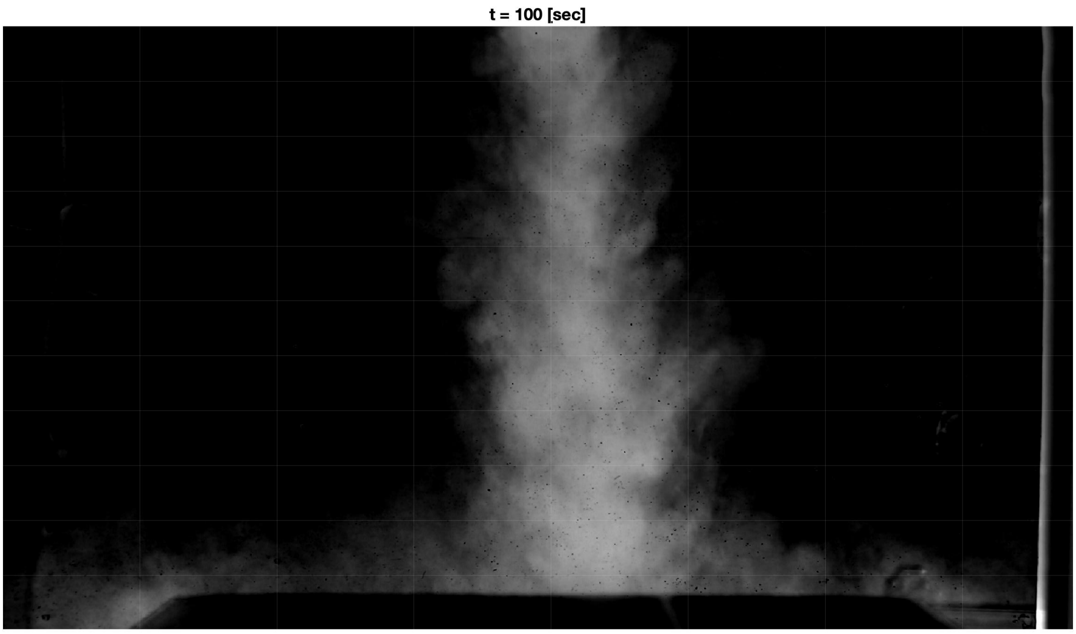


Figure G.20: Snapshot test Rectangular (20x3.9) 15

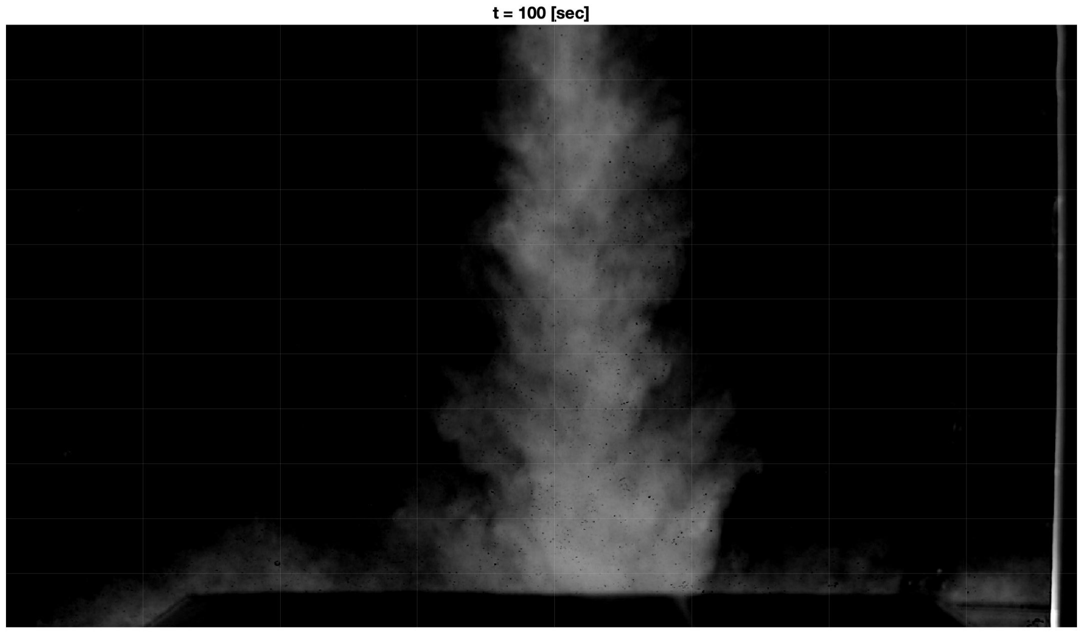


Figure G.21: Snapshot test Rectangular (20x3.9) 16

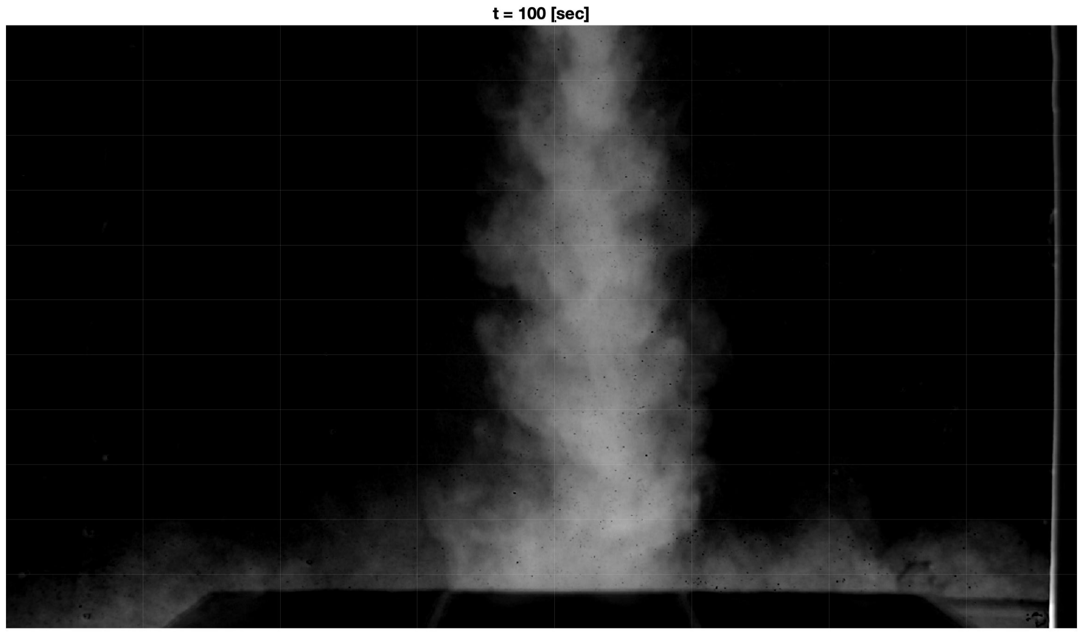


Figure G.22: Snapshot test Rectangular (20x3.9) 17

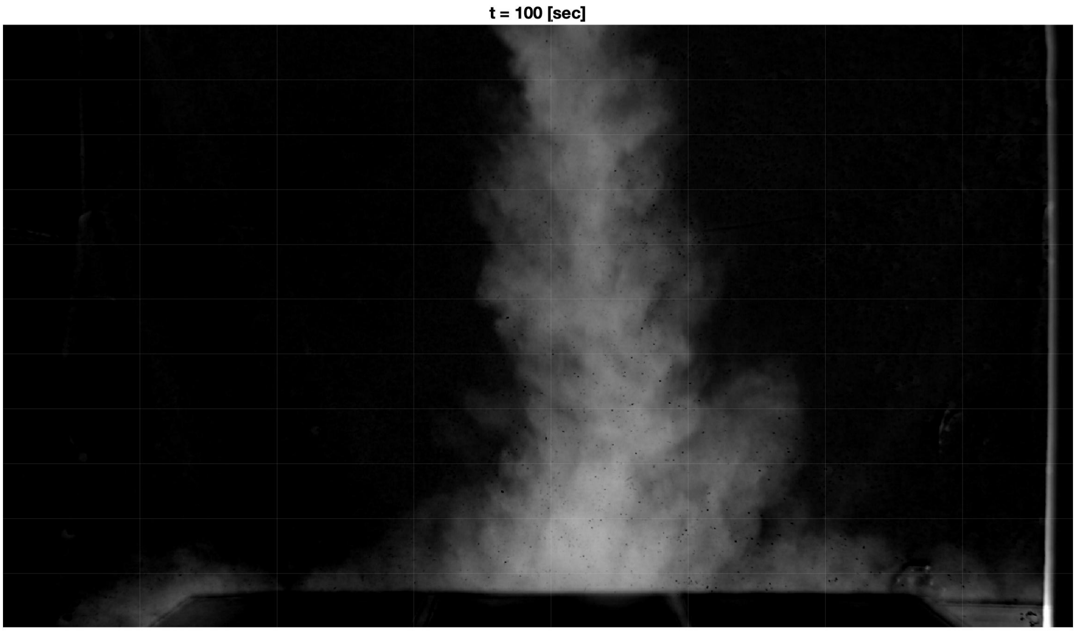


Figure G.23: Snapshot test Rectangular (20x3.9) 18

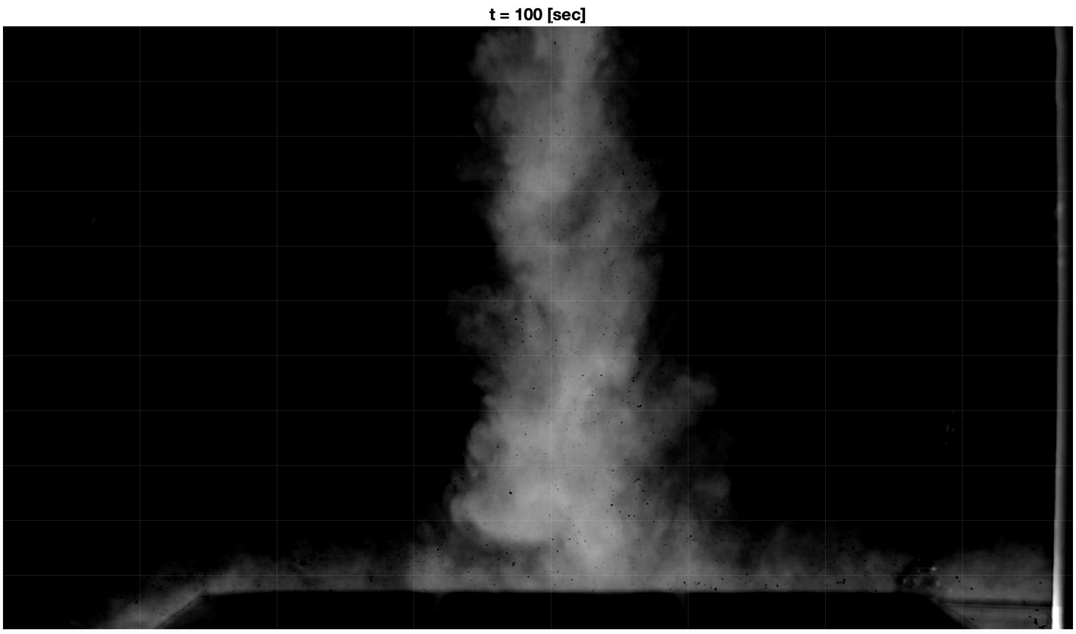


Figure G.24: Snapshot test Rectangular (20x3.9) 19

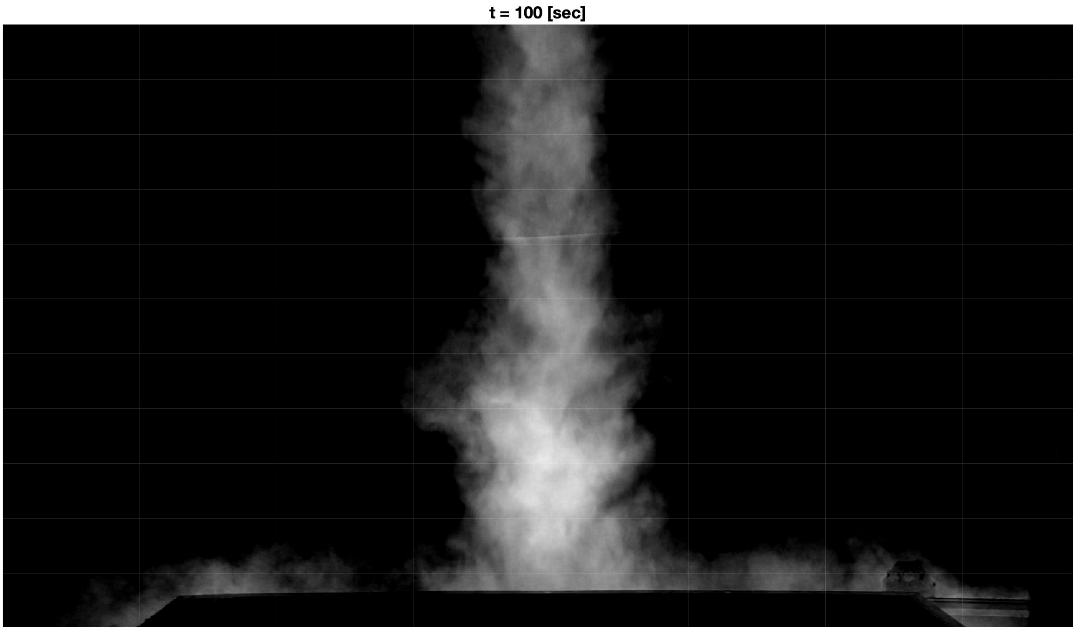


Figure G.25: Snapshot test Rectangular (20x3.9) 20

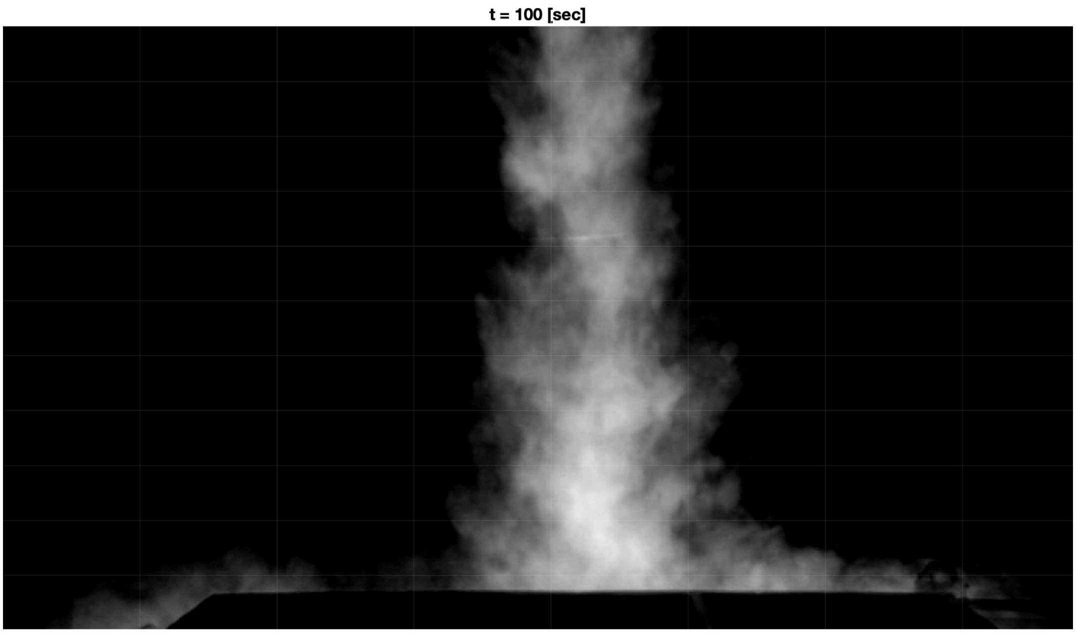


Figure G.26: Snapshot test Rectangular (30x2.6) 1

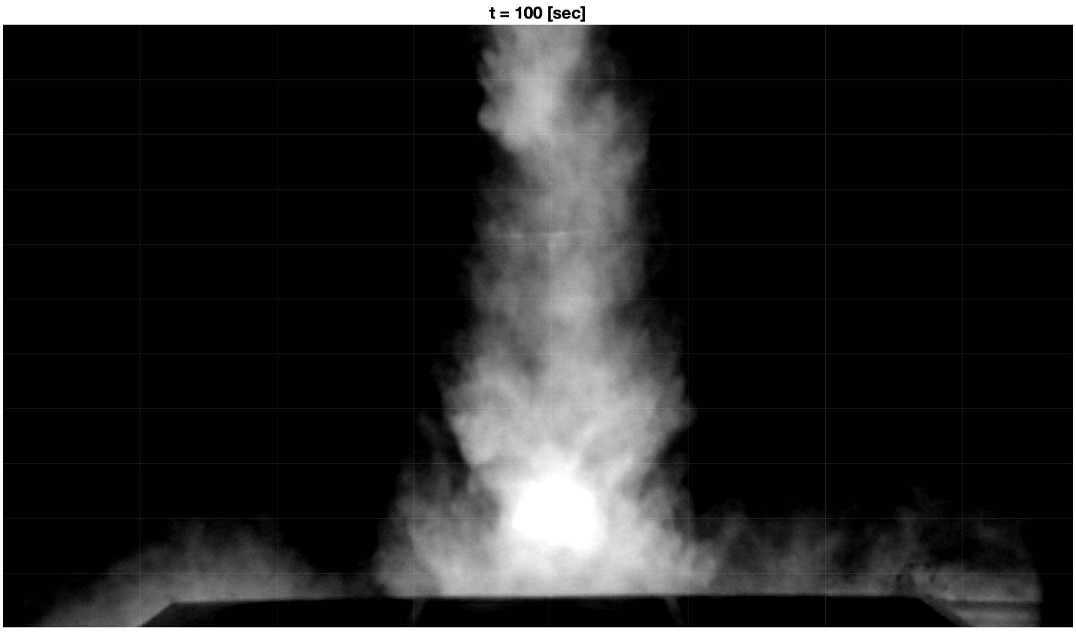


Figure G.27: Snapshot test Rectangular (30x2.6) 2

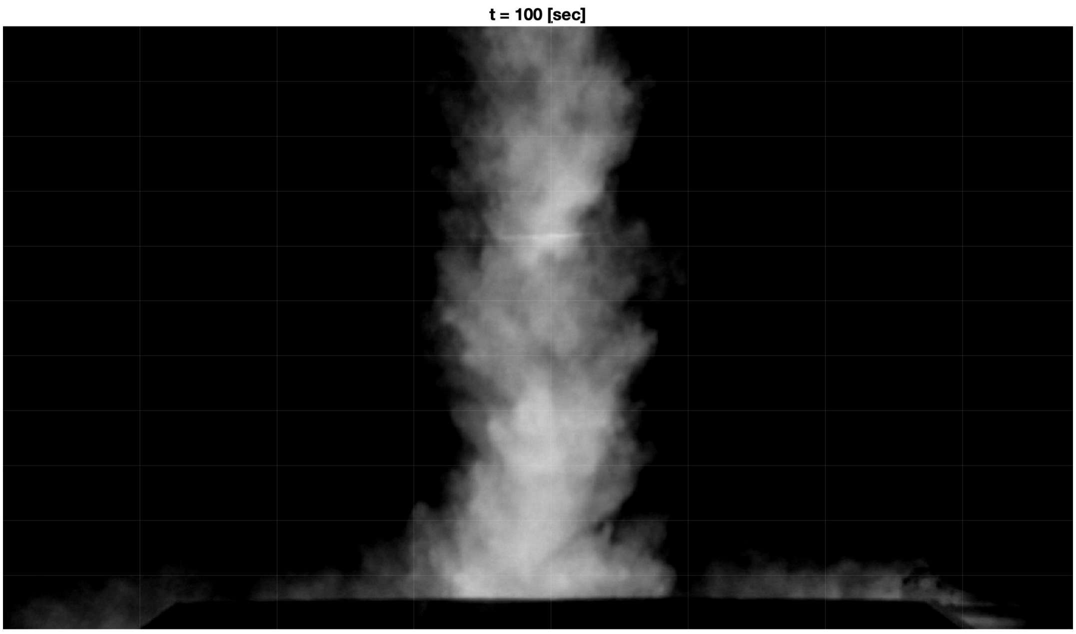


Figure G.28: Snapshot test Rectangular (30x2.6) 3

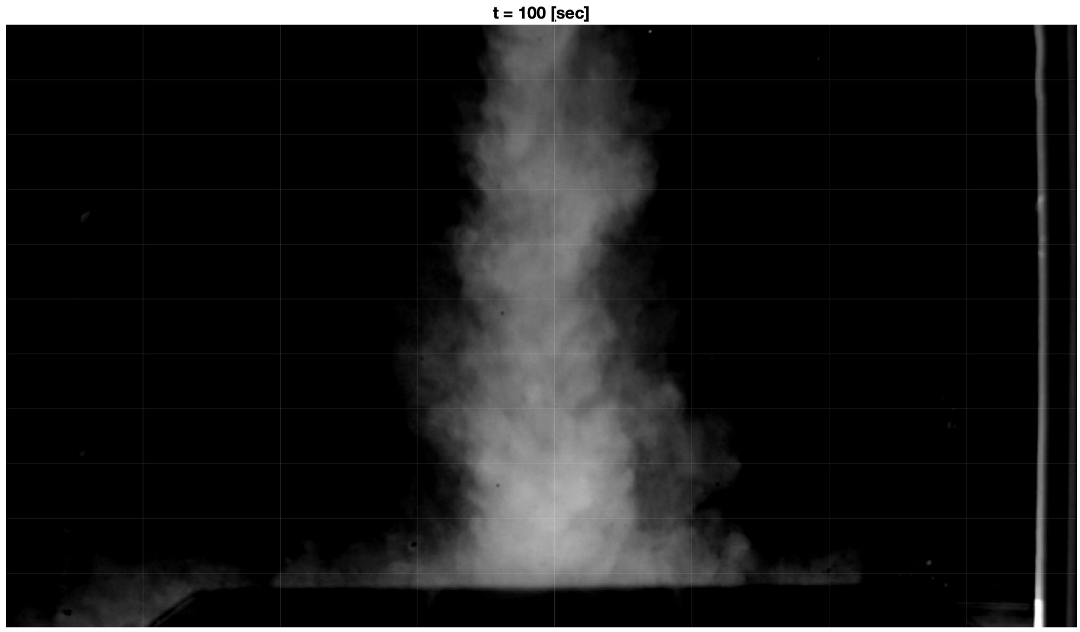


Figure G.29: Snapshot test Rectangular (30x2.6) 4

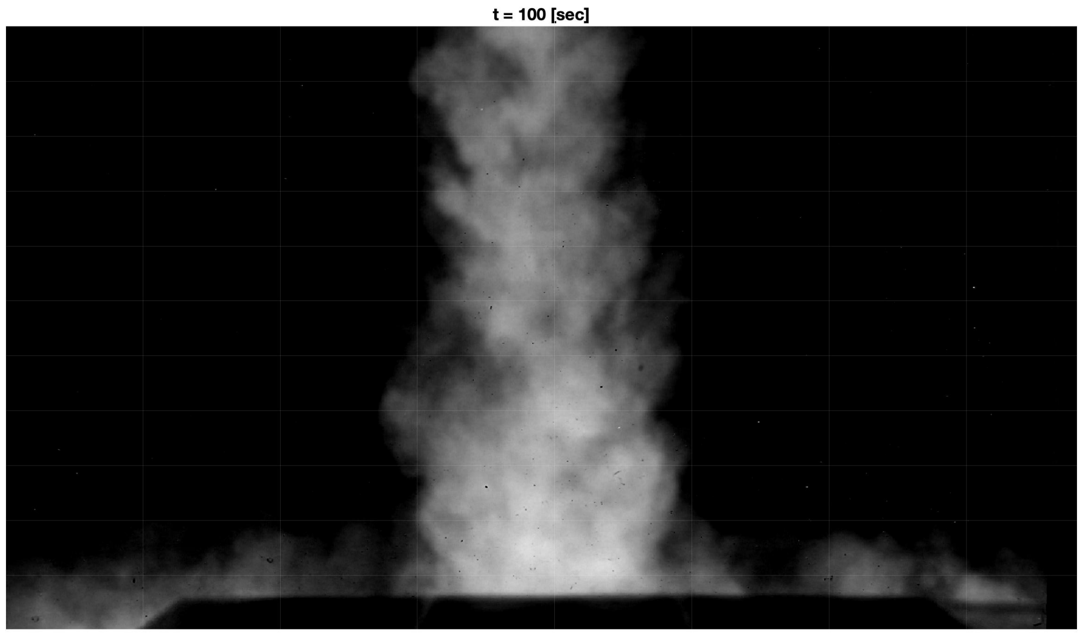


Figure G.30: Snapshot test Rectangular (30x2.6) 5

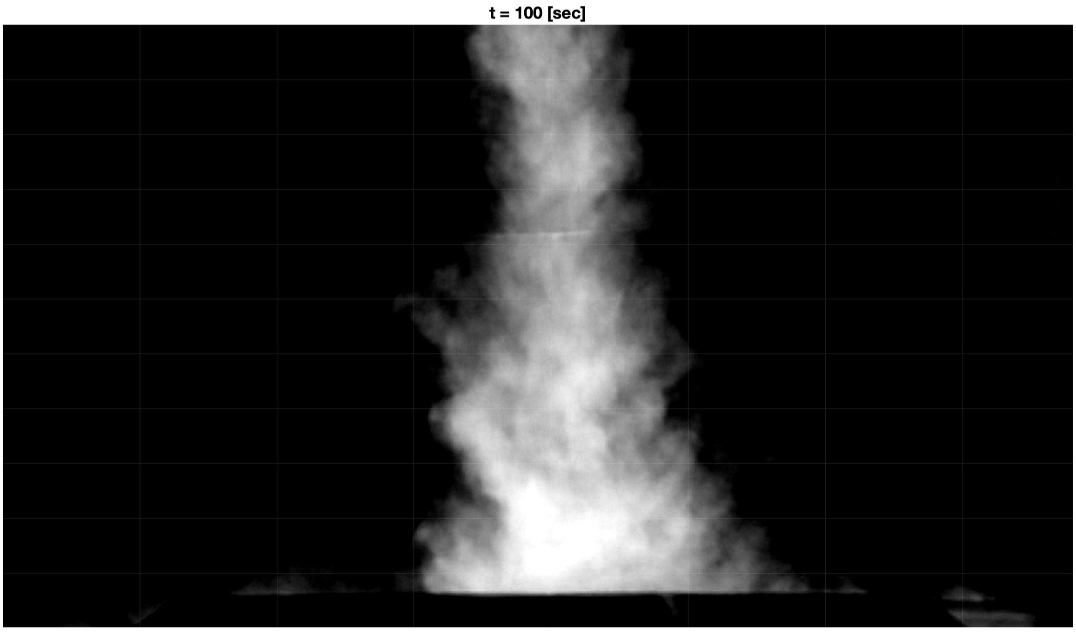


Figure G.31: Snapshot test Rectangular (30x2.6) 6

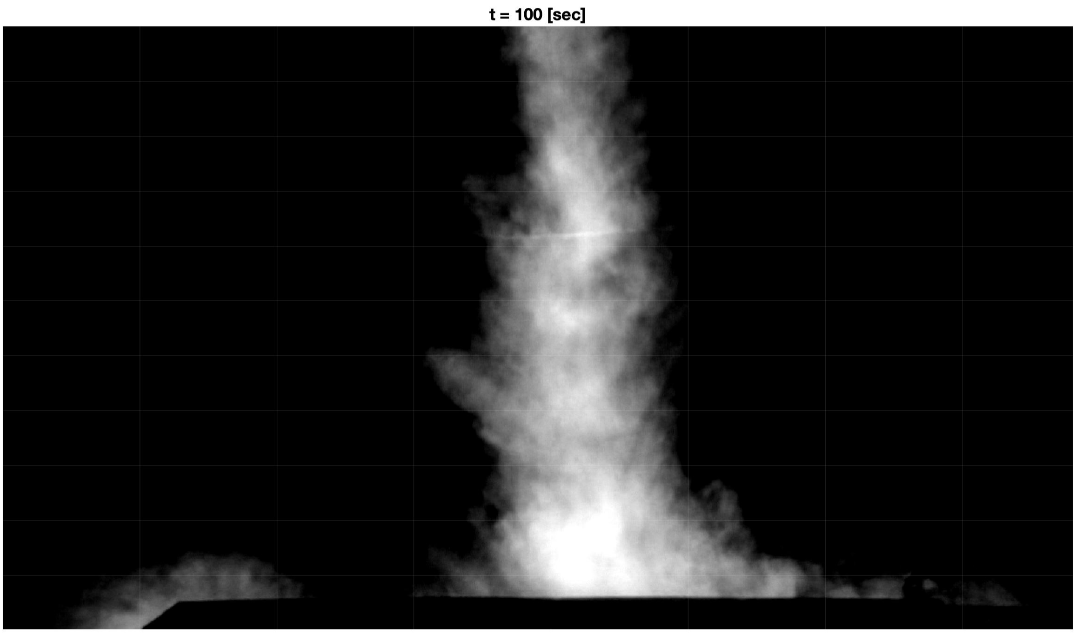


Figure G.32: Snapshot test Rectangular (30x2.6) 7

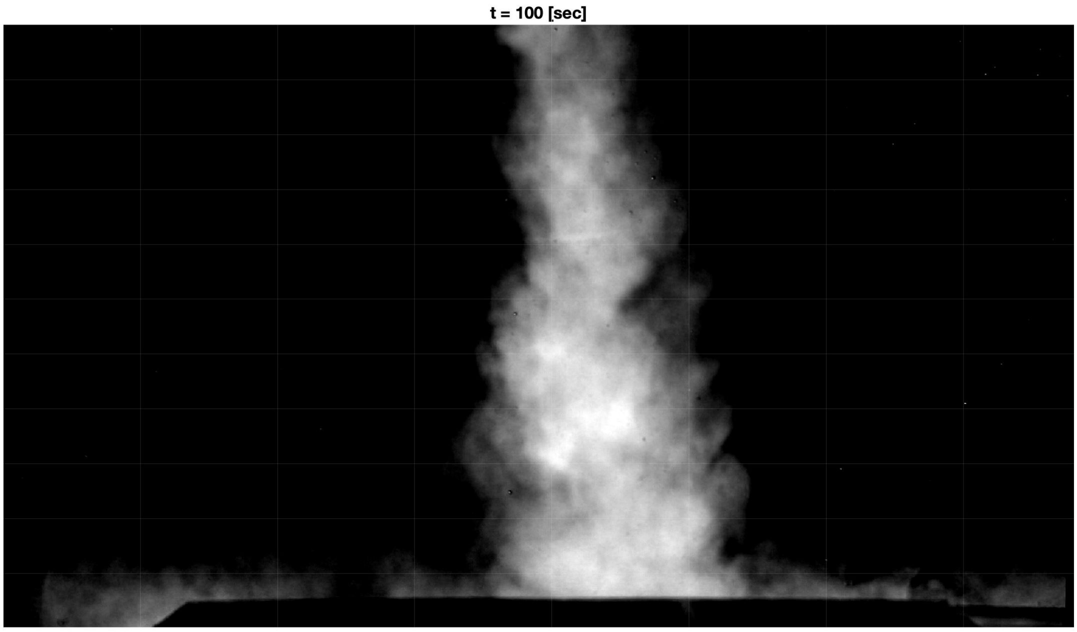


Figure G.33: Snapshot test Rectangular (30x2.6) 8

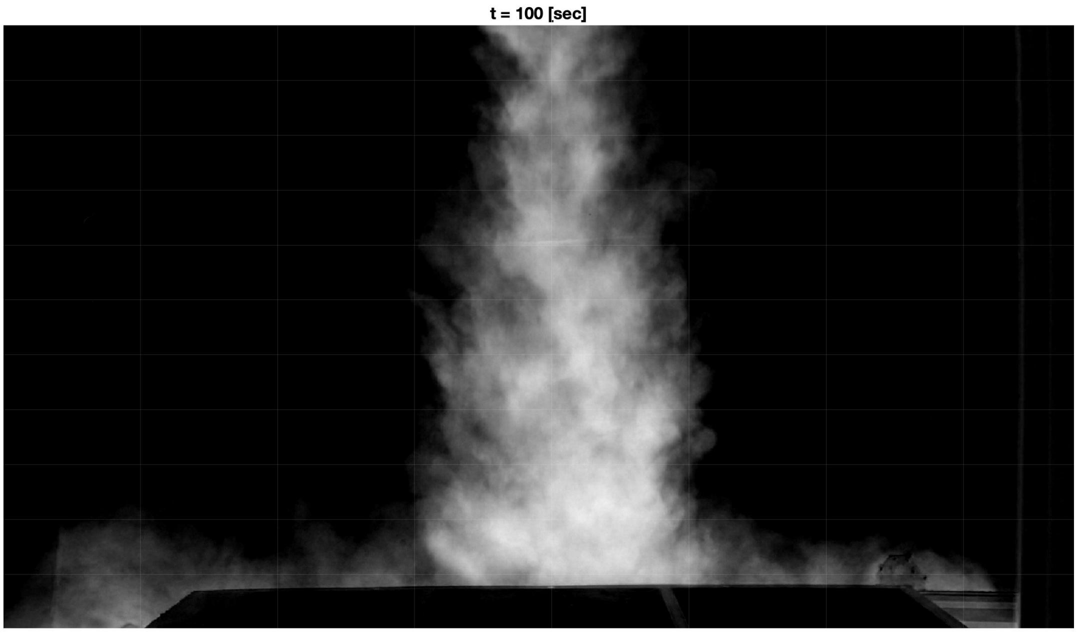


Figure G.34: Snapshot test Rectangular (30x2.6) 9

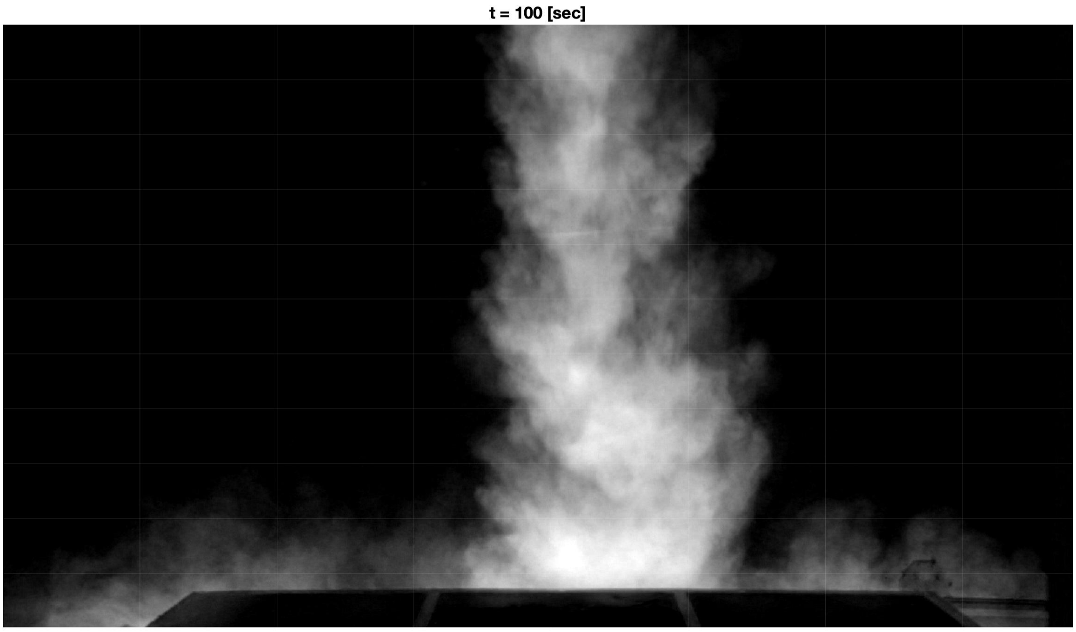


Figure G.35: Snapshot test Rectangular (30x2.6) 10

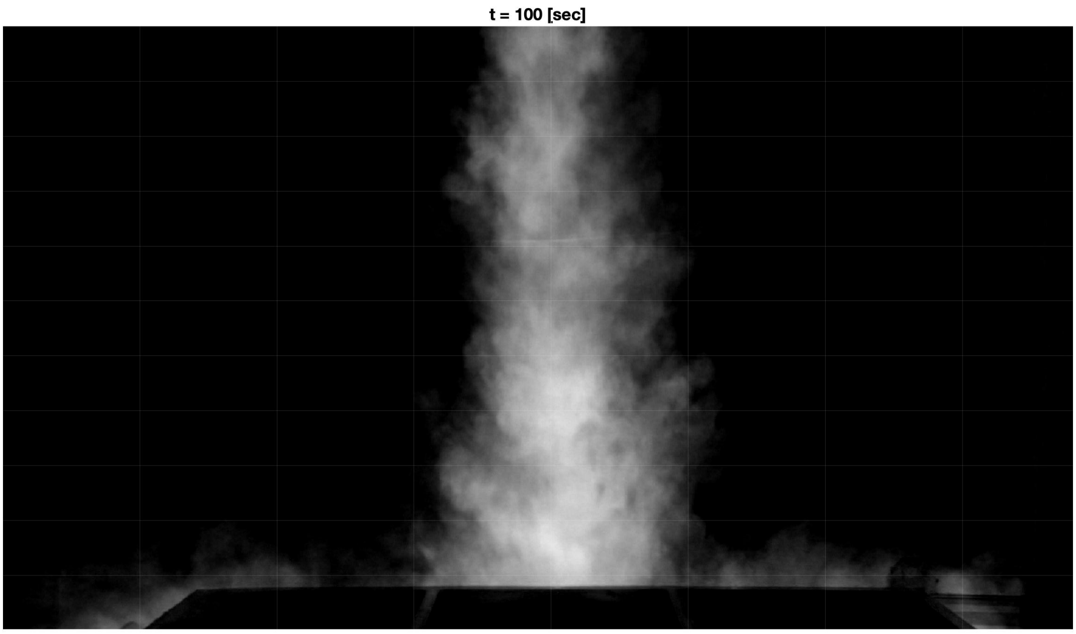


Figure G.36: Snapshot test Rectangular (30x2.6) 11

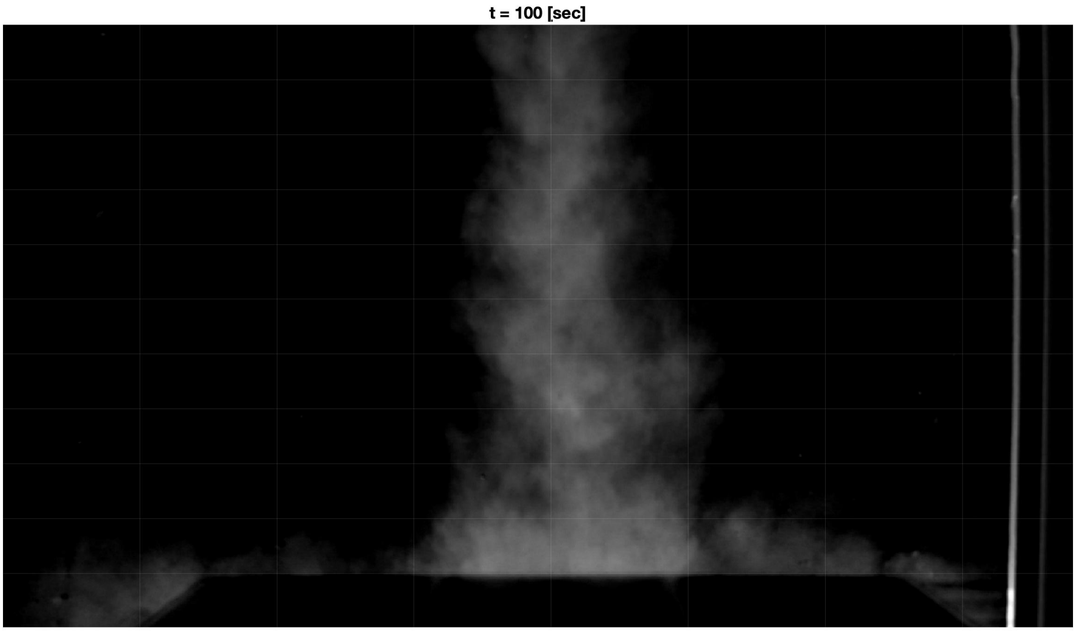


Figure G.37: Snapshot test Rectangular (30x2.6) 12

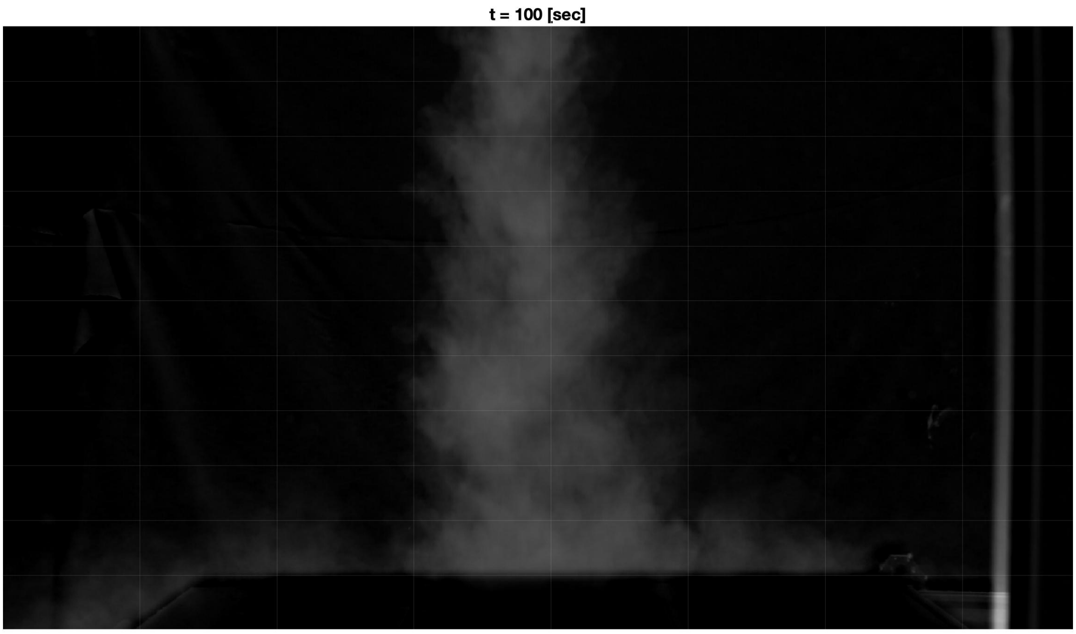


Figure G.38: Snapshot test Rectangular (30x2.6) 13

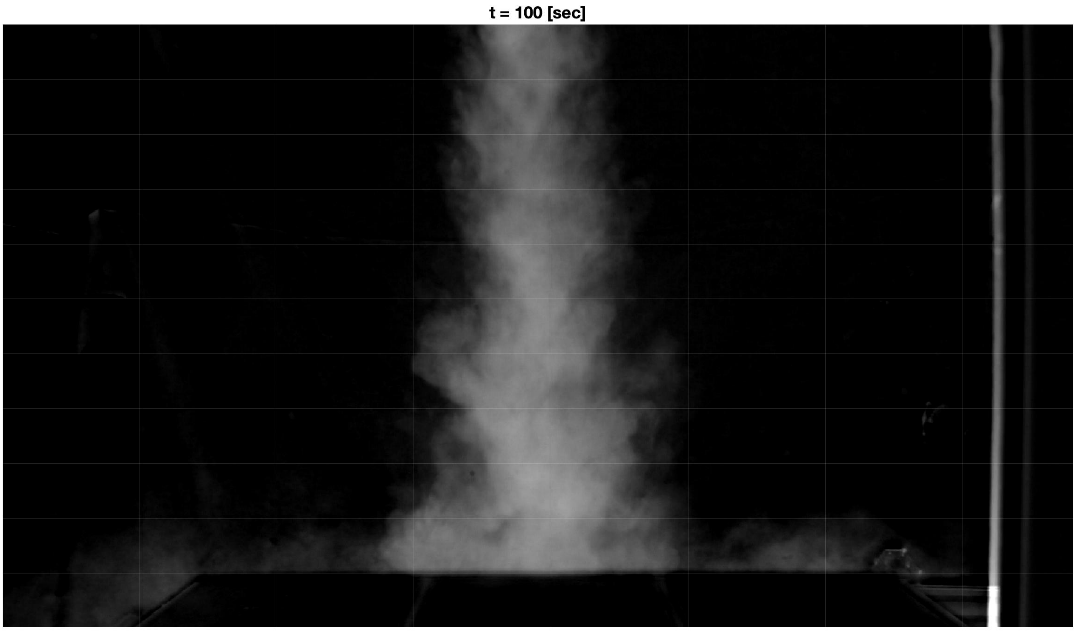


Figure G.39: Snapshot test Rectangular (30x2.6) 14

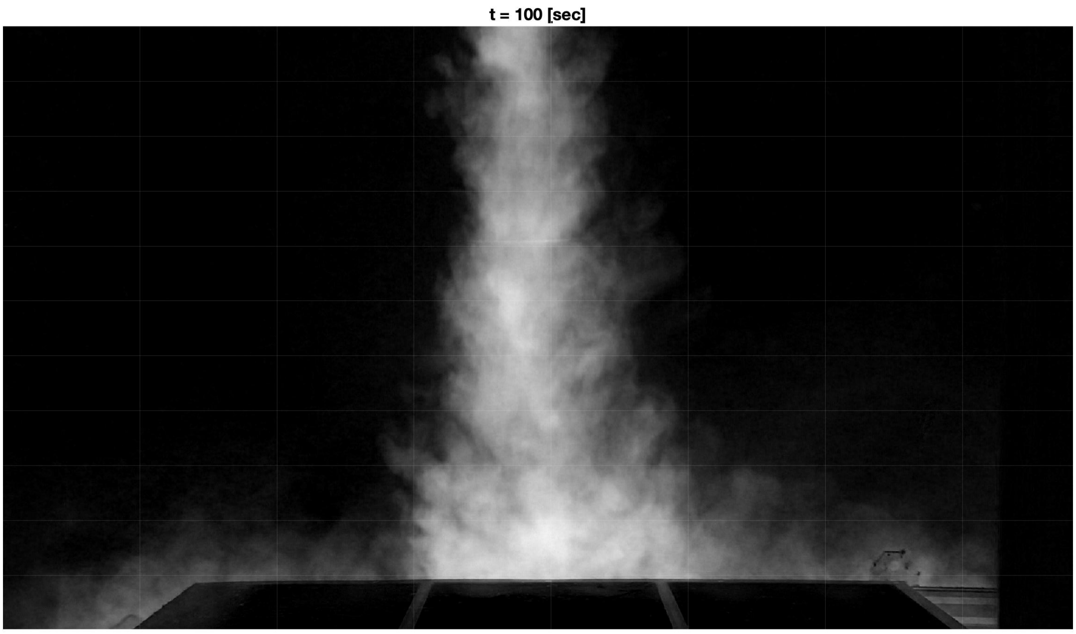


Figure G.40: Snapshot test Rectangular (30x2.6) 15

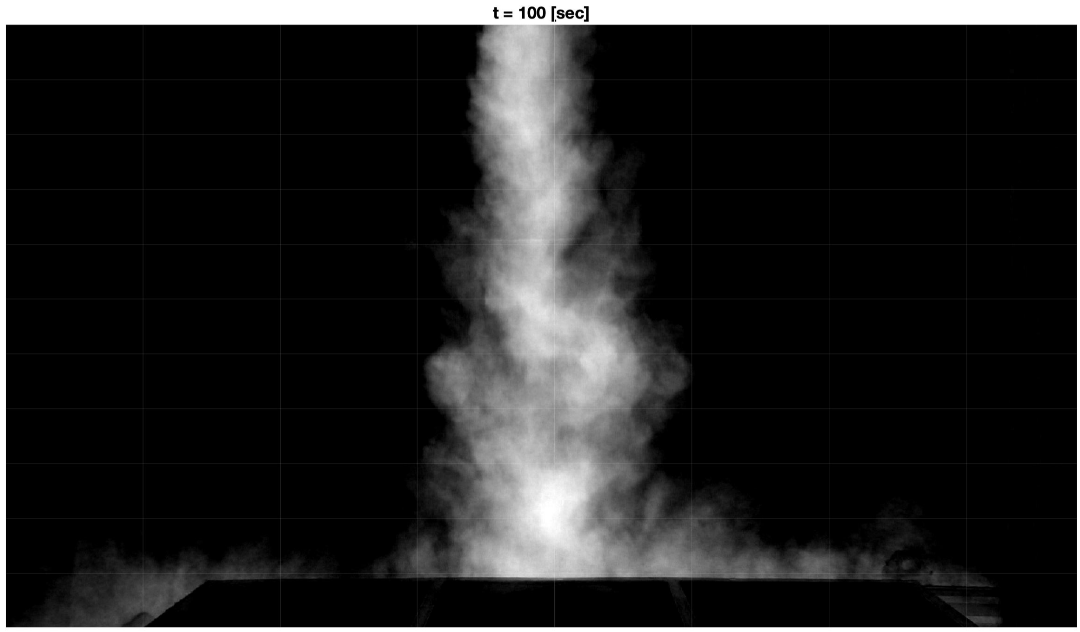


Figure G.41: Snapshot test Rectangular (30x2.6) 16

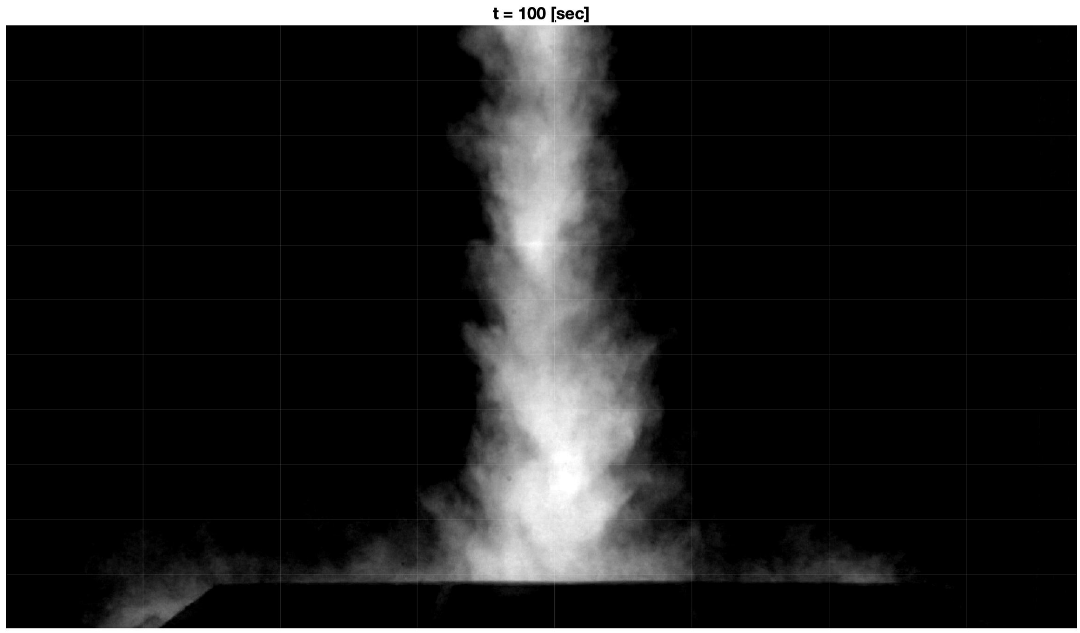


Figure G.42: Snapshot test Rectangular (30x2.6) 17

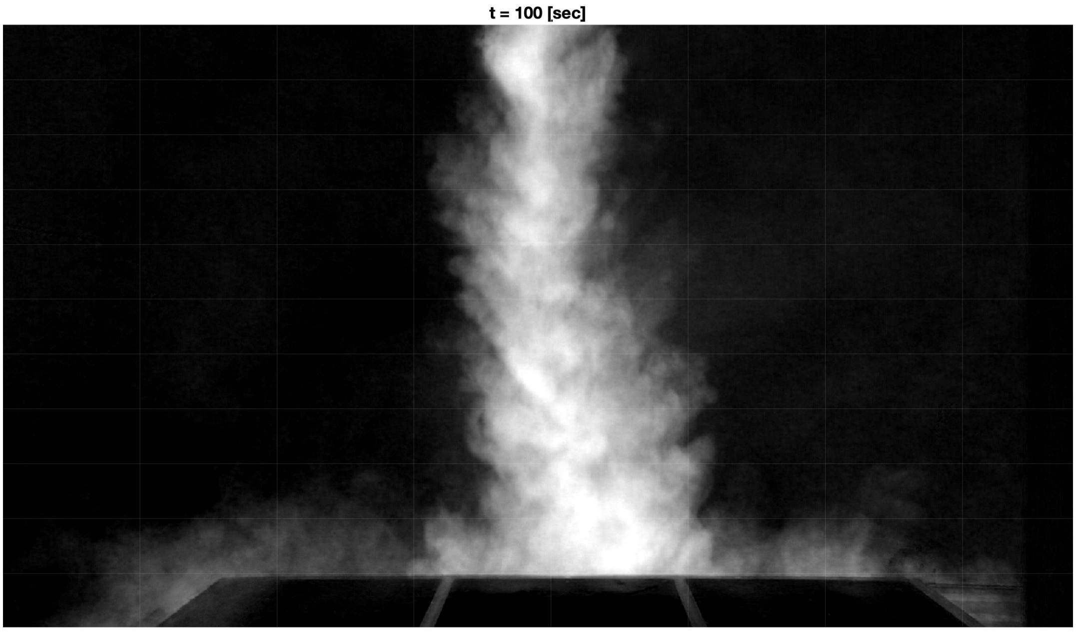


Figure G.43: Snapshot test Rectangular (30x2.6) 18

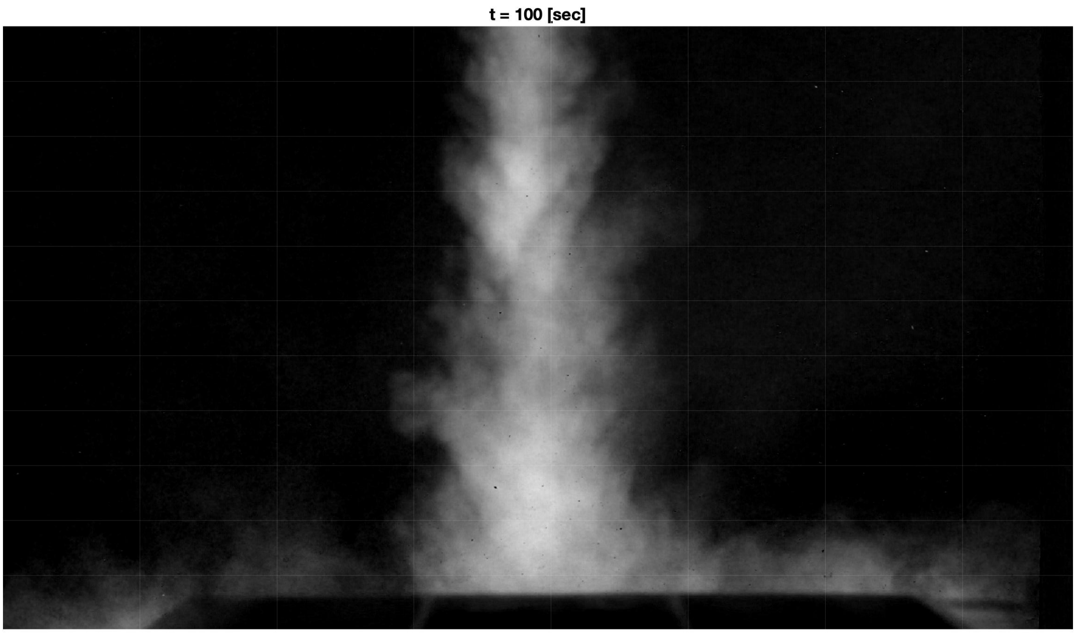


Figure G.44: Snapshot test Rectangular (30x2.6) 19

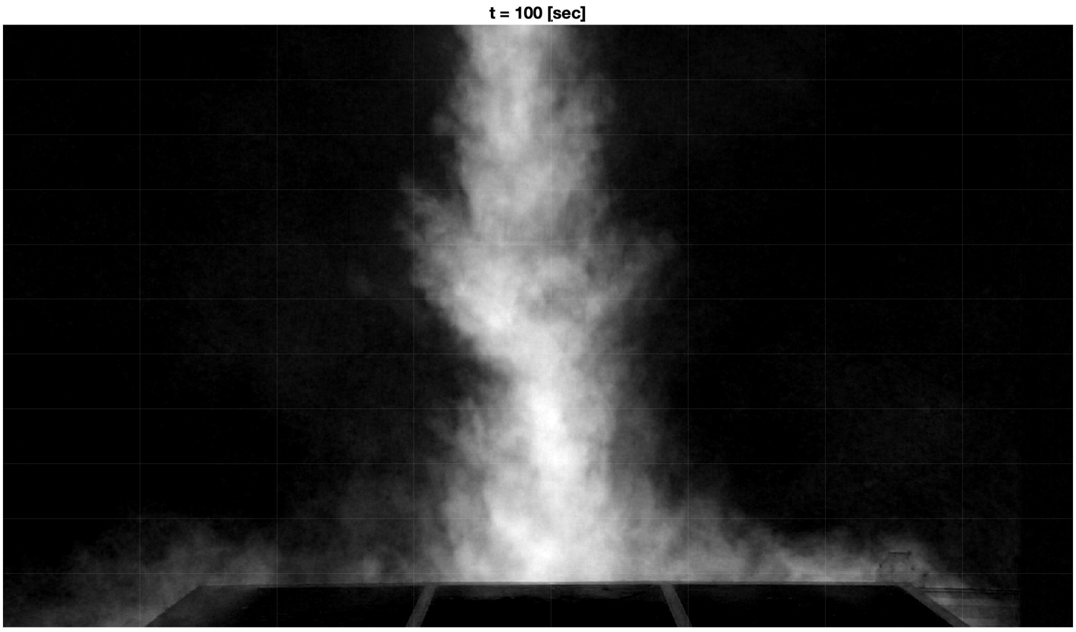


Figure G.45: Snapshot test Rectangular (30x2.6) 20

# Bibliography


Albertson, M.L., Dai, Y.B., Jensen, R.A., & Rouse, H. 1950. Diffusion of submerged jets. *Trans. ASCE*, **115**, 639–644.

Aqualytic. 2018. *Working principle / Manual*. www.aqualytic.com.

Bradbury, L.J.S. 1957. The structure of a self-preserving turbulent plane jet. *Journal of Fluid Mechanics*, **23**, 31–64.

Byishimo, P. 2018. *Experiments and 3D CFD simulations of deep-sea mining plume dispersion and seabed interactions*. Master thesis, Delft University of Technology, the Netherlands.

Camp, T.R. 1946. Sedimentation and the design of settling tanks. *Trans. ASCE*, 895–936.

Dankers, P.J.T. 2002. *The behaviour of fines released due to dredging: A literature review*. Master thesis, Delft University of Technology, the Netherlands.

de Wit, L. 2015. *3D CFD modelling of overflow dredging plumes*. Ph.D. thesis, Delft University of Technology, the Netherlands.

Decrop, B. 2016. *Numerical and Experimental Modelling of Near-Field Overflow Dredging Plumes*. Ph.D. thesis, Universiteit Gent and Katholieke Universiteit Leuven, Belgium.

Fischer, H., List, E., Koh, R., Imberger, J., & Brooks, N. 1979. *Mixing in Inland and Coastal Waters*. Academic Press.

Frick, W.E. 1984. Non-empirical closure of the plume equations. *Atmospheric Environment*, **18**, 653–662.

Haven, B., & Kurosaka, M. 1997. Kidney and anti-kidney vortices in cross flow jets. *Journal of Fluid Mechanics*, **352**, 27–64.

Hirt, C., & Nichols, B. 1981. Volume of fluid (VOF) method for the dynamics of free boundaries. *Journal of Computational Physics*, **39(1)**, 201–225.

IHC. 2018. *Overflow systems*. https://www.royalihc.com/en/products/dredging/hopper-dredging/overflow-systems.

Institute, Nautical. 2018. *Rainbowing*. https://www.theartofdredging.com/rainbowing.htm.

Jirka, G.H. 2004. *Environmental Fluid Mechanics*. Vol. 4. Kluwer Academic Publisher. Chap. Integral Model for Turbulent Buoyant Jets in Unbounded Stratified Flows. Part I: Single Round Jet.

Kotsovinos, N.E., & List, E.J. 1977. Plane turbulent buoyant jet Part I: Integral properties. *Journal of Fluid Mechanics*, **81**, 25–44.

Lee, J.H.W., & Cheung, V. 1990. Generalized Lagrangian model for buoyant jets in current. *Journal of Environmental Engineering*, **116**, 1085–1106.

Lee, J.H.W., & Chu, V.H. 2003. *Turbulent jets and plumes, a Langrangian Approach*. Kluwer Academic Publishers.

Miedema, S.A., & Vlasblom, W.J. 1996. Theory for hopper sedimentation. *29th annual Texas AM dredging seminar*.

Miller, D., & Comings, E. 1957. Static pressure distribution in the free turbulent jet. *Journal of Fluid Mechanics*, **3**, 1–16.

Morton, B.R., & Turner, J.S. 1956. Turbulent gravitational convection from maintained and instantaneous sources. *Proceedings of the Royal Society of London*, **A234**, 1–23.

Newell, R., Hitchcock, D., & Seiderer, L. 1999. Organic Enrichment Associated with Outwash from Marine Aggregates Dredging: A Probable Explanation for Surface Sheens and Enhanced Benthic Production in the Vicinity of Dredging Operations. *Marine Pollution Bulletin*.

Ooijens, S.C. 1999. Adding dynamics to the Camp model for the calculation of overflow losses. *Terra et Aqua*, 12–21.

Papanicolaou, P., & List, E.J. 1988. Investigations of round vertical turbulent buoyant jets. *Journal of Fluid Mechanics*, **195**, 341–391.

Royal IHC. 2017. *Overflow systems - maximizing the retention of solids*. Leaflet.

Salewski, M., Stankovic, D., & Fuchs, L. 2008. Mixing in circular and non-circular jets in cross flow. *Flow, Turbulence and Combustion*, **80(2)**, 255–283.

Saremi, S., & Jensen, J.H. 2014b. Numerical modelling of the effect of the green valve on air entrainment at hopper overflow. *Coastal Engineering Proceedings, 1(34)*.

Smith, S.J., & Friedrichs, C.T. 2011. Size and settling velocities of cohesive flocs and suspended sediment aggregates in a trailing suction hopper dredge plume. *Continential Shelf Research 31 (S50 - S63)*.

van Rhee, C. 2002. *On the sedimentation process in a trailing suction hopper dredger*. Ph.D. thesis, Delft University of Technology, the Netherlands.

van Rhee, C. 2017. *Lecture notes dredging processes 2 (OE4727)*. Tech. rept. Delft University of Technology, the Netherlands.

Warringa, S. 2017. *Plume impact on deep sea floor*. Research Assignment, Delft University of Technology, the Netherlands.

Winterwerp, J.C. 2002. Near-field behaviour of dredging spill in shallow water. *Journal of Waterway, Port, Coastal and Ocean Engineering*.

Wright, S.J. 1984. Buoyant jets in density-stratified cross flow. *Journal of Hydraulic Engineering*.

Zhang, W., & Zhu, D.Z. 2013. Bubble characteristics of air-water bubbly jets in crossflow. *International Journal of Multiphase Flow*, **55(0)**, 156–171.